Adaptive Numerical Techniques for the Solution of Electromagnetic Integral Equations

A Thesis Presented to

The Academic Faculty

By

Usman Saeed

In Partial Fulfillment

of the Requirements for the Degree of

Doctor of Philosophy in Electrical and Computer Engineering

School of Electrical and Computer Engineering

Georgia Institute of Technology

August 2011

Adaptive Numerical Techniques for the Solution of Electromagnetic Integral Equations

Approved by:

Dr. Andrew F. Peterson, Advisor
School of Electrical and Computer Engineering
Georgia Institute of Technology

Dr. Waymond R. Scott
School of Electrical and Computer Engineering
Georgia Institute of Technology

Dr. Emmanouil M. Tentzeris
School of Electrical and Computer Engineering
Georgia Institute of Technology

Date Approved: June 15, 2011

ACKNOWLEDGEMENTS

I am highly thankful to my supervisor, Professor Andrew F. Peterson, for helping me and supporting me throughout my PhD research. Most of the material presented in this dissertation was developed after countless discussions with him.

I would like to thank all my friends at Georgia Tech especially Mohammad Omer and Farasat Munir for their help, support, and company during my stay at Georgia Tech especially during initial days. My special thanks go to my past roommates Amil Haque and Faisal Shah for their company and support.

My special thanks go to my parents, particularly to my mother, who has been supporting me at every turn of my life. Long may she live, happy and healthy, together with me and I serve her to earn the eternal rewards. I am very thankful to my wife and my son for their love and support and for providing me with a beautiful environment at home.

I am highly indebted to the United States Educational Foundation in Pakistan (USEFP) and the US Department of State for awarding me the Fulbright fellowship for the MS studies at Georgia Tech. Moreover, I am highly thankful to the School of ECE at Georgia Tech for supporting me for my PhD studies at Georgia Tech through a Graduate Teaching Assistant (GTA) position. I am particularly thankful to the GTA selection committee including Professors Ferri and Hertling for awarding me this competitive position continuously for more than two years. Without that, a PhD study at Georgia Tech was not a possibility. My thanks and regards also go to my short-time supervisor, Dr. Joy Laskar, for his help and support and particularly for his recommendations for my first GTA position. Moreover, my special thanks to Professor Peterson for arranging the last semester (summer) GRA.

Contents

LIST OF FIGURES

CHAPTER 1

INTRODUCTION

With the advent of various modern communication systems, and the limited size of the electromagnetic (EM) spectrum, circuits and systems are being designed at higher frequencies where bandwidth is available to accommodate communication services. Design at high frequencies requires the use of full-wave EM solvers in addition to circuit solvers. Moreover, apart from radiation and scattering problems that definitely require numerical EM solvers, there is an increasing trend towards the use of various exotic materials (e.g. different polymers, organic materials, and recently graphene) for devices, substrates, packages, and various coatings. Computational EM techniques are required to characterize and model the behavior of these materials at high frequencies. One of the goals of numerical EM analysis is to achieve reasonable accuracy in the least possible time (minimize the computational workload) so as to assist the real-time design process. This dissertation explores various adaptive methods in an attempt to achieve this goal for integral equation based EM formulations.

For many years, standard techniques for solving electromagnetic integral equations convert the continuous equation into a linear system that can be solved numerically using a computer. The most widely-used technique is known as the *method of moments* (MoM). The procedure begins by dividing the problem domain (the scatterer surface, for example, in a scattering analysis) into cells to create a discrete model called a *mesh*. The unknown quantity to be determined, usually the current density on the surface of interest, is represented as a weighted summation of basis functions. Each basis function has its domain of support limited to at most a couple of cells of the mesh. Let us suppose that there are N basis functions. The coefficients of

the basis functions are the unknowns to be determined. By substituting the weighted sum representation of the unknown into the integral equation, a residual function can be defined. The residual is forced to be orthogonal to a set of N testing functions, also defined on the mesh of the surface, to form an N by N system of equations that can be solved for the unknown coefficients. The MoM is sometimes known as the *weighted residual method* since the residuals of the integral operator are weighted with the testing functions to obtain the linear system of equations. The MoM technique is described in detail in Chapter 2.

While the MoM is the most widely-used approach for solving electromagnetic integral equations, alternative approaches based on the Nyström method are also in use. The Nyström and locally-corrected Nyström (LCN) methods involve approximating integrals over cells of the mesh with quadrature rule summations. Samples of the current at the nodes of the rule are the unknowns. The integral equation is enforced at quadrature nodes to obtain an N by N system of equations. The LCN method is a variation of the classical Nyström method that can treat the singular integrands arising in electromagnetic integral equations. This technique will be explained in Chapter 2. The Nyström and LCN methods may be more efficient than the MoM when higher-order representations are employed, and thus we consider them for use in adaptive solution schemes that involve changing the order of the representation.

Numerical solution techniques have various sources of error. Strictly speaking, the unknown resides in an infinite-dimensional space and the MoM and LCN essentially find its orthogonal projection onto a finite-dimensional space, naturally incurring the error. This *discretization error* is usually the largest source of error in the numerical result. Other sources of error in the final solution arise from inaccurate geometrical modeling, inaccuracies in the quadrature rules used to carry out various integrations, and different approximations used to

simplify the integral equation formulations. In most practical problems, the error distribution is not uniform throughout the problem domain.

Adaptive refinement techniques are sophisticated numerical algorithms that work with the MoM or LCN to adjust the mesh density or the representation order locally, in an attempt to achieve a fairly uniform error distribution in the final numerical solution. Ideally, the user of an adaptive technique can "dial in" a desired accuracy level and the algorithm will iteratively adjust the numerical results until they meet the accuracy criterion. The adaptive refinement procedure involves three main components: an error estimator, a control algorithm, and the ability to refine the mesh or the order of representation and re-solve the problem. The most important component is the error estimator. A typical error estimator accepts the mesh and initial solution as input variables and generates an estimate of the error distribution on the mesh. Many research articles describe error estimation techniques for the numerical solution of differential equations using finite element techniques, but relatively few have been written on error estimators for integral equation formulations. Among the few estimators that have been studied, none are as reliable and computationally inexpensive as desired. This dissertation investigates several novel error estimation techniques for integral equation formulations of electromagnetic fields. The accuracy and computational cost of these estimators are evaluated for a number of different problems. For illustration purposes, the best-performing estimators are used in rudimentary adaptive refinement procedures.

In the following chapters, we first review the discretization methods and the literature on error estimators and adaptive refinement procedures. We then investigate several residual-based error estimators for the MoM discretization of an integral equation. These estimators are evaluated for a number of two-dimensional electromagnetic scattering problems involving

conducting structures. The specific MoM approach we used was limited to the use of piecewise linear basis functions, and thus it is suitable for an adaptive refinement procedure where the mesh cell sizes are adjusted in order to improve the error distribution. Such an approach is known as *h-refinement*. In order to more easily consider an adaptive refinement procedure where the polynomial order of the representation is adjusted, known as *p-refinement*, we also consider the use of the LCN method to discretize the integral equation. As the polynomial order increases, the LCN method usually involves smaller matrix fill times, and is therefore computationally cheaper than the MoM approach. Curved cells are used to accurately model the target surfaces with the higher-order LCN technique.

In conjunction with the LCN approach, we present various *explicit* error estimation techniques and use them to carry out adaptive *p*-refinement for a number of problems. Explicit techniques are those in which the error estimator accepts an initial numerical result as input and provides an estimate of the error in that result. We also consider an *implicit* estimator for the LCN approach. Implicit error estimators generate an error estimate based primarily on the problem mesh, and may or may not require an initial numerical result. (Normally, they solve subsets of the entire problem to obtain the error estimate, which may be more efficient than solving the entire problem.) The relative advantage and performance of the explicit and implicit estimators will be judged. While the numerical examples included in this work are two-dimensional, the various estimators and the theoretical approach are directly applicable to 3D formulations.

Original contributions of this dissertation include:

1. The development and evaluation of several residual-based explicit error estimation techniques for the MoM solution of electromagnetic integral equations.

2. The implementation of a simple *h*-refinement algorithm for use with the MoM.

3. The development and evaluation of several explicit error estimators for use with the LCN solution of electromagnetic integral equations.

4. The development of an implicit error estimation technique for the LCN method.

5. The implementation of adaptive *p*-refinement techniques for electromagnetic integral equations based on the LCN method.

6. A discussion of some of the theoretical issues associated with the error estimation process.

This dissertation is organized as follows. Chapter 2 introduces the reader to the solution techniques considered in this dissertation, the MoM and the LCN methods. It also presents a survey of the literature on error estimation and adaptive refinement techniques for numerical electromagnetics. Chapter 3 presents several error estimation methods for use with the MoM discretization procedure. Three estimators are implemented for various prototype problems, their accuracy and computational cost is studied, and a simple *h*-refinement implementation is illustrated. Chapter 4 presents an analogous investigation of explicit error estimators for use with the LCN method. It also presents their implementation for a number of problems and illustrates the performance of an adaptive *p*-refinement technique for the LCN method. In Chapter 5, an implicit error estimation technique and the corresponding adaptive refinement implementation is presented for the LCN method. Chapter 6 discusses the error estimation process from a more

theoretical perspective, and studies the possibility of scaling the residual estimators using norms of the inverse operator to improve their accuracy. Finally, Chapter 7 concludes this dissertation and provides suggestions for future research in this area.

CHAPTER 2

NUMERICAL TECHNIQUES FOR THE SOLUTION OF ELECTROMAGNETIC INTEGRAL EQUATIONS AND A SURVEY OF THE PAST RESEARCH ON ADAPTIVE TECHNIQUES

In this chapter, we review the two solution techniques that we will be using in our work for solving integral equations: the method of moments (MoM) and the locally-corrected Nyström (LCN) methods. We also summarize the literature on adaptive techniques and error estimation methods as used for integral equations in computational electromagnetics.

2.1 The method of moments

The MoM (or the weighted residual method or boundary element method) is a numerical technique to solve integral equations by converting them into a finite-dimensional linear system [1-4]. The system is subsequently solved numerically using a computer. Consider the generalized equation

$$L\{f\} = g\,, \tag{2.1}$$

where L is a linear operator, g is a known excitation (a uniform plane wave in scattering problems, for example), and f is the unknown function to be determined (the current density, for example). An inner product $\langle t, g \rangle$ is defined in the range space of the operator L. The inner product is defined as the integration of the product of the two functions over that space. The function f is represented by a sum of N weighted basis functions:

$$f = \sum_{n=1}^{N} a_n f_n\,. \tag{2.2}$$

Substitution of this expansion in (2.1) yields:

$$\sum_{n=1}^{N} a_n L\{f_n\} \cong g\,, \tag{2.3}$$

where the residual is:

$$R = g - \sum_{n=1}^{N} a_n L\{f_n\}\,. \tag{2.4}$$

The essence of the MoM lies in using a set of *testing* or *weighting* functions $\{t_m\}$ such that an inner product of each testing function with the residual is equated to zero, yielding

$$\sum_{n=1}^{N} a_n \langle t_m, L\{f_n\}\rangle = \langle t_m, g\rangle, \tag{2.5}$$

Assuming that we use N testing functions, the result is a linear system of order N

$$\mathbf{Za} = \mathbf{b}, \tag{2.6}$$

where $\mathbf{Z}$ is the N by N "impedance" matrix with entries

$$z_{mn} = \langle t_m, L\{f_n\}\rangle, \tag{2.7}$$

and $\mathbf{b}$ is the right hand side vector with entries

$$b_m = \langle t_m, g\rangle\,. \tag{2.8}$$

Equation (2.6) can be solved using various linear system solution algorithms such as direct factorization techniques or iterative algorithms [4] to yield the set of unknown coefficients $\mathbf{a} = \{a_n\}$. The coefficients can be substituted in (2.2) to complete the solution.

Various functions have been used as basis functions and testing functions within the MoM discretizations. Basis functions are often piecewise constant, piecewise linear, or some other relatively simple polynomial function. Generally, the accuracy of the numerical result depends primarily on the choice of basis functions and on how well those functions can represent the solution. Testing functions may or may not have a direct relation to the basis functions. Testing functions may also be simple polynomials. If Dirac delta functions are used as testing functions, the resulting technique is called *Point Matching* or *Collocation*, which essentially means that boundary conditions are matched only at discrete locations throughout the solution domain. Another commonly used choice, named *Galerkin's method*, incorporates the same set of functions for testing as is used for the basis functions. In Galerkin's approach, boundary conditions are enforced throughout the solution domain in an average sense.

2.2 The Locally-corrected Nyström method

The LCN method is another technique for solving integral equations [5]. It is a variation on the classical approach of Nyström, in which an integral operator is replaced with a suitable quadrature rule over each cell. The unknown quantity, such as the current density in scattering problems, is represented by its samples at the quadrature nodes. The integral equation is enforced at the same node points to obtain a system of equations, the solution of which gives an approximation to the unknown quantity. LCN implementations usually enforce the integral equation at points (analogous with the use of Dirac delta testing functions within the MoM). The accuracy of the solution depends on the quality and order of quadrature rule. In the classical Nyström approach, there are no inner products to be computed, making the approach computationally cheaper than the MoM.

A fundamental difficulty arises with the classical Nyström approach when the integral equation being solved does not have a bounded kernel over the problem domain. Most integral equations of electromagnetics involve a singular kernel, and in fact most are infinite at one point in the domain. For example, the electric field integral equation, to be used in Chapters 3-6, has a kernel that is infinite when its argument is zero. In such cases, the direct sampling of the equation is not possible. The LCN method was developed to provide an alternate approach that is similar to the classical Nyström method, but is applicable to equations with singular kernels. The *local-correction* procedure involves replacing the unbounded kernel with a suitably constructed bounded kernel near the singularity. Near the singularity, the bounded kernel is sampled instead of the original kernel. Some distance away from the singularity, the direct sampling of the original kernel will still suffice.

In the classical Nyström approach, a general integral operator with the current density as the unknown and a kernel K is sampled by a q-point rule, with weights $\{w_{ni}\}$ and nodes $\{t_{ni}\}$ in the n-th cell, according to

$$\int_{cell\ n} J_t(t')K(t_{mj},t')dt' \cong \sum_{i=1}^{q} w_{ni} J_t(t_{ni})K(t_{mj},t_{ni})\,. \tag{2.9}$$

This discretization is suitable if K is bounded over the domain defined by the n-th cell. Otherwise, we use the local-correction process to replace K by a new bounded kernel L, which is sampled in place of K:

$$\int_{cell\ n} J_t(t')K(t_{mj},t')dt' \cong \sum_{i=1}^{q} w_{ni} J_t(t_{ni})L(t_{mj},t_{ni})\,. \tag{2.10}$$

The kernel L in Equation (2.10) is synthesized by matching the near fields of some hypothetical currents at the nodes of the quadrature rule. (In this manner, the original kernel is "locally

corrected" to obtain the bounded kernel.) The hypothetical currents are just a set of basis functions, $\{B_k(t)\}$, such as the Legendre polynomial functions defined on one cell. The actual near field of each basis function is equated with the near field obtained by applying the quadrature rule to the bounded kernel, yielding

$$\sum_{i=1}^{q} w_{ni} B_k(t_{ni}) L(t_{mj}, t_{ni}) = \int_{cell\ n} B_k(t') K(t_{mj}, t') dt', \tag{2.11}$$

at each location t_{mj} where L is needed, and for each basis function in the set. For q basis functions in the set $\{B_k(t)\}$, equation (2.11) yields the following system at one observer location (fixed t_{mj}):

$$\begin{bmatrix} B_1(t_{n1}) & B_1(t_{n2}) & \cdots & B_1(t_{nq}) \\ B_2(t_{n1}) & B_2(t_{n2}) & \cdots & B_2(t_{nq}) \\ \vdots & & & \vdots \\ B_q(t_{n1}) & B_q(t_{n2}) & \cdots & B_q(t_{nq}) \end{bmatrix} \begin{bmatrix} w_{n1} L(t_{mj}, t_{n1}) \\ w_{n2} L(t_{mj}, t_{n1}) \\ \vdots \\ w_{nq} L(t_{mj}, t_{n1}) \end{bmatrix} = \begin{bmatrix} \int_{cell\ n} B_1(t') K(t_{mj}, t') dt' \\ \int_{cell\ n} B_2(t') K(t_{mj}, t') dt' \\ \vdots \\ \int_{cell\ n} B_q(t') K(t_{mj}, t') dt' \end{bmatrix}. \tag{2.12}$$

This system can be solved to yield the required samples of L, $L(t_{mj}, t_{n1})$ through $L(t_{mj}, t_{nq})$. A similar system must be solved for each of the observer locations t_{mj} in the near field of cell n.

In the LCN approach, the bounded kernel L is used near the singularity, where "near" typically implies points in the same cell and points outside the cell within some fixed distance, such as within one quarter of the wavelength. The computational overhead of generating the bounded kernel is limited to a fraction of the matrix entries; thus the LCN approach is almost as efficient as the classical Nyström method.

2.3 Adaptive refinement techniques in the literature

We focus the following literature review on error estimation and adaptive refinement techniques applicable to boundary element methods (integral equation formulations). Many articles on these topics have been written for the differential equation/finite element approach, and reviews of those are available [6-12]. We single out the PhD dissertation of Botha [6] and the references therein (207 of them!) and the book by Ainsworth and Oden [7] as excellent references on adaptive techniques for differential equation formulations.

Although the numerical treatment of integral equations has steadily advanced for decades, adaptive refinement procedures have lagged behind other developments. Adaptive refinement is an approach where either the mesh density or the order of representation in certain regions of the mesh is automatically modified as required to improve the accuracy of the approach, without user intervention. The main components of an adaptive technique are error estimation, a control algorithm, and the ability to refine the mesh or the representation [13]. The goal of an adaptive refinement solution is to reliably achieve a desired error level throughout the problem domain, while minimizing the computational cost of obtaining that level of accuracy.

Adaptive refinement procedures are of three main types; *h*-refinement, *p*-refinement, and *r*-refinement [13]. There are also variations on these approaches that use combinations of any two of these techniques, for example, *hp*-refinement. In an *h*-refinement technique, the mesh density is adaptively refined without changing the order of representation, whereas in *p*-refinement, the polynomial degree of the representation employed in certain regions of the mesh is adaptively adjusted without changing the mesh density. In an *r*-refinement approach, mesh points are relocated to form a new local mesh. All these techniques have been extensively

studied in the literature when applied to the finite element analysis of differential equations [8-12]. In contrast, relatively few research articles have addressed adaptive refinement techniques for integral equation formulations. These refinement techniques have their own advantages and disadvantages. For example, *h*-refinement requires the problem domain to be successively re-meshed, while *p*-refinement can be carried out without the need to change the mesh. Since the polynomial order of the representation used within the Nyström approach can be changed by the simple expedient of changing the quadrature rule, *p*-refinement with the Nyström method requires essentially no additional computation per matrix entry [5]. In contrast, the MoM discretization involves inner product computations that become more costly as the polynomial degree of the basis functions increases. The LCN procedure retains most of the computational efficiency of the classical Nyström technique, and is also favorable for *p*-refinement implementations.

The most important component of an adaptive technique is the error estimator. All the adaptive techniques rely on some sort of error estimation procedure to identify the local regions of the problem domain where refinement needs to be done to improve the overall accuracy of the solution. Therefore, a reliable, computationally inexpensive, and elegant error estimation scheme is a vital component of any adaptive refinement scheme. As mentioned previously, many research articles describe error estimation techniques for the numerical solution of the differential equation formulations [6-12] but few have been written on error estimation for the numerical solution of the integral equations. Among those few, none are as reliable and inexpensive as desired.

Error estimators can be used in two ways. For a rudimentary adaptive refinement algorithm, a user may draw upon his or her experience to provide an initial mesh and degree of

representation that should be suitable to provide the desired accuracy. In that case, the error estimator must accurately identify the regions of the problem where the numerical error is relatively large, compared to the average error level in the result, so that the solution accuracy in those regions may be refined to a level comparable to the rest of the problem domain. In that application, it may not be essential that the error estimator produces an accurate global estimate of the error level, just that it be able to distinguish between small and large errors. On the other hand, an accurate global error estimate may be desired, to provide the user with additional confidence in the numerical result or to eliminate the need for any particular user expertise. The most sophisticated adaptive approaches would permit the user to "dial in" the desired accuracy level and carry out the computations until that level is reached.

Some of the common factors affecting error in a numerical solution are the smoothness of the surface of the structure being considered, the degree of geometrical modeling (faceting or curved cells), the type of kernel (singular, hyper-singular, or analytic) within the integral operator, the accuracy of the quadrature used to carry out numerical integrations, the polynomial order of the expansion and the testing functions, and the algorithms used to solve the linear system of equations [4, 13].

Previous work on error estimation in the boundary element methods can be classified into two main types. First are the empirical techniques based on numerically solving and applying various heuristics to estimate the error, and testing them on a number of canonical problems, and second are the theoretical approaches of mathematics based on functional analysis and operator theory. Although most of the computational electromagnetics community has used empirical approaches for error estimation, there are a few researchers who have adopted theoretical approaches. For example, Warnick and Chew [14] present a theoretical understanding of the

error behavior of the MoM applied to integral equations. References [14-15] review some of the important factors that cause error in MoM simulations. These authors also obtain theoretical error rates for surface currents and far fields for several canonical problems such as circular cylinders and flat strips.

Mathematical approaches to error analysis have also been developed to study the convergence of the numerical result to the correct solution and the asymptotic convergence rate of the error. For a given polynomial degree *p*, error is often found to decay asymptotically according to some power of the mesh size, such as $O(h^{p+1})$, as the nominal mesh dimension *h* is refined. Our intent here is not to tackle the theoretical approaches to error analysis, which are quite complicated, but to point the reader to this important body of knowledge and to acknowledge its important results and possibilities of error bounds. Interested readers are referred to a recent book by Warnick [15] and to the articles [16-17].

Articles by Hsiao and Kleinman [16-17] consider an MoM formulation in terms of mapping properties of the integral operator in appropriate function spaces (Sobolev spaces due to finite energy possessed by field quantities). They provide a mathematical discussion of the residual error and derive appropriate bounds on the condition number of the impedance matrix resulting from discretization of the integral operator.

In [16-17], Hsiao and Kleinman provide a strong rationale for the use of the *residual* of the solution as a measure of the actual error. In the general equation

$$L\{f\} = g\,, \tag{2.13}$$

if f_a denotes the approximation of the exact solution *f*, then the residual is defined as:

$$R = g - L\{f_a\}. \tag{2.14}$$

The residual in (2.14) provides a measure of the error in the approximate solution f_a. The actual error in the approximation is $f - f_a$. The exact solution is usually unknown, and therefore the actual error is not immediately available, but we can use the residual error as a measure of the actual error if the problem being solved is *well-posed*. Inverse problems, e.g. inverse scattering, are often *ill-posed* because there may be more than one solution to the problem. Direct problems of radiation and scattering that we consider here have a unique solution and are usually well-posed, and consequently residual based error estimation is a viable option.

Equation (2.14) can be manipulated, using (2.13) and the linearity property of the operator *L*, to compute the actual error in the approximation as follows:

$$R = L\{f\} - L\{f_a\} = L\{f - f_a\}, \tag{2.15}$$

$$f - f_a = L^{-1}\{R\}. \tag{2.16}$$

This calculation is possible if a unique solution exists, as it should for well-posed problems, and if the inverse operator can be obtained. In practice, the inverse operator must be obtained using the MoM or LCN approaches, and therefore is at best an approximation to L^{-1}.

Numerical solution procedures to compute the residual proceed as follows. An *N* by *N* matrix operator **Z** can be obtained using the MoM or LCN approaches, as described in Sections 2.1 and 2.2, and used to obtain an approximate solution f_a by solving Equation (2.6). However, the residual associated with the system of equations in (2.6) will be identically zero since f_a exactly satisfies those equations. In order to estimate the residual error, a new system of

equations must be defined at points independent of those used to construct the original system. Consequently the cost of computing the residual R over the problem domain involves creating a second system of equations, which is as expensive as creating the original system of equations. For a general MoM system, this is an $O(N^2)$ operation, where N is the number of unknowns in Equation (2.2). The solution of Equation (2.6) is usually an $O(N^3)$ operation. Therefore, for large N, the cost of the residual computation is asymptotically small compared with the cost of obtaining f_a. However, even though the cost only grows at an $O(N^2)$ rate, it still may be relatively expensive to compute the entries of the second system.

It may be desired to obtain a direct solution error estimate using equation (2.16). The inverse operator L^{-1} is not available, but could be approximated by the inverse matrix for the second system of equations (the system used to obtain the residual). Assuming that the second system is also N by N, the computation in (2.16) adds an additional $O(N^3)$ operations, so the cost of that error estimate is approximately twice the cost of obtaining the approximate solution in the first place. This computational cost is usually judged to be prohibitive for routine calculations. Furthermore, the second system of equations may not provide a more accurate description of the problem than the original system.

Reference [18] investigated the calculation of Equation (2.16) for linear wire problems. The specific approach involved the use of a relatively small system of equations to initially determine f_a and a significantly larger system of equations to calculate the residual R and the error $f - f_a$. (The use of a larger system was to ensure that the reference solution f was more accurate than the initial result f_a.) The authors of [18] used the approach to judge the relative performance of different types of basis functions, and suggested that it could be used to place

error bars on computational results. They also conceded that it was rather expensive to implement, and therefore not practical for routine error estimation.

While the cost of the error estimate in (2.16) is an $O(N^3)$ operation, the cost of directly computing the residual is only an $O(N^2)$ operation. There are many reports of error estimators based on residual calculations. Reference [13] surveys more than 100 papers from the mechanical engineering literature on error estimators for integral equations, and summarizes many papers that focus on residual estimators for Laplace's equation and the equations of elasticity. The earliest work in the electromagnetics literature appears to be [8], which briefly mentions one approach for calculating the residual error for electromagnetic integral equations. (The primary emphasis of [8], like [9-12], is on hybrid formulations involving differential equations coupled with integral equations.)

Reference [19] employed a residual-based error estimator for electromagnetic scattering from wire structures. The authors of [19] used an approximate technique for calculating the near-zone fields when computing the residual, to improve the efficiency of the residual calculations. Reference [20] also proposed a residual calculation to determine the error associated with electromagnetic scattering from three-dimensional conducting bodies. No major attempts were made to improve the efficiency of the residual calculation.

An alternate way to calculate the residual is to form an over-determined system of equations and solve it using a least-square type of algorithm. That approach produces the initial solution and simultaneously an estimate of the residual error (since the least-square result will not usually produce a zero residual). Reference [21] employed this approach for dipole antenna problems solved using both the MoM and the LCN. A similar approach was used in [22] and

[23] for a variety of problems. The solution of an over-determined system is more expensive than that of a square system; for a 2:1 over-determined system the coefficient of the $O(N^3)$ term in the operation count increases by at least a factor of five [24].

It should also be noted that a well-posed problem can sometimes be *ill-conditioned*. An ill-conditioned problem is one where small changes in the input data cause large changes in the result; such problems usually give rise to linear systems that have a large matrix condition number. The integral equation formulations that we consider for electromagnetic scattering problems can sometimes become ill-conditioned due to the well-known effects of internal resonances and low-frequency breakdown. Corners and edges, if not treated properly, may also result in higher matrix condition numbers [23]. Residual based error estimates become inaccurate for ill-conditioned problems, meaning that the residual may indicate a small error in the solution ($\|g - L\{f_a\}\|$ is small) even though the actual error ($f - f_a$) may be large.

In the following chapters, we will investigate several techniques for computing residual-based error estimates, with an eye toward determining the trade-off between the accuracy and computational cost of each approach.

Another approach to error estimation involves comparing a numerical result with a second result obtained using a higher-order representation of the unknown or a result obtained with a finer mesh to better approximate the exact solution. An approach of this type is proposed by the authors of [25], who use a higher-order representation on a local mesh with an MoM solution procedure. The difference between the two results is computed using a suitable norm (an L_2 norm or a Sobolev norm, for example, for functions that are not square integrable). This provides an error estimate

$$error = \frac{\|f - f_a\|}{\|f\|}, \tag{2.17}$$

where f is the reference solution, the "better" approximation to the exact solution as described earlier. This approach is valid only if the reference solution is really more accurate than the numerical result. Chapter 5 describes an implementation of a similar technique in the context of the LCN.

Since currents on smooth surfaces should be continuous functions, researchers sometimes use the discontinuity of the current (in places where the representation does not impose continuity) as a direct measure of the local error. Variations on this procedure have been studied in the mechanical engineering literature [13], and have also been used in electromagnetics [26-27]. In vector electromagnetic problems, the formulation may force the normal component of the current density to be continuous across cell boundaries while allowing the tangential component of the current density to jump; in that case the tangential component would provide the error estimate. For example, Wang and Webb [27] demonstrate higher-order triangular-cell basis functions that impose the normal continuity of the surface current on element edges. The authors use the discontinuity in the tangential component of the surface current, computed on a common edge connecting two elements, as a measure of the numerical error. The element error is taken to be the maximum of all the three edge errors. Since the basis functions were designed to have continuous normal components, there will be no discontinuity in that component. This scheme is designed for smooth surfaces, where the current density has a continuous tangential component. Edges that correspond to true sharp edges of the scatterer are left out in computing the error indicator since the tangential component of the surface current will be infinite or possibly discontinuous there. Using this error indicator, the authors of [27] demonstrate a very simple *p*-

adaption scheme where at *i*-th step, some percentage of the elements with the highest error indicators are upgraded to the next higher order.

A related measure is a derivative discontinuity in the current (analogous to discontinuities in the gradient of the field in differential equation formulations) [9], [10]. While such an approach has not yet been reported for electromagnetic integral equation formulations, a derivative discontinuity estimator is considered in Chapter 4.

The above techniques attempt to provide an estimate of the error in a specific numerical result. These are termed *a posteriori* estimators in the literature. Some of them are *explicit* while others are *implicit*. Explicit techniques produce an error estimate from the solution itself or by using the same equation that was solved to produce the original result, while implicit techniques attempt to solve a separate equation (usually a much smaller system of equations in practice) to determine the error in the original result. *A priori* techniques do not involve a specific result and are mainly used to establish stability, convergence, and the asymptotic behavior of the solution. Thus, a priori techniques are not used in refinement schemes [6, 7], and will not be considered in this work.

CHAPTER 3

ERROR ESTIMATION TECHNIQUES AND ADAPTIVE REFINEMENT FOR THE METHOD OF MOMENTS

In this chapter, we investigate several methods for estimating the local (cell-by-cell) error associated with a method of moments (MoM) solution of the electric field integral equation (EFIE). Several different residual error estimators are used with a variety of prototype structures. The global error estimates show correlation with the actual current density errors, and all three local error estimates are shown to correctly identify the high-error regions. A simple *h*-refinement procedure is also illustrated.

3.1 Introduction

Electromagnetic field problems often involve the prediction of fields in the presence of complicated structures, and the solution of these problems usually rests upon computational procedures. Integral equation formulations have been widespread, and are discussed in several texts [1-4]. The typical numerical solution process involves creating a subsectional mesh model for the surface of any structure, representing the equivalent surface currents on that surface by a piecewise-polynomial representation, and imposing boundary conditions on the fields to construct a large linear system of equations. The solution of that system produces the coefficients of those polynomial basis functions. That process is known as the *method of moments* or the *boundary element method*. Although the numerical treatment of integral equations has steadily advanced for decades, adaptive refinement procedures have lagged behind other developments. Adaptive refinement is an approach where either (a) the mesh density, or (b) the polynomial

degree employed in certain regions of the mesh, is automatically modified as required to improve the accuracy of the approach, without user intervention. Such modification must be based on an estimate of the local error [6-27].

In the present study, we consider the transverse-electric (TE)-to-*z* EFIE for two-dimensional conducting structures. The continuous equation being solved can be expressed as:

$$\bar{L}\left\{\bar{J}\right\}_{\tan} = \bar{g}_{\tan}, \tag{3.1}$$

where $\bar{J}$, the electric current density, is the quantity of interest,

$$\bar{L}\left\{\bar{J}\right\} = \frac{1}{j\omega\varepsilon}\left\{\nabla\nabla\bullet + k^2\right\}\int \bar{J}(t')\frac{1}{4j}H_0^{(2)}(k|\bar{r}-\bar{r}'|)dt', \tag{3.2}$$

and

$$\bar{g} = -\bar{E}^{inc}(\bar{r}), \tag{3.3}$$

where $\bar{E}^{inc}$ is the given excitation, $H_0^{(2)}$ is the zero-order Hankel function of the second kind, t and t' denote parametric variables along the contour of the structure, and $\bar{r}$ is the position vector from t' to t on the contour.

The numerical solution for the current density is obtained in terms of a representation in N basis functions:

$$\bar{J}_N(t) = \sum_{n=1}^{N} J_n \bar{B}_n(t). \tag{3.4}$$

The surface of the conducting scatterer is represented by flat facets, while the current density is represented by an expansion using piecewise-linear or "triangle" basis functions $\{\bar{B}_n(t)\}$ that are tangential to the surface. Each triangle function straddles two of the facets in the surface model. A weighted-residual approach is employed using piecewise-constant or pulse

testing functions $\{\bar{T}_m(t)\}$, also tangential to the surface and partially straddling adjacent cells, to construct a system of equations that may be expressed in matrix form as

$$\mathbf{ZJ} = \mathbf{E}. \tag{3.5}$$

The entries of the N by N system matrix and the N by 1 excitation vector are given by

$$Z_{mn} = \int \bar{T}_m \bullet \bar{L}\left\{\bar{B}_n\right\} dt, \tag{3.6}$$

and

$$E_m = \int \bar{T}_m \bullet \bar{g}\ dt. \tag{3.7}$$

Other details of the numerical solution procedure, including approximations that were used in the computation of Z_{mn}, are described in section 2.4 of [4].

As discussed in Chapter 2, local error estimators are often based on residual error computations. Once the coefficients in (3.2) have been determined, the tangential residual associated with this numerical result can be written as:

$$R_{\tan}(t) = \bar{L}\left\{\bar{J}_N\right\}_{\tan} - \bar{g}_{\tan}. \tag{3.8}$$

The residual error is known to correlate with the actual error $\bar{e} = \bar{J} - \bar{J}_N$ [16-17], and has formed the basis for determining solution error in various integral equation formulations [22, 28]. However, it is relatively expensive to compute, since it usually must be evaluated using an approach that is independent from that used to construct the original linear system.

In the following [29], we consider several different error estimators related to (3.8), and compare their performance and computational efficiency on a number of canonical scattering targets. One estimator is implemented in a simple *h*-refinement scheme for illustration.

3.2 Tangential residual error estimator

The TE EFIE imposes the tangential-field boundary condition:

$$E_{\tan}^{tot} = 0 \tag{3.9}$$

indirectly, by equating the average value of the residual in (3.8) over the domain of the testing function to zero. In other words, in the construction of the linear system in (3.5), equation (3.9) is imposed in an average sense by integrating it with a piecewise-constant testing function from the center of one cell to the center of the adjacent cell. In the preceding notation, this is equivalent to imposing:

$$\int R_{\tan}(t)dt = 0\,, \tag{3.10}$$

over the domain of each pulse testing function.

The residual in (3.10) provides a means to measure the error in a particular result, and is directly computable since it does not depend directly on the exact solution. If we compute the residual error in the same manner as was used to construct the linear system in (3.5), we do not obtain useful information since the equations are exactly satisfied. However, we could re-compute the residual error in a variety of ways to obtain an independent measure of the residual error.

Consider the use of weighting functions that are centered within each cell with their widths made relatively small (1/5 of the cell width in this case). In that case, the residual error at the center of cell *i* may be obtained as:

$$R_t(t_i) = \int_{small\ domain\ at\ center\ of\ cell\ i} R_{\tan}(t)dt\,, \tag{3.11}$$

where $R_{\tan}$ is computed from the previously-obtained numerical values for the current density, using essentially the same subroutines as used to compute the matrix entries Z_{mn}.

The normalized tangential residual error in the i^{th} cell may be defined as:

$$TR_i^{loc} = \frac{|R_t(t_i)|}{|\bar{g}|_{\max}}, \tag{3.12}$$

to provide a local measure of the error. For a global measure of the error, we employ the 2-norm error obtained by summing (3.12) over all the cells in the model:

$$TR_2^{glo} = \sqrt{\frac{1}{N}\sum_{i=1}^{N}(TR_i^{loc})^2}\ . \tag{3.13}$$

As a consequence of the definition of the residual in (3.11), these error measures are relatively independent of the system of equations that led to the specific numerical solution being evaluated.

3.3 Normal residual error estimator

In the preceding section, a residual error estimator was constructed based on enforcing the tangential field boundary condition. An additional boundary condition should be satisfied by the normal component of the total electric field at the surface of a perfect conductor, namely:

$$\hat{n} \bullet \bar{E}^{tot} = \frac{\rho_s}{\varepsilon}, \tag{3.14}$$

where ρ_s denotes the surface charge density at a point on the surface, ε denotes the permittivity of the exterior medium, and $\hat{n}$ is an outward-directed unit vector perpendicular to the surface. The boundary condition of (3.14) may be expressed in the form of an alternative residual:

$$N(t) = \hat{n}(t) \bullet \left(\bar{L}\left\{\bar{J}_N\right\} - \bar{g}\right) + \frac{1}{j\omega\varepsilon}\frac{d\{\hat{t}(t) \bullet \bar{J}_N\}}{dt}, \tag{3.15}$$

which uses:

$$\rho_s = -\frac{\nabla_S \bullet \bar{J}_N}{j\omega} = -\frac{1}{j\omega}\frac{d\{\hat{t}(t) \bullet \bar{J}_N\}}{dt}. \tag{3.16}$$

For ease of computation and employing the same subroutines used to build the matrix in (3.5), we orient the testing functions so that they are normal to the cells, at the cell center, and compute the normal residual in the i^{th} cell using:

$$NR_i^{loc} = \frac{1}{|\bar{g}|_{\max}} \int_{\text{perpendicular to cell } i} N(t)dn\,, \tag{3.17}$$

where the testing domain is typically on the order of the cell size. The global error NR_2^{glo} is obtained in the same manner as in equation (3.13).

3.4 Error estimation based on an over-determined system of equations

A third way to compute a residual is to set up and solve an overdetermined system of equations representing (3.1), by employing more testing functions (over smaller domains) than basis functions when constructing equation (3.5) [22-23, 28]. A least-squares approach can be used to obtain a solution that minimizes the error in the residual equations. Since the equations will not be exactly satisfied, the residual can be computed from the equations and used directly as a measure of the error in the numerical result [23].

We use an implementation where the cells are divided in half, each with a tangential testing function centrally located, to yield a $2N$ by N system:

$$\mathbf{Z}_{2N\times N}\mathbf{J}_N = \mathbf{E}_{2N}\,. \tag{3.18}$$

After the current coefficients are determined by a least-square solution, the residual function is computed as the matrix column vector:

$$R_{OD}(t_i) = Z_{2N\times N}J_N - E_{2N}^{inc}\,. \tag{3.19}$$

The normalized tangential residual error at location i may be defined as:

$$ODR_i^{loc} = \frac{|R_{OD}(t_i)|}{|\bar{g}|_{\max}}\,. \tag{3.20}$$

A global function is obtained by summing over the 2*N* locations in accordance with (3.13).

3.5 Simulation results

In the following, we compare the performance of the preceding three error estimators on several geometries. We also estimate the actual error in each numerical result by comparison to a numerical result obtained with a finer discretization of the target. A local value for the normalized error in the *i*-th cell is obtained as:

$$NE_i^{loc} = \frac{\left|\bar{J}_{ref}(t_i) - \bar{J}_N(t_i)\right|}{\max\left|\bar{J}_{ref}(t_i)\right|}, \tag{3.21}$$

with the global estimate obtained following (3.13).

Figure 3.1(a) shows the geometry of the first problem, which is a circular cylinder of 5λ circumference illuminated with two line sources placed (as shown) at a distance of 0.1λ from the cylinder surface. Each of the line sources produces an incident field of the form

$$\overline{E^{inc}} = j\eta 2\pi H_1^{(2)}(k\rho)\left[\hat{x}\frac{y-y'}{\rho} \quad -\hat{y}\frac{x-\hat{x}}{\rho}\right]. \tag{3.22}$$

The region of the cylinder that is nearer to the line sources (φ = 180°) is expected to have more error than the regions far away, since the current is more rapidly varying there. This is also observed, for example, in antennas near their feed region (and often motivates a higher MoM discretization density in that region).

Figure 3.1(b) shows the performance of the three residual-based error estimators for cylinder of Figure 3.1(a) modeled with 200 cells. The reference solution in this case is the result obtained with 400 cells, and all three estimators predict a similar error pattern as the reference. All the estimators correctly identify the highest error region near φ = 180°.

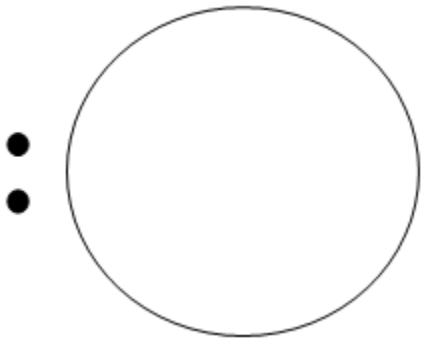

Fig. 3.1(a): Geometry of the problem.

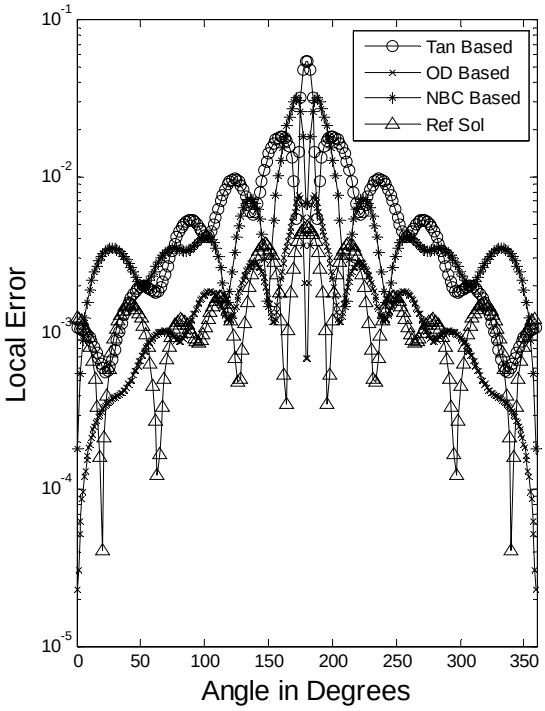

Fig. 3.1(b): Local error for problem of Figure 3.1(a).

Figure 3.1(c) shows a plot of the global error produced by the same estimators, as a function of the number of unknowns or cells used in the computations. The global residual error estimates decrease at approximately an O(h) rate as the cylinder model is refined. As discussed below, this is different from the rate at which the reference current density error decreases. These rates agree with those observed in [22–23] for the TE EFIE and linear basis functions.

Figure 3.2(a) shows a keyhole-shaped cylinder, consisting of sections of two circular cylinders connected by a region with parallel walls. Figure 3.2(b) compares the performance of the three residual-based error estimators for a keyhole-shaped cylinder of 4.15λ total perimeter, modeled with 300 cells, for the same double line source excitation used in Figure 3.1(a). The larger end of the target has a radius of 0.32λ, while the smaller end has a radius of 0.14λ. The circular segments have centers separated by 1.32λ. The reference solution is obtained using 600 cells. There is a relatively large error level near the junction where the large circle meets the planar region (at 90° and 270°), and a larger error where the smaller circle meets the planar region (near 10° and 350°). The expected higher-error region at φ = 180° is correctly identified by the three estimators. Figure 3.2(c) shows a plot of the global error, as the number of unknowns used in the computations is varied. The global residual error levels decrease at approximately an O(*h*) rate as the cylinder model is refined.

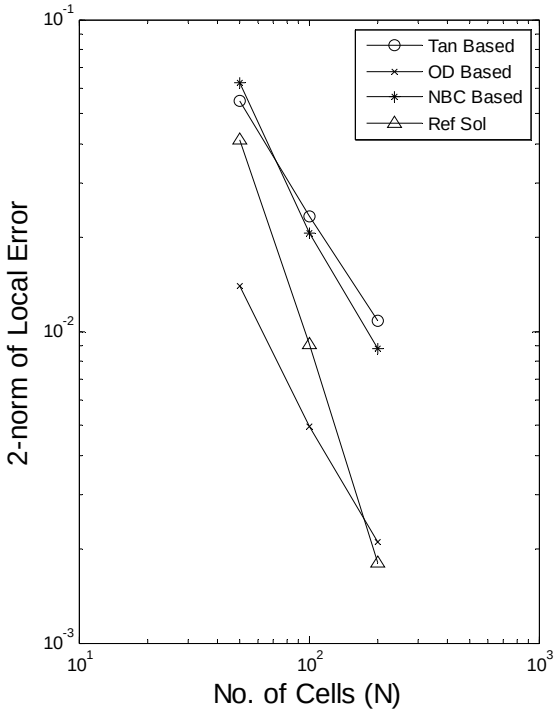

Fig. 3.1(c): Global error for problem of Figure 3.1(a).

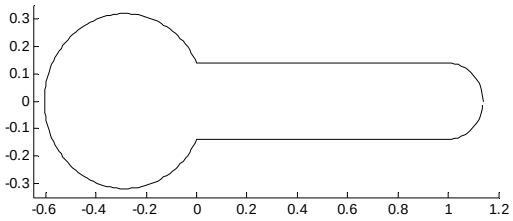

Fig. 3.2(a): Geometry of the problem.

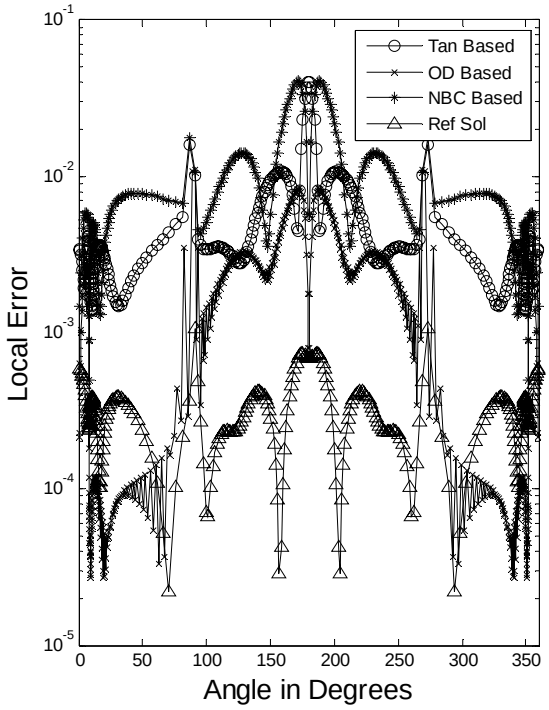

Fig. 3.2(b): Local error for problem of Figure 3.2(a).

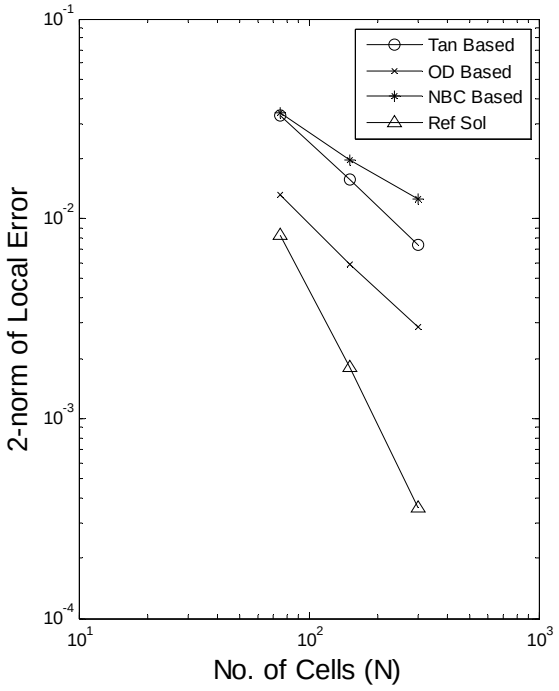

Fig. 3.2(c): Global error for problem of Figure 3.2(a).

Figure 3.3 shows the local error computed by the three estimators for the same keyhole-shaped cylinder as shown previously in Figure 3.2(a), but with a uniform plane wave excitation instead of line sources. The plane wave impinges symmetrically upon the larger end of the scatterer. It is expected that the error will be relatively uniform except near discontinuities in the surface, as is confirmed by Figure 3.3. Error peaks near 10° and 90° angles correspond to curvature discontinuities where the circular regions meet the planar region of the surface. The higher spike corresponds to the sharper corner. Another interesting observation is that the error level gradually rolls off with increasing distance from the corner cells. The global error behavior is similar to that shown in Figure 3.2(c) and is not repeated here.

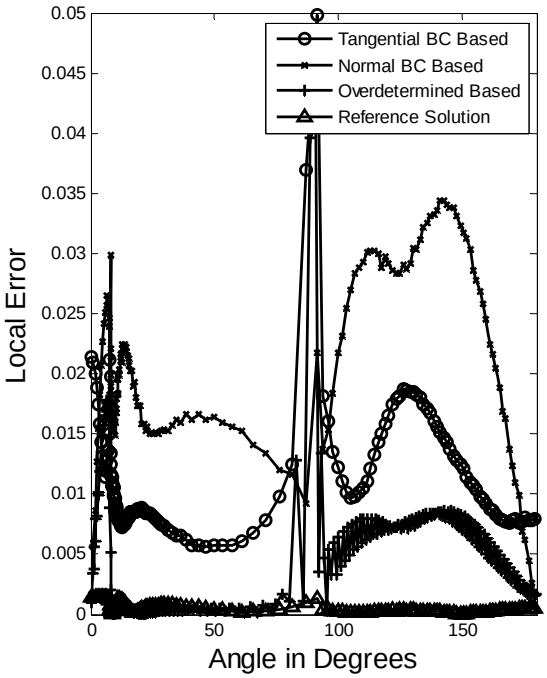

Fig. 3.3: Local error for the problem of Figure 3.2(a) for place wave illumination.

Figure 3.4(a) shows the performance of the three residual-based error estimators on a problem involving a circular cylinder of 1λ circumference, where λ is the wavelength, modeled with 40 cells. The reference solution in this case is the exact series solution, which indicates that all three estimators predict a larger error level than the actual level. Figure 3.4(b) shows a plot of the global error in the same solution, as a function of the number of unknowns used in the computations. Although the global error levels are higher than the actual, they decrease at approximately the same rate of O(h) as the cylinder model is refined. This rate agrees with that observed in [22–23] for the residual errors associated with the TE EFIE and linear basis functions.

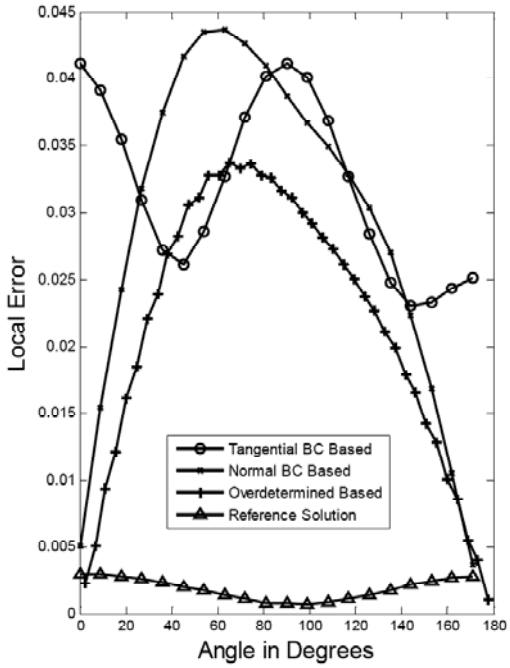

Fig. 3.4(a): Local error estimates produced by the three error estimators and the actual current density error as determined from the exact solution, for a circular cylinder of circumference 1λ.

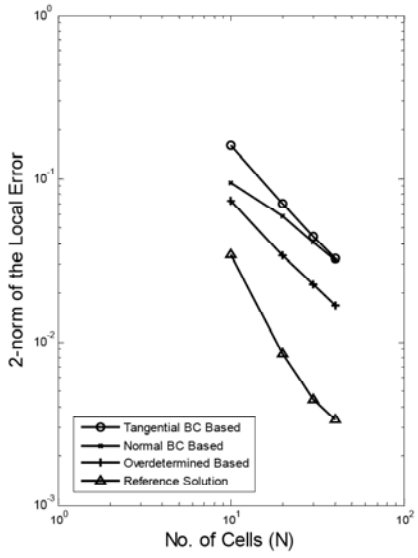

Fig. 3.4(b): Global error estimates produced by the three error estimators and the actual error, for a circular cylinder of circumference 1λ.

Figure 3.5(a) shows the performance of the three residual-based error estimators on a problem involving a triangular cylinder (equilateral) of 1λ circumference, modeled with 48 cells. The incident plane wave impinges symmetrically upon one corner of the triangle. The reference solution is a numerical result obtained using 300 cells. For the TE polarization, the exact electric field at sharp corners is usually infinite, due to the behavior of the electric charge in the vicinity of the corners. Since the expansion functions used within the EFIE discretization do not provide the proper edge singularity for these problems, the fields near the edges are incorrect, and the local error levels exhibit large spikes in those locations. Figure 3.5(b) shows a plot of the global error in the same solution, as the number of unknowns used in the computations is varied. These error estimates are decreasing very slowly, as a consequence of the edge singularities.

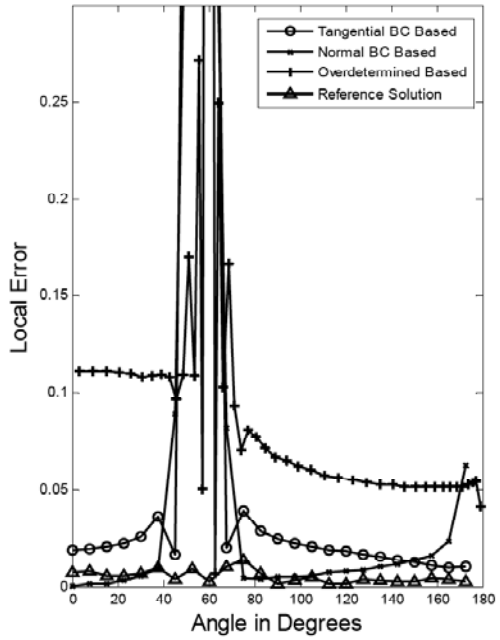

Fig. 3.5(a): Local error estimates produced by the three error estimators and the error in the current density as determined from a reference solution, for an equilateral triangular cylinder of perimeter 1λ.

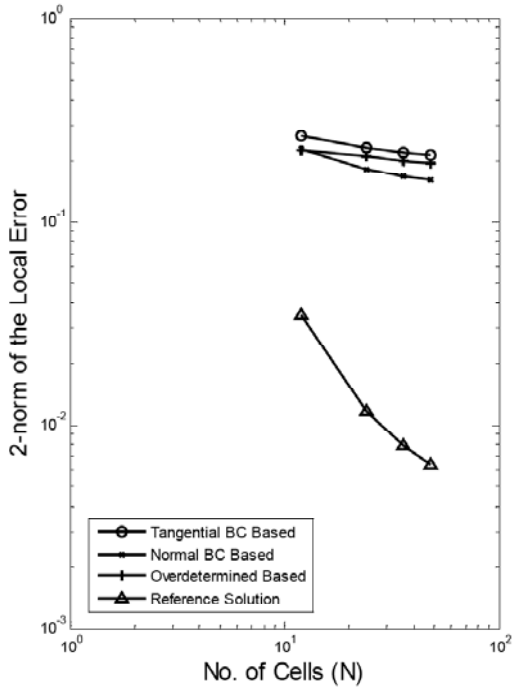

Fig. 3.5(b): Global error estimates produced by the three error estimators and the reference error, for a triangular cylinder of perimeter 1λ.

The three residual-based error estimators were also studied for a problem involving a square cylinder of 1λ circumference, modeled with 48 cells. As observed for the triangular cylinder, the local estimators all indicate large error levels near the corners, where the linear basis functions do not properly model the charge singularities. The global residual error levels are similar overall to those obtained for the triangular cylinder: they are higher than the actual current error, and decrease at a slow rate as the cylinder model is refined due to the edge singularities.

3.6 Comment on the global error rates

In practice, the error in moment method results is usually dominated by the ability of the basis functions to represent the actual current density. For a piecewise-linear representation of a

smoother function, this error should decrease at an O(h^2) rate, where h is the nominal mesh size [4]. The reference solution error plotted in Figures 3.1(c) and 3.2(c) appears to decrease at approximately that rate. It has been observed in [22-23], and in Figures 3.1(c) and 3.2(c), that for the TE EFIE operator, the residual error decreases at a rate that is one order less, an O(h) rate. This is apparently due to the nature of the TE EFIE operator, which contains one integral and two derivatives. We note that for the transverse-magnetic (TM) polarization, where the operator involves one integration and no derivatives, the EFIE residual error appears to decrease at a rate that is one degree faster than the current error. In other words, it appears that each integral increases the rate by one order while each derivative decreases the rate by one order, relative to that of the current density. It has been observed that the residual error associated with the magnetic field integral equation (MFIE) decreases at the same rate as the current density error [22-23], while error in far field quantities may decrease at different rates from the current density for all these integral operators [22].

The different error rates may limit our ability to use residual error estimators to determine the absolute global level of current density error in a particular result. This issue will be considered in a later chapter. Despite this limitation, the residual estimators appear to correctly identify regions of relatively large errors, and therefore are able to provide a local error distribution suitable for an adaptive refinement algorithm.

3.7 Computational cost of estimators

The relative computational cost of the estimators can be estimated as follows. The baseline cost without error estimation is:

$$C_0 \cong \alpha N^2 + \beta N^3 , \tag{3.22}$$

where α and β are the constants associated with matrix fill and solve times, respectively. The

tangential and normal estimators add an approximate cost of:

$$C_t \cong C_n \cong \alpha N^2 , \tag{3.23}$$

since the residual computation in each case is comparable to an additional matrix fill.

The overdetermined error estimator has an approximate cost of:

$$C_{over} \cong 2\alpha N^2 + 5\beta N^3 , \tag{3.24}$$

since the matrix has twice as many entries, and since the least-square solution of a 2:1 rectangular system is reported to require about 5 times the operations of the LU factorization of a square system [24].

Thus, all three estimators add a cost of αN^2 operations, but the overdetermined estimator requires an additional $4\beta N^3$ operations beyond that. Thus, the overdetermined estimator is more expensive than the others, especially for large N.

3.8 Adaptive *h*-refinement

In this section, we demonstrate the utility of the above error estimators to carry out adaptive refinement. The type of adaptive refinement we present here is called *h*-refinement and it requires the cell size to be adaptively adjusted to control the error. We use the tangential residual estimator presented in section 3.2 to estimate the local error. The details of our *h*-refinement scheme are as follows. First, an initial coarse solution for the current density J is computed. That solution is used to compute the local error using the tangential residual error estimator. Once the local error values have been computed, they are sorted in descending order to identify the cells with the largest error levels. The 20% of those cells with the largest error are each divided into 3 cells, while each of the next 20% are divided into two cells. The remaining cells are left at their original size. After re-meshing, the problem is solved again to obtain a new

solution for *J*, and a new local error estimate is obtained from the residual error. If the local error is still high or does not meet the user's criteria, the above procedure may be repeated recursively.

We implemented one iteration of the above procedure for a 5λ circumference cylinder illuminated with a pair of line sources as shown in Figure 3.1(a). The initial coarse solution was calculated for 100 cells and local error was computed. Based on the estimated local error values, a new mesh was created according to above scheme and is shown in Figure 3.6.

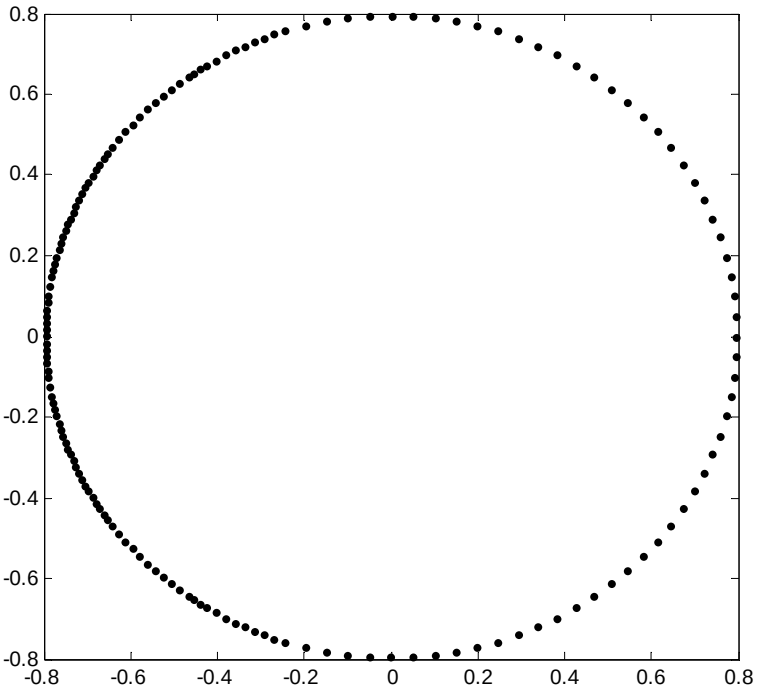

Fig. 3.6: Mesh density after the refinement.

It is clear that the mesh density in the anticipated high-error region (near φ = 180°) has increased. The local error estimate computed before and after the adaptive refinement step is shown in Figure 3.7, and it is clear that the tangential residual error has been reduced in the refined region of the problem.

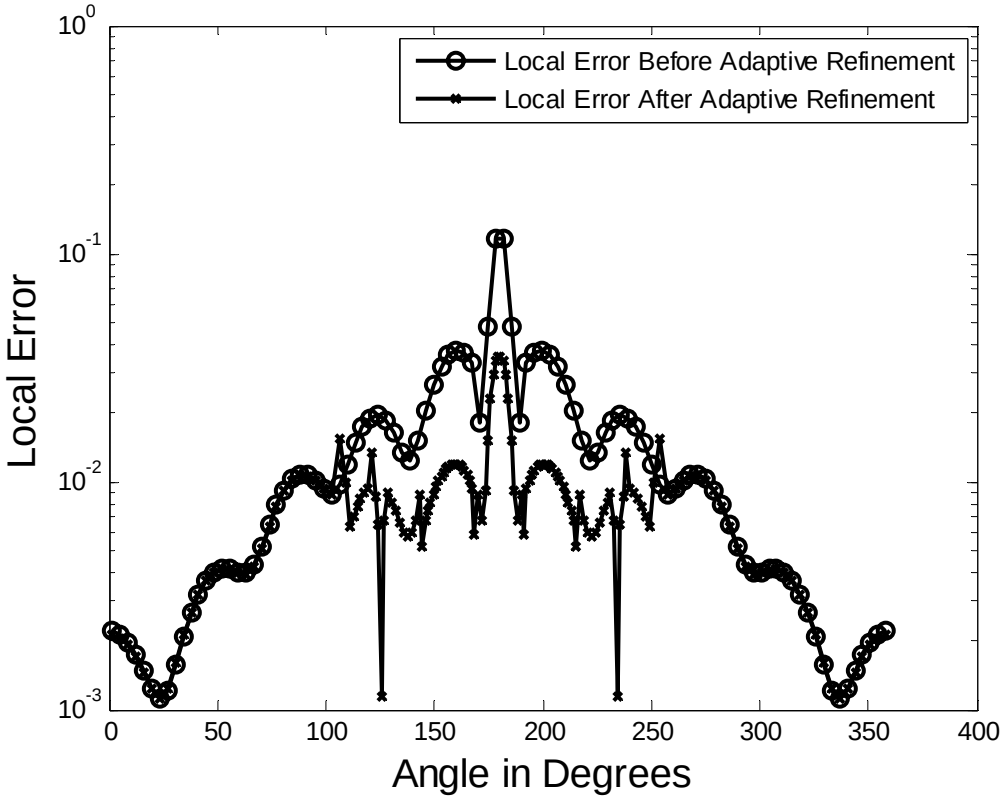

Fig. 3.7: Local error estimate before and after *h*-refinement.

Figure 3.8 shows the actual error in J, both before and after the adaptive refinement step, using (3.21) with a 600-cell solution for J as a reference. It is clear from Figure 3.8 that the error in J is reduced by a factor of more than 3 in the refined regions. Thus, the combination of the tangential residual estimator and the *h*-refinement procedure shows promise for realizing a more uniform error level across the problem domain.

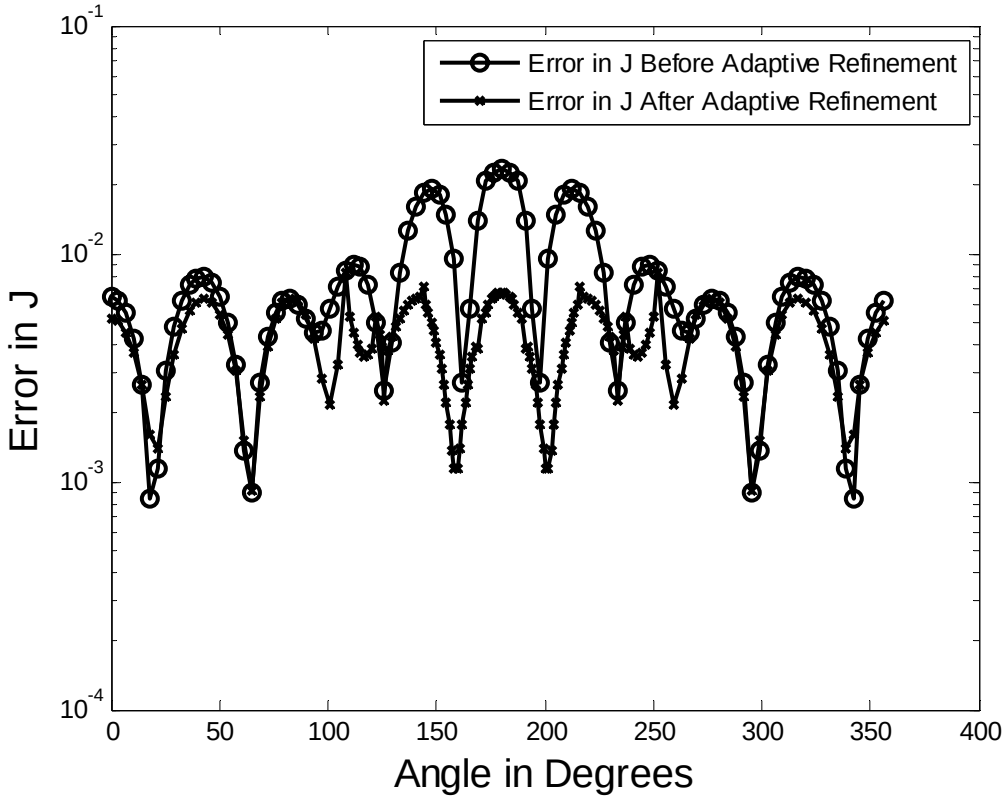

Fig. 3.8: Error in J before and after h-refinement.

3.9 Concluding remarks

This chapter considered an initial investigation of three residual-based error estimators in conjunction with an MoM solution of electromagnetic integral equations. The MoM formulation was limited to the use of piecewise linear basis functions defined on a flat-faceted model of the targets. A rudimentary h-refinement implementation was included for illustration. All three estimators successfully located higher-error regions in test problems. All appear to be suitable for use in adaptive refinement schemes. The tangential residual and the normal residual estimators have comparable cost and generally gave comparable results. The overdetermined estimator also gave similar results, but requires additional computation compared to the others.

While the tangential error estimators considered in this chapter were successful at identifying the regions of a structure with the largest error, they were not as accurate at predicting the overall global error levels. In fact, it was noted that for the EFIE the residual error decreases at a different rate than the current density error as a function of the nominal cell size. At the present time, this limits the use of simple residual error estimators for predicting the absolute error associated with a particular result. We will revisit this issue in subsequent chapters.

The discussion in Chapter 2 concluded that the LCN procedure was more efficient for implementing *p*-refinement than the MoM approach, since MoM matrix entries involve inner product integrations that require more computation as the degree of the basis functions increases. Thus, in Chapter 4, we turn to the LCN approach for a more detailed investigation of error estimators and adaptive refinement techniques.

CHAPTER 4

ERROR ESTIMATION TECHNIQUES AND ADAPTIVE REFINEMENT FOR THE LOCALLY-CORRECTED NYSTRÖM METHOD

Chapter 3 conducted a preliminary investigation of error estimators in the context of the MoM. It was concluded that residual-based error estimators appeared to correctly identify the regions of the problem domain where error levels were greater than average. In order to study the performance of error estimators in more detail, it is desired to develop numerical solutions of the EFIE that are more accurate than the simple approach used in Chapter 3. Specifically, we would like to incorporate higher-order representations for the current, with curved-cell models of the targets under consideration. Since it appears that LCN formulations are more efficient for high order representations, in this chapter we turn our attention to an LCN discretization of the EFIE for the TE-to-z polarization.

This chapter presents several local (cell-by-cell) error estimation techniques suitable for use with the LCN approach. The accuracy and ease of implementation of the error estimators are evaluated for various problems with regions of high local error. The error estimation schemes are shown to correctly identify the high-error regions. Subsequently, a simple adaptive *p*-refinement algorithm is implemented for solving the TE EFIE. The *p*-refinement implementation is successful at reducing the error values in the high-error cells and leads to a more uniform error distribution for most of the examples.

This chapter is organized as follows. Section 4.1 discusses the LCN method and how it differs from that of the MoM. Section 4.2 reviews important implementation details of the LCN approach for the TE EFIE. Several error estimation techniques compatible with the LCN are developed in Section 4.3. Section 4.4 presents the simulation results of these error estimators for

a set of selected test problems. Section 4.5 discusses the adaptive refinement technique and its application to various problems using the error estimators developed in Section 4.3. Finally, Section 4.6 provides conclusions.

4.1 Introduction

The Nyström method is an alternative to the method of moments (MoM) for numerical solutions of integral equations. In the Nyström approach, integrals are replaced with quadrature summations. As described in Chapter 2, the locally-corrected Nyström (LCN) method is a variation on the classical Nyström method that enables its use for problems with singular (infinite) integrands [5, 30]. Because the Nyström method does not involve inner products, it is expected to be far more efficient than the MoM as the degree of representation is increased. This makes it advantageous for situations where high accuracy modeling is desired.

Since the exact solutions of the continuous integral equations of electromagnetics reside in an infinite dimensional space, procedures such as the MoM and the LCN incur error due to their finite dimensional representations of the unknown. The dominant error in a numerical solution procedure of this type is usually the discretization error associated with the approximate representation of the current density. In the LCN approach, this error arises from the fact that the current density is represented by samples (at nodes of the quadrature rule on which the discretization is based). Although a q-point Gauss-Legendre quadrature rule is capable of exactly integrating polynomials of degree $2q-1$, in the LCN approach the local correction process limits the accuracy to that of the basis functions used in the local correction process, which is at most degree $q-1$ [5]. This error can be improved by refining the mesh, and reducing the cell dimensions, or by refining the representation, and using more quadrature points per cell (and equivalently improving the accuracy of the representation for the current). The goal of an

adaptive refinement algorithm is to identify the regions of the problem where the error is large so that mesh refinement (*h*-refinement) or representation refinement (*p*-refinement) can be carried out automatically.

4.2 The LCN solution of the TE EFIE

The TE EFIE was previously introduced in Chapter 3. Here, the equation will be written in a different form, which can be expressed as [5]:

$$E_t^{inc}(t) = j\frac{\eta}{k}\int_{\Gamma} J_t(t)D(t,t')dt', \tag{4.1}$$

where

$$D(t,t') = \{k^2\cos[\Omega(t)-\Omega(t')] + \sin\Omega(t)\sin\Omega(t')\frac{\partial^2}{\partial x^2} - \sin[\Omega(t)+\Omega(t')]\frac{\partial^2}{\partial x\partial y} + \cos\Omega(t)\cos\Omega(t')\frac{\partial^2}{\partial y^2}\}\frac{1}{4j}H_0^{(2)}(kR) \tag{4.2}$$

is the kernel of the equation, Ω is the angle of the outward normal to the scatterer surface, and $H_0^{(2)}$ is the Hankel function of 0-th order and 2-nd kind. The kernel *D* becomes infinite when the observer at *t* approaches the source at *t′*, and motivates the use of a local correction procedure to construct a bounded kernel *L*. The bounded kernel *L* is obtained at the required observer locations in the near-field region by matching the actual fields produced by a set of known sources, Legendre polynomials in our case, to the fields produced by applying the quadrature rule to the product of these sources and *L*. Details on this procedure were provided in Chapter 2 and additional information can be found in [5].

For geometrical modeling of the scatterer, we have used curved cells with quadratic curvature defined by the quadratic Lagrangian functions defined over the interval $-1 \le t \le 1$ [4].

All cells will be scaled to this standard interval size and a suitable Jacobian function is used to scale various derivatives and integrals. Suppose t is the parametric variable defined on interval $-1 \le t \le 1$ used to describe a single cell. The cell is defined using three points (x_1, y_1), (x_2, y_2), and (x_3, y_3), and the mapping

$$x(t) = x_1 B_1(t) + x_2 B_2(t) + x_3 B_3(t), \tag{4.3}$$

$$y(t) = y_1 B_1(t) + y_2 B_2(t) + y_3 B_3(t). \tag{4.4}$$

In these equations,

$$B_1(t) = \frac{1}{2} t(t-1), \tag{4.5}$$

$$B_2(t) = 1 - t^2, \tag{4.6}$$

$$B_3(t) = \frac{1}{2} t(t+1), \tag{4.7}$$

are quadratic Lagrangian functions. Integrals defined over the domain of curved cells in the t-space ($-1 \le t \le 1$) are transformed with the use of the Jacobian function

$$Q(t) = \sqrt{\left(\frac{dx}{dt}\right)^2 + \left(\frac{dy}{dt}\right)^2}, \tag{4.8}$$

to correspond to the actual physical interval of the cell. In other words, the integrals are carried out by quadrature in the t-space, and the presence of the Jacobian in the integrand scales the result as if the integrals were in the x-y space.

The discretization of the EFIE in Equation (4.1) is based on a subdivision of the contour of the structure under consideration into N cells. For illustration purposes, suppose a q-point Gauss-Legendre rule is used in each of the N cells to define the Nyström process. This yields a linear system of order Nq given by

$$\mathbf{ZJ} = \mathbf{E}^i, \tag{4.9}$$

where the entries of **J** are the unknowns, $J_t(t_{ni})$, and the vector $\mathbf{E}^i$ consists of the tangential components of the incident field sampled at the observation points. The entries of the impedance matrix **Z** are directly sampled from *D* if observer and the source are far enough apart (more than 0.2λ, in our case) in accordance with the classical Nyström approach. For closely-spaced observer and source locations, the **Z** matrix entries are computed by sampling the bounded kernel *L* constructed by the local correction process (Chapter 2). To compute *L* within one cell, it is necessary to solve a *q* by *q* system of equations — Equation (2.12) from Chapter 2 — *q* times.

To validate the accuracy of the LCN computer program, we tested it for a problem involving a circular cylinder of 1λ circumference illuminated with a uniform plane wave. The exact J_t for this problem is available in the form of an eigenfunction series expansion [31]. The normalized local error as a function of the cell index *i* and the global error, defined as 2-norm of the local error, were computed using

$$LE_i = \frac{\left|J_{num} - J_{exact}\right|}{\left|J_{exact}\right|_{\max}}, \tag{4.10}$$

$$\left\|LE\right\|_2 = \sqrt{\frac{1}{N}\sum_{i=1}^{N}\left(LE_i\right)^2}\,, \tag{4.11}$$

and are plotted in Figure 4.1. The error levels reduce as the mesh is refined, indicating that the numerical solutions are converging to the exact solution. Three quadrature nodes per cell ($q = 3$) were used. As the cells in the model are reduced in size, the global error in the current density appears to decrease at a rate of $O(h^q)$, which is as expected.

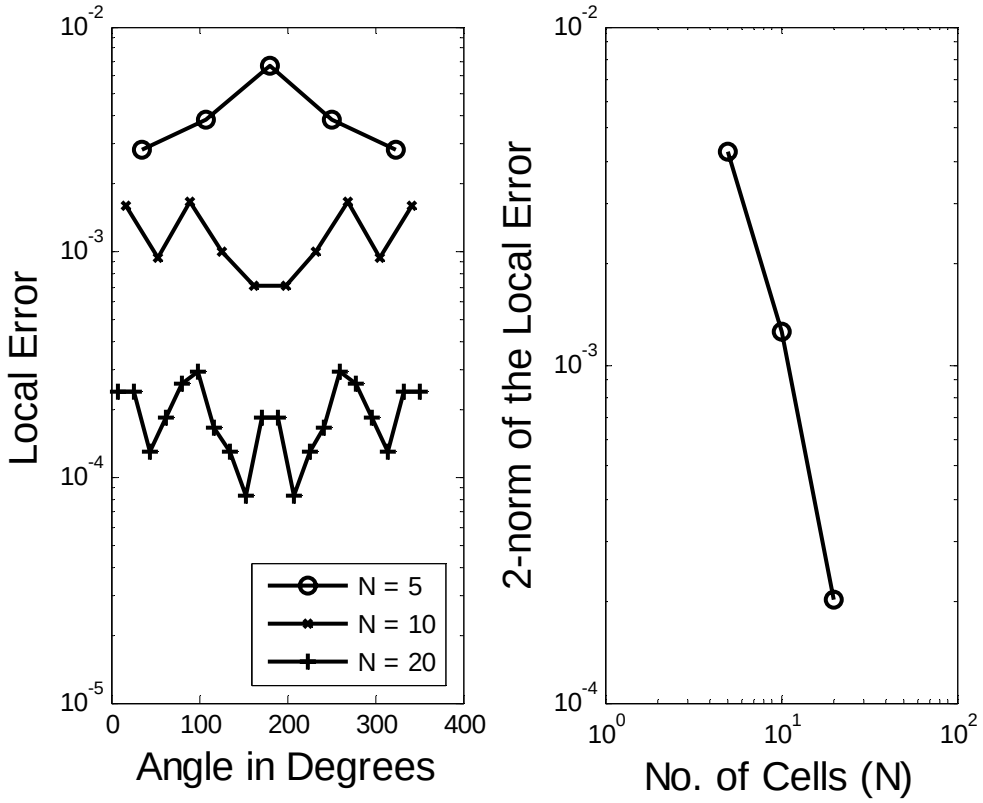

Fig. 4.1: Local and global errors for 1λ circumference cylinder.

4.3 Error estimation techniques for the LCN

In this section, we present several different techniques for estimating the numerical error in the LCN solution of the TE EFIE. All the error estimators presented below are general and can be applied to other electromagnetic integral equations.

A. Derivative Discontinuity in J

For a smooth scatterer, we expect the current to be smooth with no jump discontinuities at the cell junctions. However, since the representation employed by the LCN approach does permit the current density to jump at cell boundaries, it will not be exactly continuous there. The resulting discontinuities are attributed to the numerical error, and should be proportional to that

error. Thus, they can be used to create an error estimate. Our initial investigation considered an error estimator based directly on the jump discontinuity of J, but that estimator did not perform as well as the residual error estimators. Therefore, we instead considered an estimator based on the discontinuity in the first derivative of J at cell boundaries.

At a cell edge, we calculate the left- and right-hand derivatives of J_t to find the normalized change in J_t', given by

$$LE_i^{Diff} = \frac{|J_t'(t_{bi}^+) - J_t'(t_{bi}^-)|}{\max(|J_t|)}. \tag{4.12}$$

where the cell boundary is denoted by the location $\{t_{bi}\}$. Equation (4.12) can be used as a local error estimator. A global error estimator can be obtained by taking the 2-norm of (4.12) in the same manner as in Equation (4.11).

Figure 4.2 shows the local error computed using Equation (4.12) for a circular cylinder of 1λ circumference for two mesh densities, and compares those results with the actual error in current density computed using Equation (4.10). There is a good correlation between the two error functions, other than a difference of scale of approximately one order of magnitude. This suggests that the derivative discontinuity estimator holds promise, if we can correctly select the scale factor.

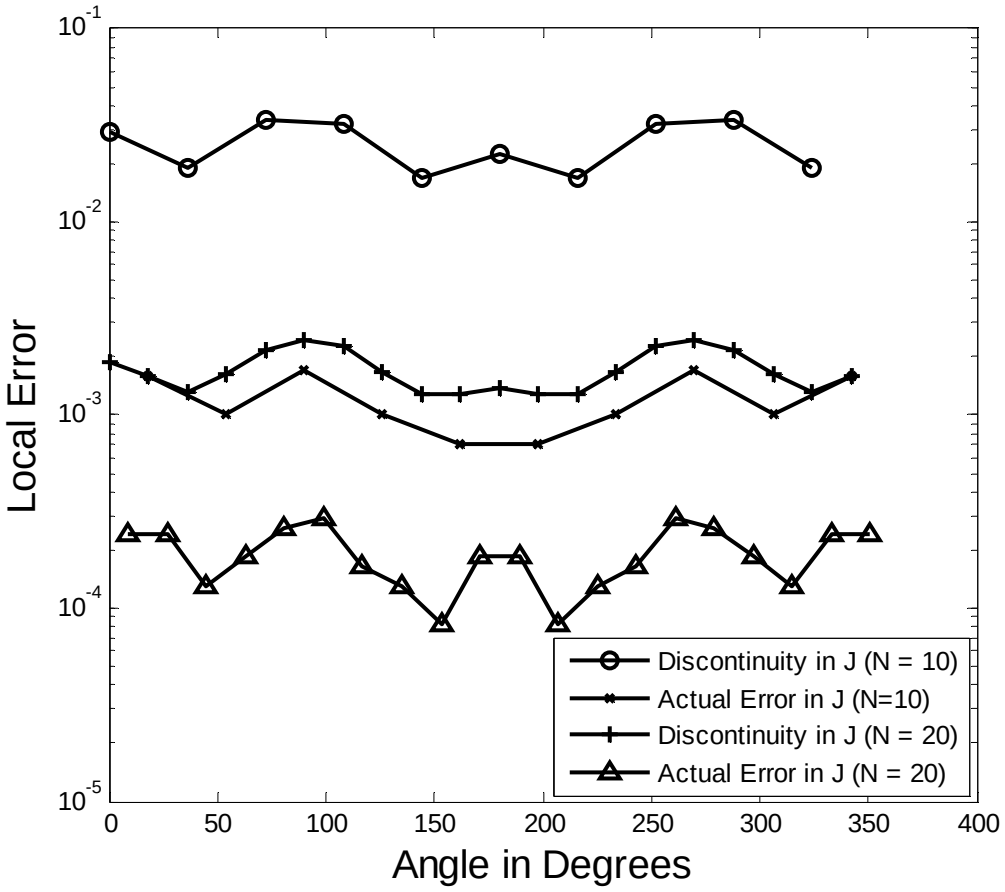

Fig. 4.2: Error estimates based on the derivative discontinuity in *J*, compared with the actual error.

B. Tangential E-Field Residual

The tangential E-field boundary condition for conducting targets dictates that the tangential component of the total E-field must vanish at each point along the contour of the scatterer, i.e.,

$$E_{\tan}^{tot} = 0\,, \tag{4.13}$$

where the total electric field is obtained from the EFIE as

$$E_{\tan}^{tot} = E_{\tan}^{inc} - j\frac{\eta}{k}\int_{\Gamma} J_t(t)D(t,t')dt'\,. \tag{4.14}$$

Thus, the solution of the EFIE is attempting to satisfy the boundary condition in Equation (4.13), or equivalently the condition that the residual of the equation vanish. The tangential residual is defined as

$$R_{\tan}(t) = \left| E_t^{inc}(t) - j\frac{\eta}{k}\int_{\Gamma} J_t(t) D(t,t')dt' \right|. \tag{4.15}$$

Since the numerical solution produced by the LCN procedure will satisfy Equation (4.13) exactly at the set of node points $\{t_{ni}\}$ associated with the LCN quadrature rule, the residual $R_{\tan}(t)$ will be exactly zero if evaluated on that same set. Thus, that residual will give no information about the error. But, if the residual is evaluated at other points chosen from $\Gamma - \{t_{ni}\}$ (Γ is the problem domain), it will generally be nonzero and provide some indication of the error in the numerical result. Consequently, we consider a local error estimator based on the normalized value of the residual:

$$LE_i^{\tan} = \frac{\left|R_{\tan}(t_i)\right|}{\left|E_t^{inc}\right|_{\max}}, \tag{4.16}$$

where the set of points $\{t_i\}$ must differ from the nodes of the quadrature rule. A global error estimator can also be defined by taking the 2-norm of (4.16) in the same manner as in Equation (4.11).

C. Normal E-Field Residual

The normal component of the electric field at a conducting surface must also satisfy a boundary condition, given by

$$\hat{n} \bullet \overline{E^{tot}} = \frac{\rho_s}{\varepsilon} = \frac{j\eta}{k} \cdot \frac{dJ_t}{dt}, \tag{4.17}$$

where ρ_s is the surface charge density, and the outward normal vector $\hat{n}$ can be expressed as

$$\hat{n}(t) = \hat{x}\cos\Omega(t) + \hat{y}\sin\Omega(t), \tag{4.18}$$

where Ω is the angle of the outward normal to the surface. The surface charge density is related to the derivative of the current by the equation of continuity. The total electric field can be written as

$$\bar{E}^{tot} = \bar{E}^{inc} - \bar{E}^{s}. \tag{4.19}$$

A procedure for calculating the normal component of the scattered field, $\hat{n} \bullet \overline{E^s}$, from a given numerical solution for J_t is described in Appendix A. Using that procedure, the residual in the normal component of the electric field can be defined as

$$R_{nor}(t) = \left| \hat{n} \bullet \overline{E^{inc}}(t) + \hat{n} \bullet \overline{E^s} - \frac{j\eta}{k} \cdot \frac{dJ_t}{dt} \right|. \tag{4.20}$$

A local error estimator based on the normal E-field residual can be defined as

$$LE_i^{nor} = \frac{\left| R_{nor}(t_i) \right|}{\left| E_n^{inc} \right|_{\max}}. \tag{4.21}$$

A global estimator can be obtained following the construction of Equation (4.11).

D. Recomputation of J using the Magnetic Field

In the last two sub-sections, we have defined residual-based error estimators for the TE EFIE that use the TE EFIE kernel itself (in a separate calculation from the one used to determine the initial solution) to calculate the residual. This approach is computationally expensive due to the hypersingular nature of the TE EFIE kernel, and the need to employ local corrections for near-field calculations. We may be able to improve the speed of the error estimation process if we can avoid using the EFIE kernel to compute the residual. An alternate approach is to employ a different equation, the magnetic field integral equation (MFIE), in this process. One possibility is to compute the tangential or normal residual using the MFIE. Another possibility is to re-

compute the current density using the MFIE operator, in order to compare to the original current density. We consider the second approach in the following.

The MFIE is based on the tangential H-field boundary condition

$$\hat{n} \times \overline{H^{tot}} = \overline{J}, \tag{4.22}$$

which, for TE polarization, can be expressed in terms of scalar components as

$$H_z^{inc} + H_z^s = -J_t^{MFIE}. \tag{4.23}$$

Suppose we have obtained a numerical solution for J_t by solving the EFIE, which we denote J_t^{EFIE}. That result may be substituted into the MFIE operator, and used to compute the scattered magnetic field

$$H_z^s = -\frac{J_t^{EFIE}}{2} + \int J_t^{EFIE}(t') C_2(t,t') dt', \tag{4.24}$$

where $C_2(t,t')$ is given by:

$$C_2(t,t') = \left\{ \begin{array}{l} \dfrac{\kappa(t)}{4\pi} \quad \lim t' \to t \\ \dfrac{jk}{4} H_1^{(2)}(kR) \left\{ \dfrac{\left[y(t) - y(t')\right]}{R} \sin\Omega(t') + \dfrac{\left[x(t) - x(t')\right]}{R} \cos\Omega(t') \right\} \\ otherwise \end{array} \right\}. \tag{4.25}$$

To compute the integration required in Equation (4.24), we can employ a suitable quadrature rule, and use an approach similar to that of the LCN procedure. The computation can be expressed as a matrix-vector multiplication of the form

$$\mathbf{H^s = ZJ}, \tag{4.26}$$

where entries of the **Z** matrix are given by

$$Z_{mj,mj} = -\frac{1}{2} + w_j Q_{mj} \frac{\kappa(t)}{4\pi}, \tag{4.27}$$

$$Z_{mj,mi} = -\frac{jk}{4} w_i Q_{mi} \left[\sin\Omega_m \frac{y_{mj} - y_{mi}}{R_{mj,mi}} + \cos\Omega_m \frac{x_{mj} - x_{mi}}{R_{mj,mi}} \right] H_1^{(2)}(kR_{mj,mi}), \quad i \neq j \,, \tag{4.28}$$

$$Z_{mj,ni} = -\frac{jk}{4} w_i Q_{ni} \left[\sin\Omega_n \frac{y_{mj} - y_{ni}}{R_{mj,ni}} + \cos\Omega_n \frac{x_{mj} - x_{ni}}{R_{mj,ni}} \right] H_1^{(2)}(kR_{mj,ni}), \quad m \neq n \,. \tag{4.29}$$

Once we obtain the scattered H_z-field from J_t^{EFIE}, it can be substituted into Equation (4.23) to find J_t^{MFIE}. Since the exact solution for J_t would satisfy both equations, any discrepancy between the two current densities is attributed to the numerical error. Thus, a local error estimate can be computed as the normalized difference between the two current densities:

$$LE_i^{MFIE}(t_{ni}) = \frac{\left| J_t^{EFIE}(t_{ni}) - J_t^{MFIE}(t_{ni}) \right|}{\left| J_t^{EFIE}(t) \right|_{\max}} \,. \tag{4.30}$$

A global error estimate can be computed from the 2-norm of (4.30), following Equation (4.11).

This MFIE error estimator may be more efficient to compute than the residual estimators defined previously. However, the MFIE boundary condition in (4.22) and (4.23) has an important limitation: it is only valid for closed scatterers due to the assumption that the magnetic field is zero on one side of the surface. Thus, while Equation (4.24) should produce the correct scattered field, for open surfaces Equation (4.23) will not produce the correct current density. Thus, this estimator will only be useful for problems involving closed scatterers.

E. Use of an over-determined system of equations

The preceding discussion has assumed that the LCN procedure will be implemented with the same number of match points as samples of the current (to produce an *Nq* by *Nq* system). In fact, the LCN method can be implemented with more observer points per cell than the number of source samples in that cell. The resulting over-determined system has more equations than unknowns. For example, if we use twice as many observer points per cell than source points, by

placing observer locations just to the right and left ($t = \pm 0.1$ in our case) of each of the source locations, we can construct a system of order $2Nq \times Nq$ using essentially the same routines used for the previous LCN systems. The solution of the over-determined system

$$\mathbf{Z_{2Nq \times Nq} J_{Nq} = E_{2Nq}} \tag{4.31}$$

can be obtained using a least-square algorithm. The solution of this system may not exactly satisfy any of the individual equations, but it will minimize the overall error in all the equations. Consequently, the solution will produce a nonzero residual of the form [22]:

$$R_{OD}(t_i) = Z_{2Nq \times Nq} J_{Nq} - E^{inc}_{2Nq}. \tag{4.32}$$

This residual can be used to estimate the error. A normalized local error estimator with a form identical to Equation (4.16) can be based on the residual in (4.32). A global error estimate may be obtained by taking the 2-norm of the local error as in Equation (4.11).

4.4 Evaluation of the error estimators

In this section, we consider several examples involving targets with localized regions of relatively high error, in order to evaluate the performance of the error estimators defined previously.

In the first example, a 5λ circumference circular conducting cylinder is illuminated with two line sources placed a radial distance of 0.1λ away from the surface of the cylinder (Figure 4.3). The incident field of these line sources was previously given in Equation (3.22) of Chapter 3. Due to the rapid variation of the currents near the line sources, that region of the cylinder ($\varphi = 180°$) is expected to have more error in the current density than the regions far away.

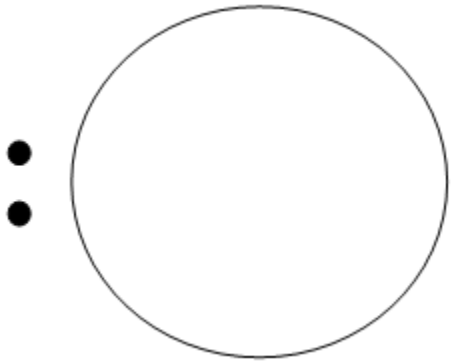

Fig. 4.3: Geometry of the problem.

Figure 4.4 shows a plot of the local error in current density obtained from each of the five error estimation schemes defined in this chapter. All the schemes use a 100-cell model of the scatterer with a uniform order of $q = 4$ (4 node points per cell), and plot the error at the center of each cell. Actually, for tangential and normal residual estimators, error is plotted at the center of each cell whereas, for overdetermined estimator, maximum error per cell is plotted corresponding to the location where maxima occur, and for derivative based estimator, error is plotted at the cell boundaries where it is computed. For MFIE based estimator, error is plotted at the location of the node points. The error obtained from (4.10) using a higher order reference solution is also shown for comparison. The reference solution is obtained using a 400-cell model and order of $q = 4$. All the estimators produce a similar pattern for the error as a function of position, and none underestimate the actual error in the current density. The MFIE based error estimator produces error estimates that are more than one order of magnitude larger than the actual error, while the derivative-based estimator is somewhat larger than the actual error. The residual-based estimators all closely track the actual error. Figure 4.5 shows plots of the global error estimates computed using $q = 4$ for several different mesh densities.

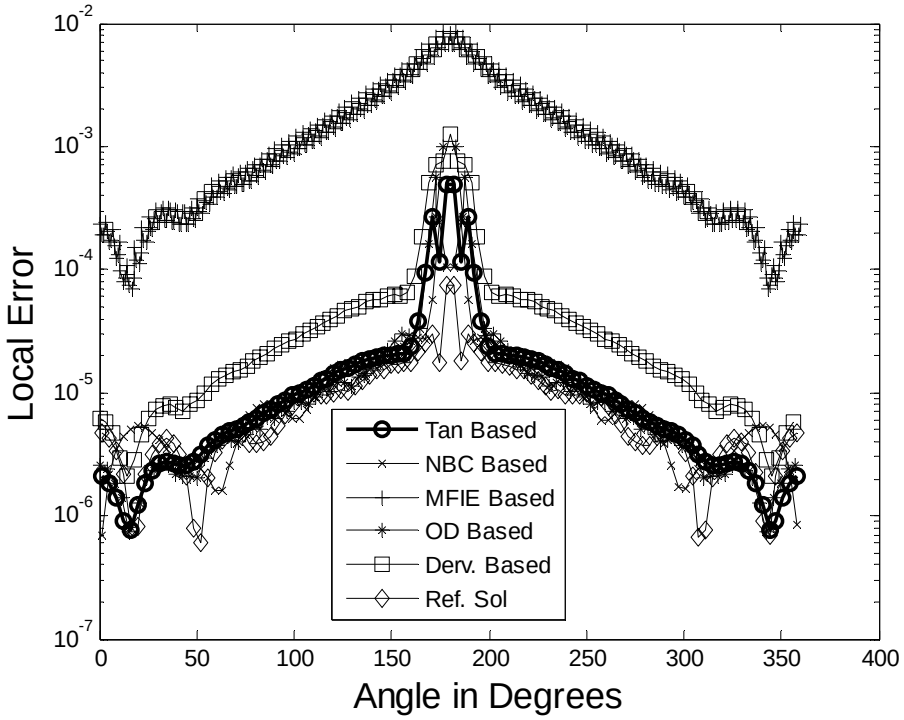

Fig. 4.4: Local error for the problem in Fig. 3 computed using different error estimation schemes.

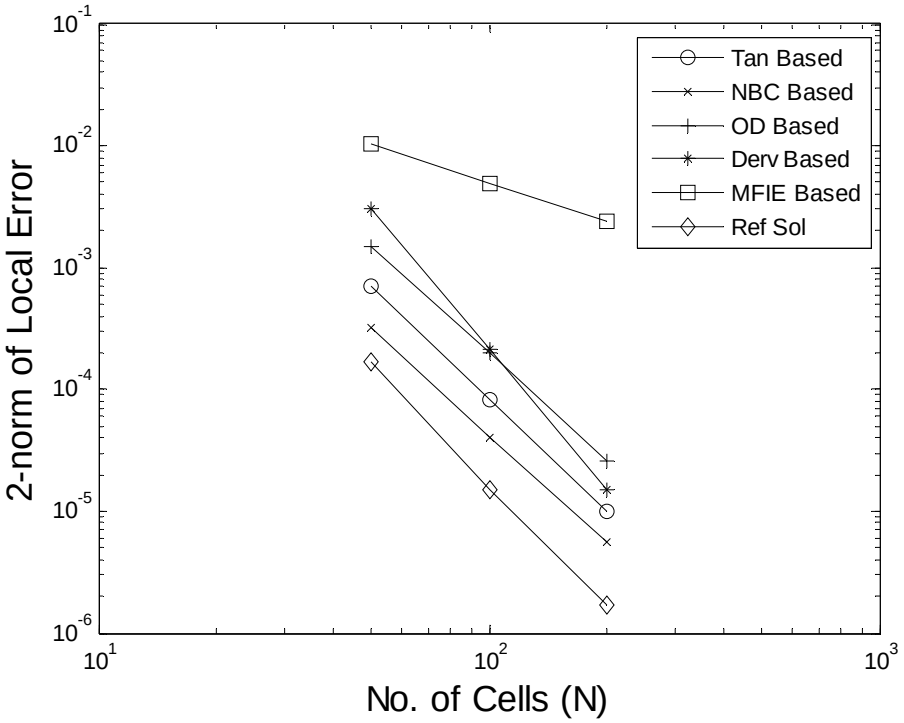

Fig. 4.5: Global error behavior for various error estimators for the problem in Fig. 3.

The second example involves a smooth triangular shaped cylinder (shown in Figure 4.6) illuminated with a pair of line sources similar to those used in Figure 4.3. A model with 80 non-uniform cells was used, as depicted in Figure 4.6. The LCN solutions are obtained with 2 points per cell ($q = 2$), and line sources located at a radial distance of 0.17λ from the surface. Figure 4.7 shows the local error computed using the previous estimators at the same locations as described in the last example. A reference solution was computed using a 160-cell model with $q = 2$. Regions on the surface with sharp curvature are expected to exhibit more error than the smoother regions, as is the region near the line source. The global error, computed as the 2-norm of the local error for varying mesh density, is plotted for each result as shown in Figure 4.8.

For this problem, we also investigate the error behavior as a function of the proximity of the line sources. Figure 4.9 shows the results for the same problem when line sources are moved away to a radial distance of 0.3λ. The peaking in the error is less sharp. Figure 4.10 shows the corresponding global error behavior. Figures 4.11 and 4.12 show the effect of a change in the excitation. Instead of line sources, a plan wave symmetrically impinges upon the scatterer from the –x-axis. With all other solution parameters kept the same, the error becomes more shape and curvature dependant and loses its peaking behavior.

From the last two examples, we can observe two important things; first, the local error computed by our various error estimation schemes follows the same pattern as the reference error computed using an expensive much higher order solution, and second, the global error slopes follow the anticipated [5] convergence rate of $O(h^q)$ as the mesh density is resolved. Moreover, the local error variations as computed by our error estimation schemes follow the geometrical variations of the scatterer i.e. sharper regions have higher error. All this points to a promising use of our error estimation techniques for the adaptive refinement processes.

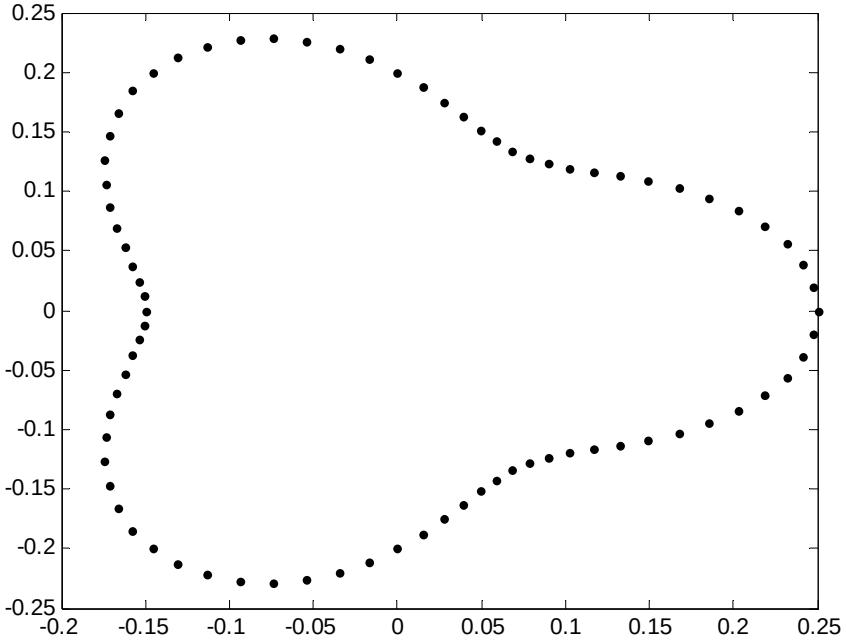

Fig. 4.6: Geometry of the problem.

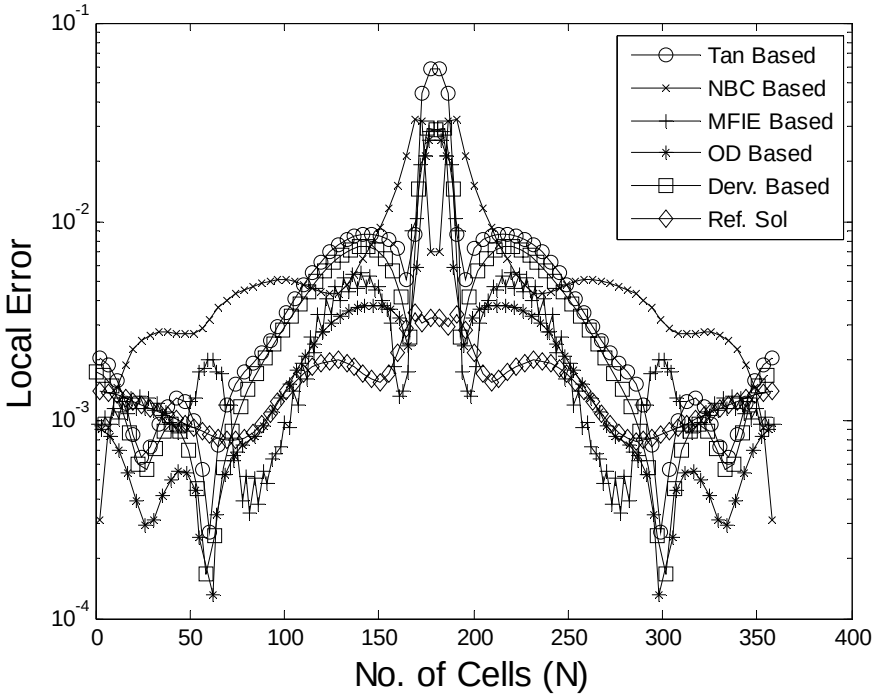

Fig. 4.7: Error for the problem in Fig. 4.6 when illuminated by line sources at a distance of 0.17λ.

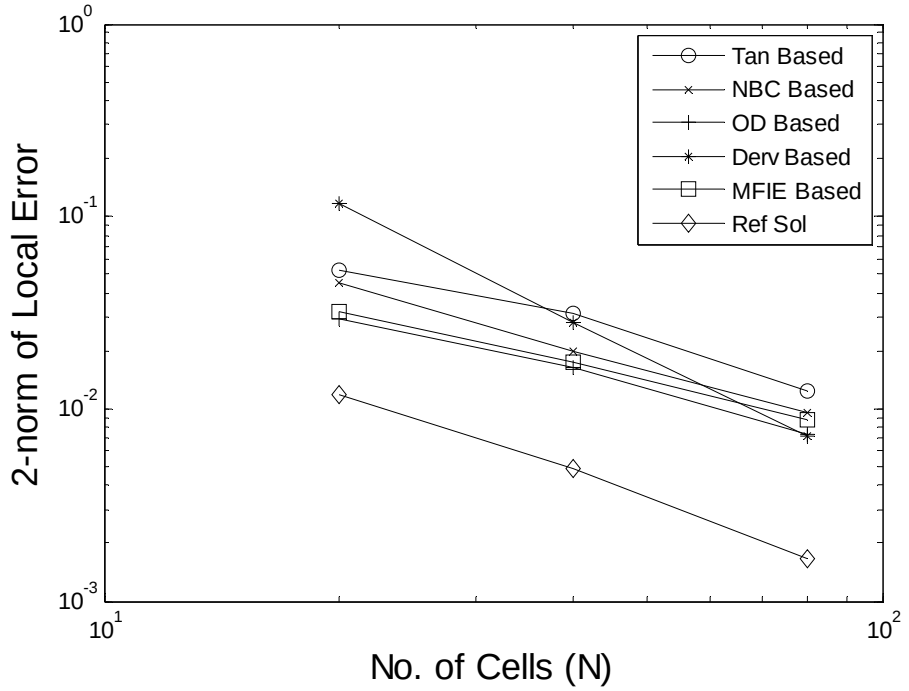

Fig. 4.8: Global error behavior for the problem in Fig. 4.6.

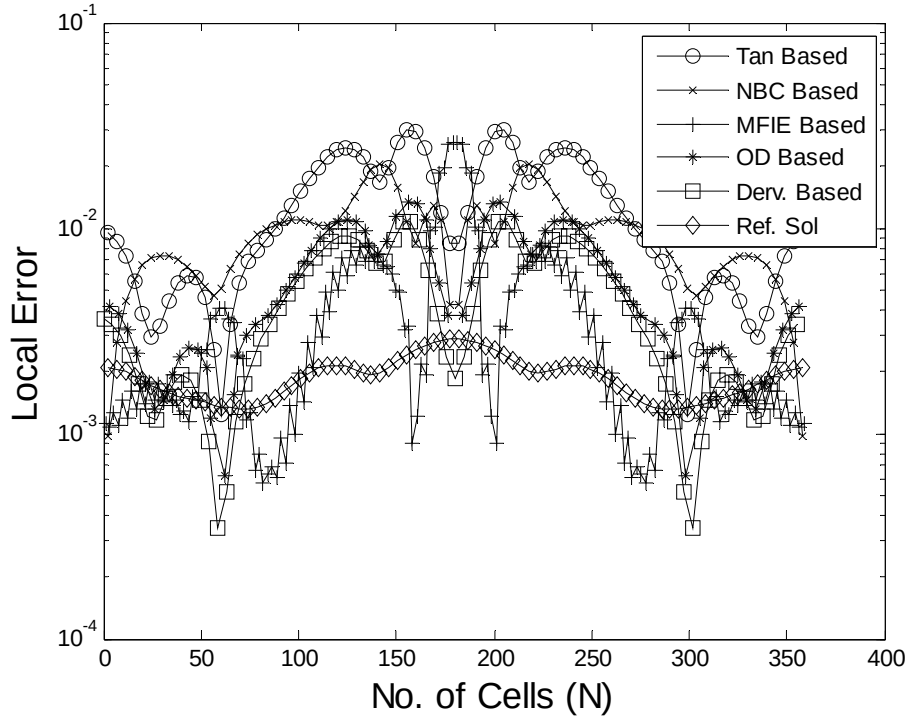

Fig. 4.9: Local error for the problem in Fig. 4.6 when line sources are 0.3λ away.

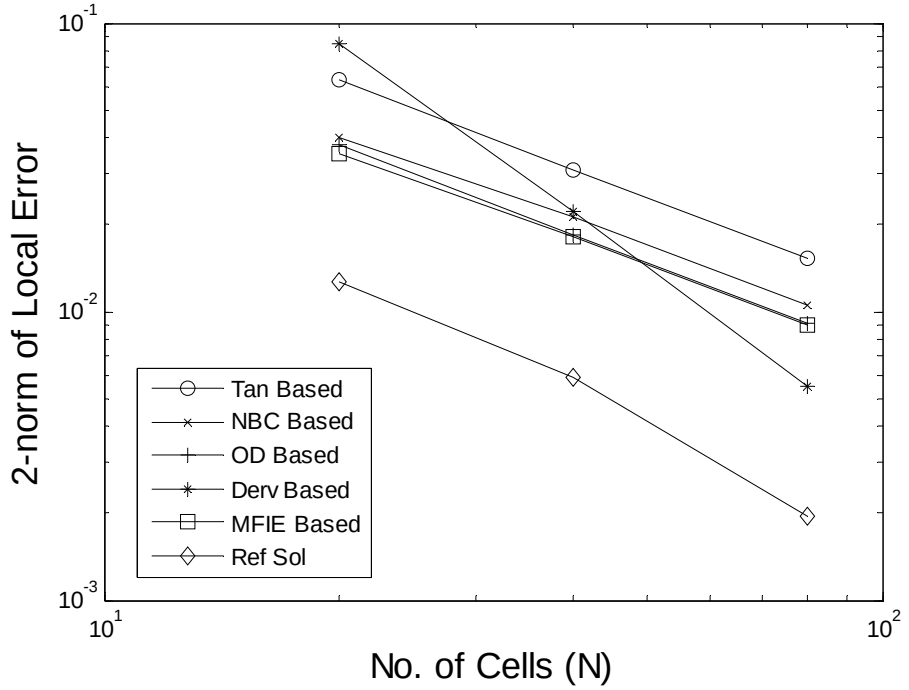

Fig. 4.10: Global error behavior for the problem in Fig. 4.6 when line sources are 0.3λ away.

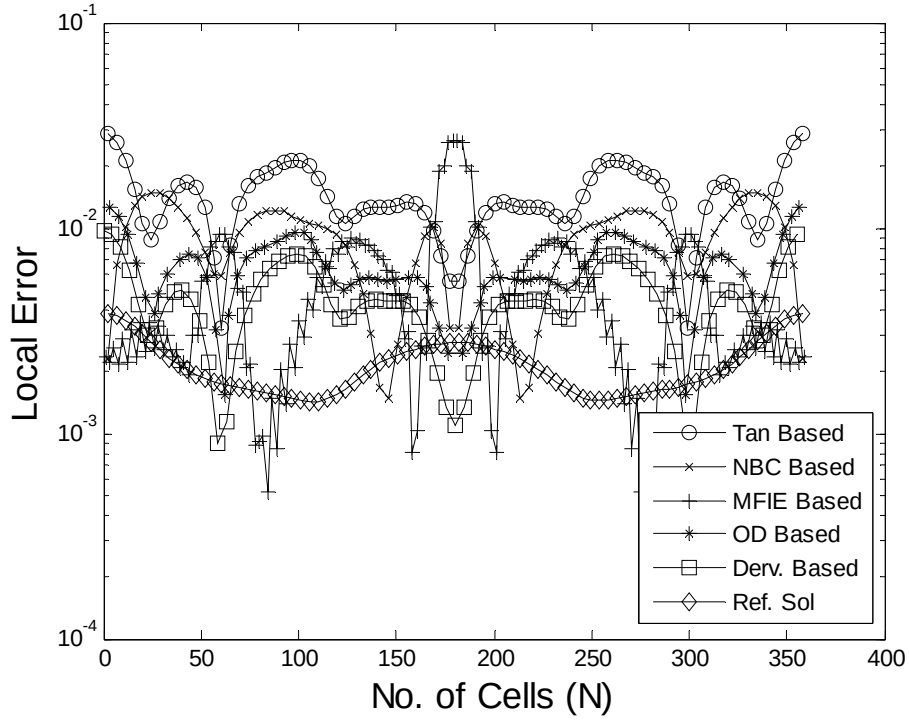

Fig. 4.11: Local error for the problem in Fig. 4.6 when illuminated by a plane wave.

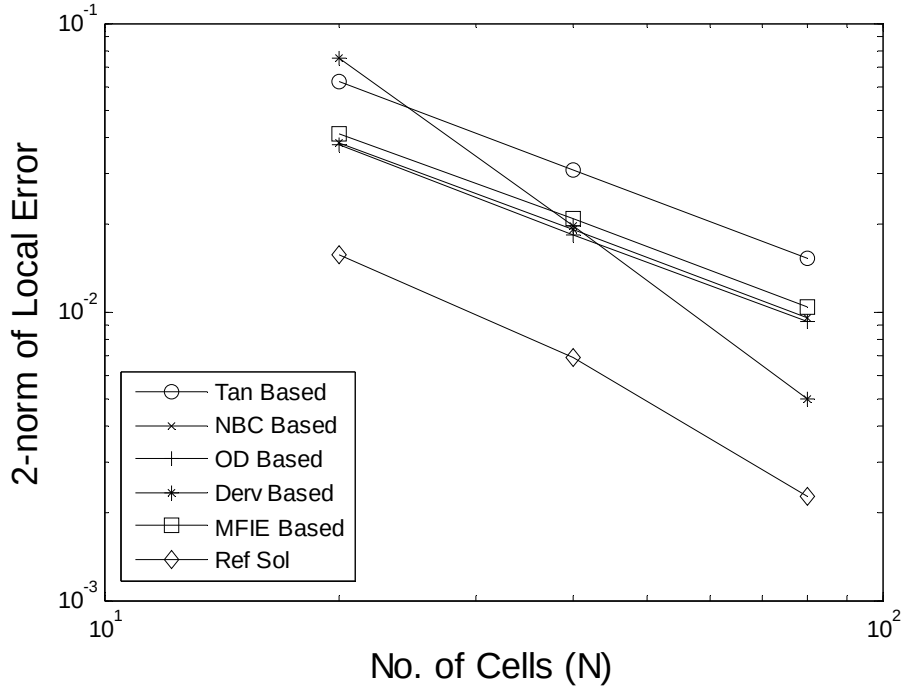

Fig. 4.12: Global error behavior for the problem in Fig. 4.6 for plane wave excitation.

In the third example, we consider a star shaped cylindrical scatterer (Figure 4.13) and illuminate it with the same excitation as used in the last two problems, a pair of line sources placed at a radial distance of 0.3λ. Figures 4.14 and 4.15 show the local and global error estimates. Their behavior is similar in general to that of the preceding two examples. Local error values were computed using an 80-cell model with two node points per cell (q = 2) at the same locations along the scatterer as in the last two examples. The reference solution is based on a 160-cell, q = 2 LCN discretization.

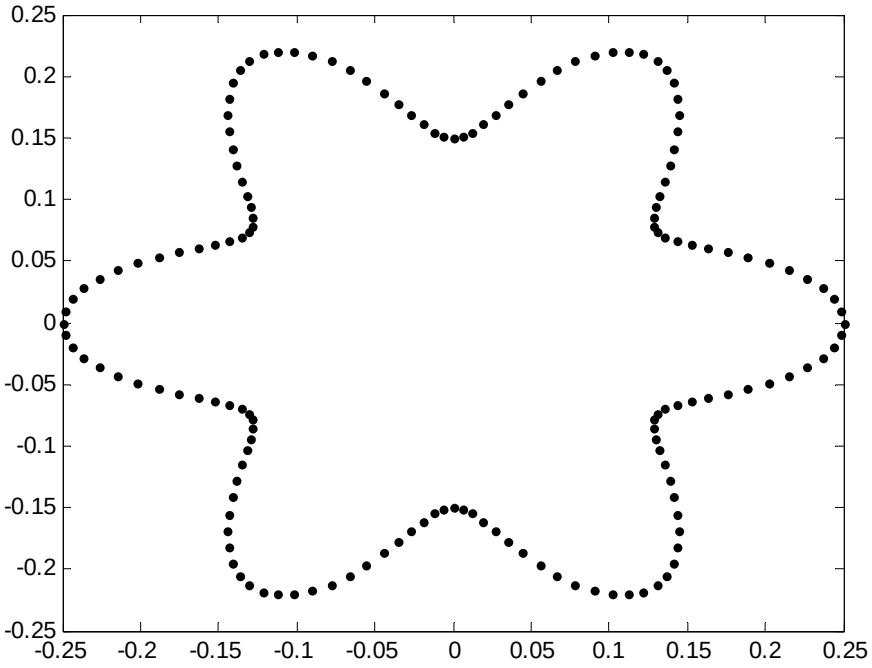

Fig. 4.13: Geometry of the problem.

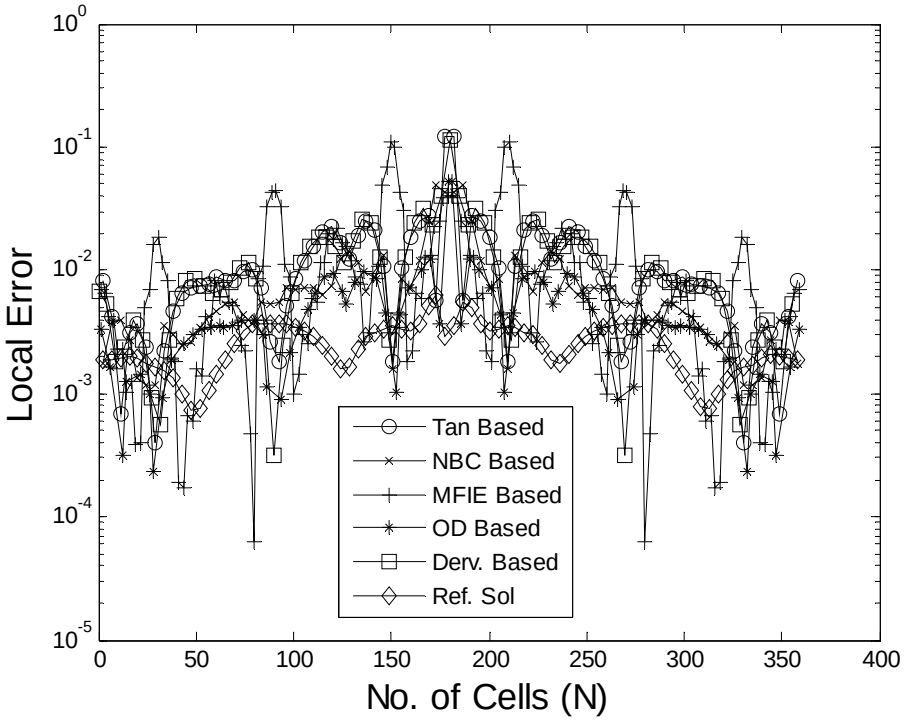

Fig. 4.14: Local error for the problem in Fig. 4.13, computed using the five error estimators.

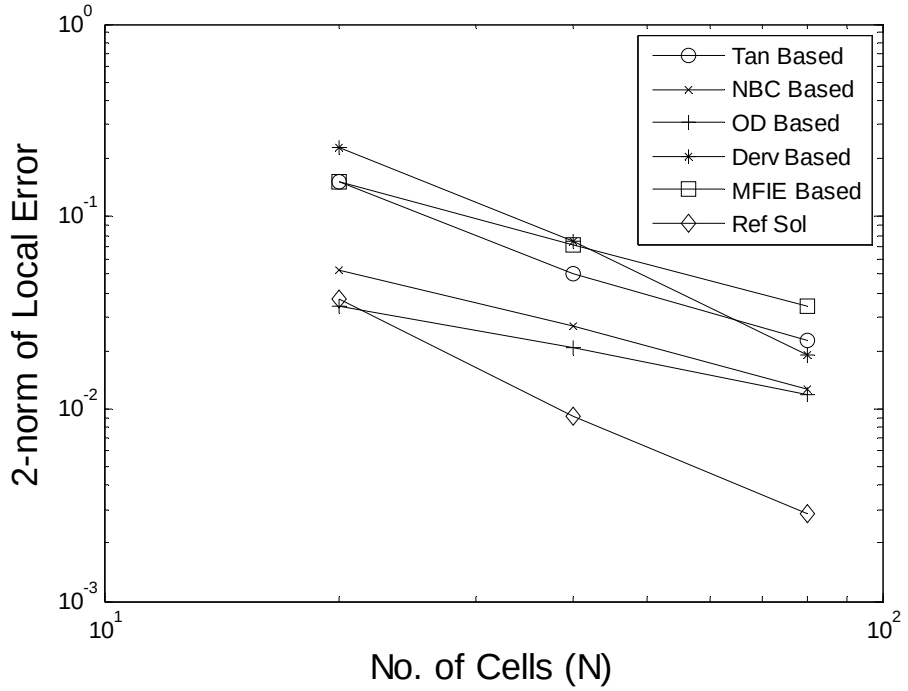

Fig. 4.15: Global error behavior for the five error estimators, for the problem in Fig. 4.13.

From the preceding examples, it appears that all the error estimators correctly identify the high-error regions. While some slightly over-estimate the error, none of them under-estimate it. All of them have a reasonable accuracy as compared to the reference solution and can be used for adaptive refinement schemes, as will be shown in the next section.

4.5 Adaptive refinement

The LCN method lends itself to a straightforward implementation of adaptive *p*-refinement. For the LCN method, the order of the representation is directly related to the number of quadrature nodes, which can easily vary from cell to cell. Increasing the order of the representation also requires that the local correction process be upgraded to a higher order, which involves additional basis functions and a larger local correction system to solve for each cell with

an increased order.

To illustrate the adaptive *p*-refinement, we present a simple implementation. The adaptive refinement technique that we consider begins with the computation of a low order solution, for $q = 1$ or $q = 2$, followed by the determination of the local error distribution as a function of location. In other words, the error estimator produces an array with one error value for each cell in the mesh. That array is sorted in descending order to identify the cells with the largest error. In our specific implementation, the cells with an error in the top 20% are upgraded to a representation order of q+2, while those with errors in the next 20% of the group are upgraded to use a representation order of q+1. The other cells are kept at order q. After the new orders are assigned, the problem is re-solved using the new orders for each cell. The refinement process can be repeated iteratively until the overall error is deemed sufficiently low or until computational constraints prevent further analysis. In the following, we will just consider one step of the p-refinement.

The results from applying one step of the adaptive *p*-refinement scheme to the problem of Figure 4.3 are shown in Figures 4.16 and 4.17. Both the solutions, before and after adaptive refinement, use a 50-cell model. For this example, the error estimator based on the derivative discontinuity of the current density as described in Section 4.3-A was employed to determine the error distribution. The initial value $q = 2$ was used throughout the mesh. Figure 4.16 shows the initial error distribution, and the cells with the largest errors are identified in Figure 4.17. The cells with the largest errors (20% of the cells in the mesh) were upgraded to $q = 4$, while the next group of 20% were upgraded to $q = 3$. The order of the matrix equation therefore increased from 100 to 130. Figure 4.16 shows the error plot for the result after the upgrade. The local error has dropped by more than one order of magnitude in the regions where the order was upgraded.

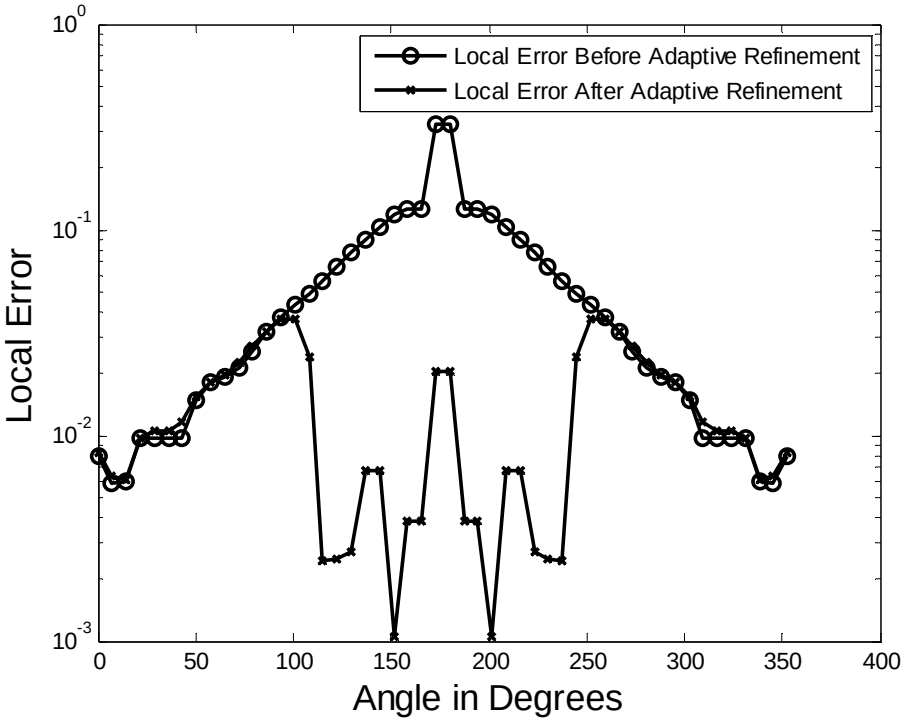

Fig. 4.16: Result from applying one step of the adaptive refinement algorithm to the problem in Fig. 4.3, using the derivative discontinuity error estimator (section 4.3-A).

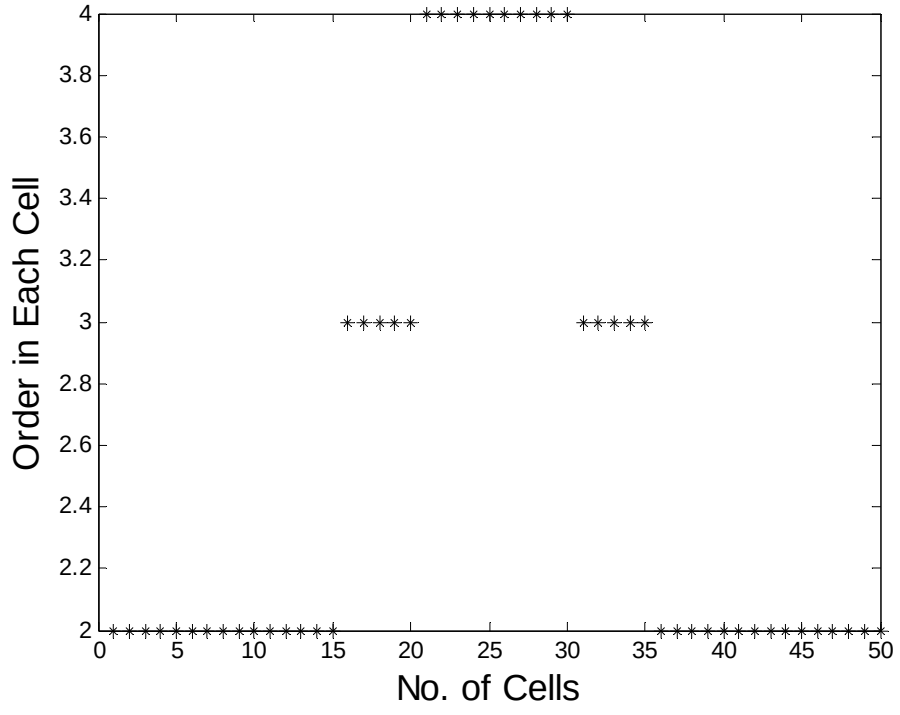

Fig. 4.17: Cell order after the first step of the adaptive refinement algorithm.

In the next example, the adaptive refinement procedure described above is applied to the problem in Figure 4.6, involving the triangular cylinder with rounded corners. Line sources are placed at a radial distance of 0.17λ. For this problem, we used the tangent E-field residual estimator described in Section 4.3-B. Figure 4.18 shows the local error associated with the initial numerical solution, which was obtained with $q = 2$ and a mesh with 80 cells. Figure 4.19 shows the cells that were upgraded to $q = 3$ and $q = 4$ in response to the initial error map, increasing the order of the matrix equation from 160 to 208. The resulting error distribution is also shown in Figure 4.18. The local error has substantially dropped in the regions where the representation was upgraded.

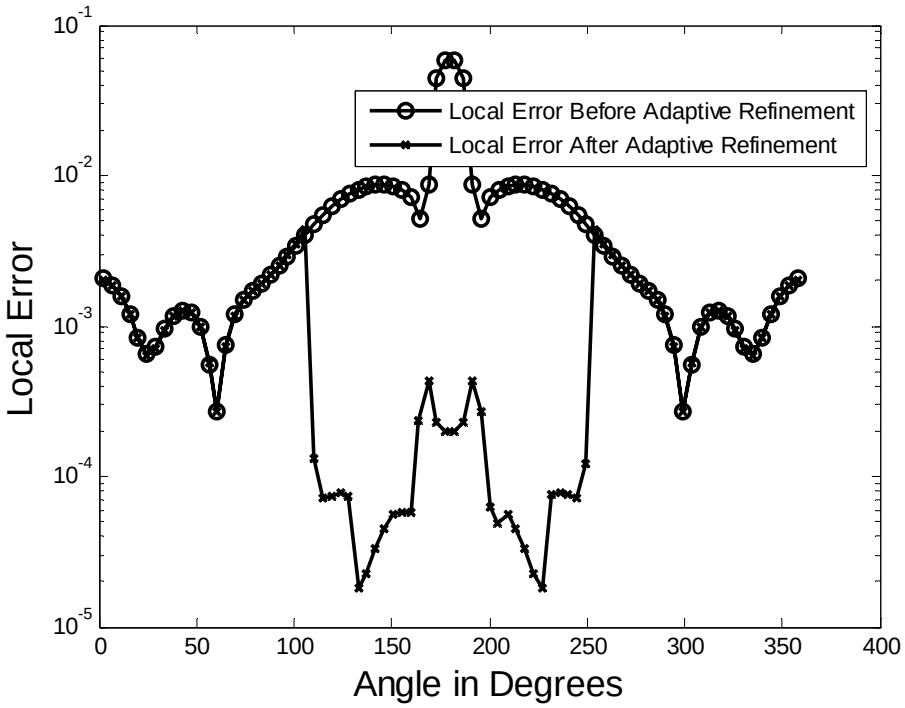

Fig. 4.18: Error distribution before and after one step of adaptive *p*-refinement, based on the tangential E-field residual estimator (section 4.3-B), for the problem of Fig. 4.6.

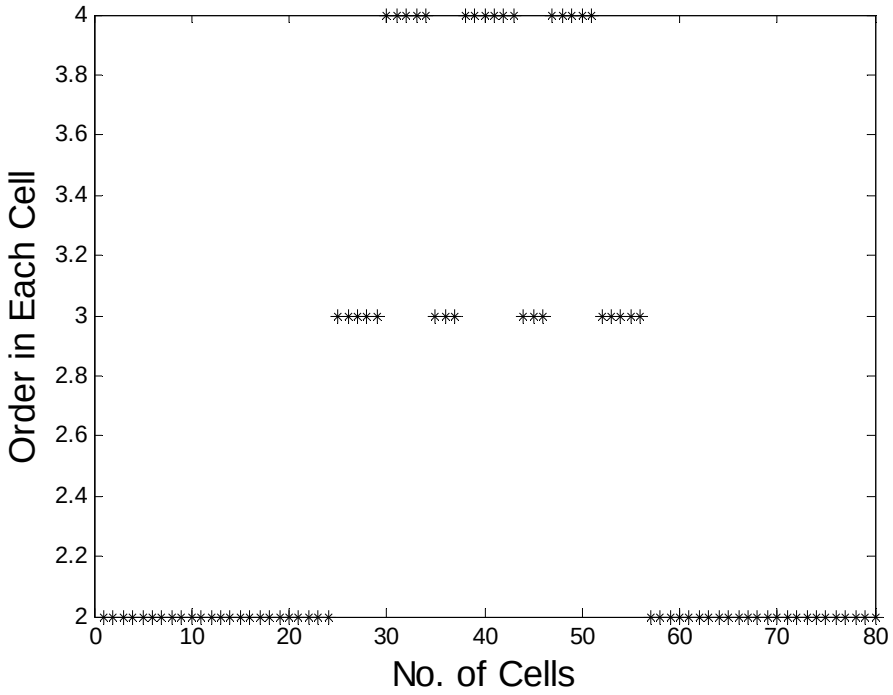

Fig. 4.19: Cell order used for the adaptive refinement step.

We now apply the adaptive *p*-refinement technique to the problem of Figure 4.13. For this problem, we construct a 2:1 over-determined system and employ the error estimator described in Section 4.3-E. Both the solutions, before and after adaptive refinement, use an 80-cell model. Figure 4.20 shows the initial error distribution obtained with $q = 2$ throughout the mesh, and Figure 4.21 shows which cells were upgraded to higher orders. In this case, the original problem involved the solution of a 320 by 160 system, which grew to a system of size 416 by 208 after the first refinement step. The error distribution after one refinement step is shown in Figure 4.20.

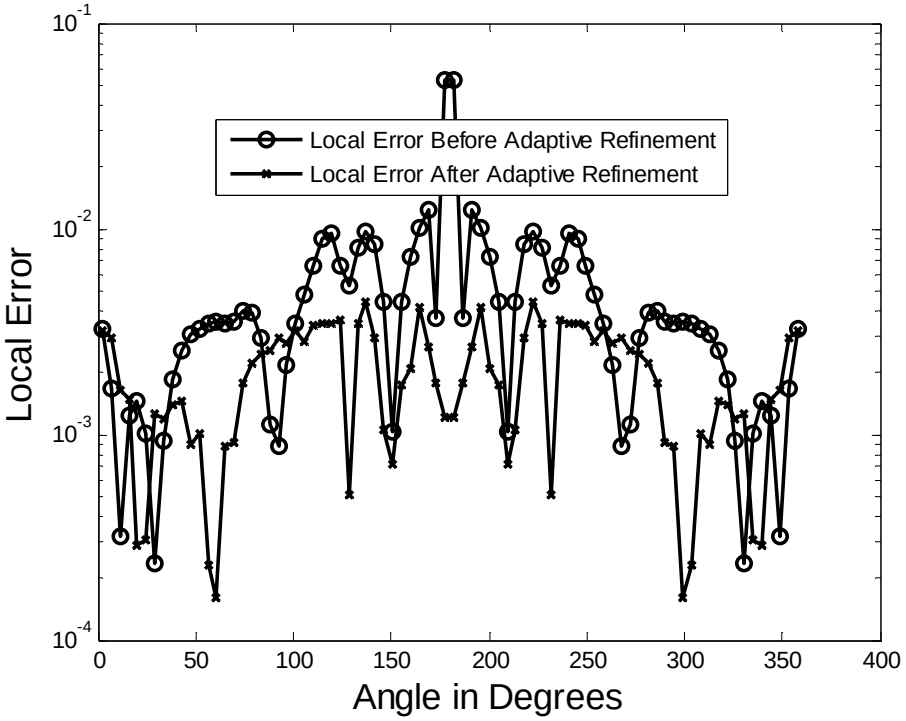

Fig. 4.20: Result of the adaptive refinement to the problem in Fig. 4.13 using the error estimator based on the overdetermined system (section 4.3-E).

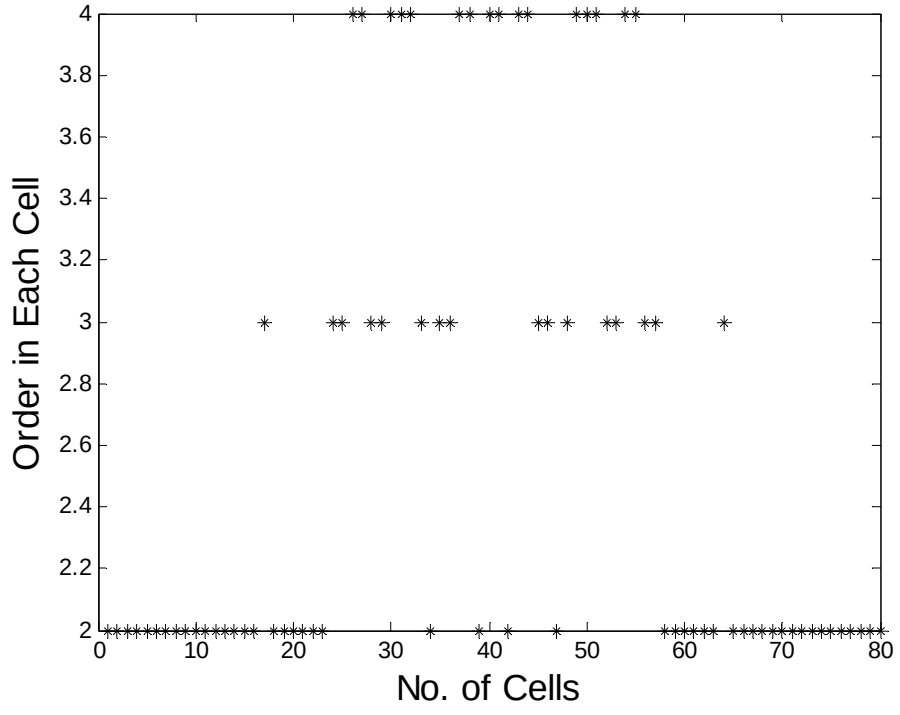

Fig. 4.21: Cell order used for the adaptive refinement step.

In each of the preceding examples, a single step of the adaptive *p*-refinement algorithm was able to reduce the peak error in the current density by an order of magnitude, at least as measured by the error estimators.

4.6 Computational cost of estimators

The relative computational cost of the estimators can be estimated as follows. The baseline cost of the LCN solution for a problem with N cells and uniform order q without error estimation is

$$C_0 \cong \alpha Nq + \beta N^2 q^2 + \gamma N^3 q^3 , \tag{4.33}$$

where α is a constant associated with the local correction part of the matrix fill time, β is a constant associated with the far-field part of the matrix fill time, and γ is a constant associated with the LU factorization solve time, respectively. It is expected that $\beta << \alpha$, since the far-field part of the matrix fill involves just samples of the kernel.

The derivative estimator in Equation (4.12) requires no additional matrix fill, so its computational cost grows as

$$C_1 = \delta Nq \tag{4.34}$$

where δ is a constant. The tangential and normal estimators in Equations (4.16) and (4.21) require a residual computation that is essentially the same as a second matrix fill, and therefore add an approximate cost of

$$C_2 \cong C_3 \cong \alpha Nq + \beta N^2 q^2 , \tag{4.35}$$

where α and β are essentially the same constants used in Equation (4.33).

The MFIE estimator proposed in (4.30) requires a matrix fill for the MFIE operator, which (assuming an LCN discretization of that operator) results in a cost of

$$C_4 \cong \alpha Nq + \beta N^2 q^2 . \tag{4.36}$$

Although the constants α and β in Equation (4.36) are not identical to those used in (4.33), they are likely to be within one order of magnitude of those constants.

The over-determined error estimator has an approximate cost of

$$C_5 \cong 2\alpha Nq + 2\beta N^2 q^2 + 5\gamma N^3 q^3 . \tag{4.37}$$

(In contrast to the previous estimators, this is the total cost of the solution, since the initial operation in Equation (4.33) is not required for this error estimator.) The fill time is double that required in (4.33) since the matrix has twice as many entries, and the solve time is greater by a factor of 5 under the assumption that the QR factorization is employed to generate the least-square solution of the over-determined system [24]. If other techniques (such as singular value decomposition) are used to obtain the least-square solution, the cost will be greater.

For large Nq, we may compare the cost of the initial solution and the error estimate by considering only terms with powers of $N^2 q^2$ and higher. Thus, the current discontinuity estimator has a computational cost that grows as $\gamma N^3 q^3 + \beta N^2 q^2$, the tangential residual, normal residual, and MFIE estimators all have costs that scale as $\gamma N^3 q^3 + 2\beta N^2 q^2$, and the over-determined estimator has a cost that grows as $5\gamma N^3 q^3 + 2\beta N^2 q^2$. The current discontinuity estimator is the least expensive, while the over-determined estimator is (by far) the most expensive.

4.7 Concluding remarks

Five different error estimation techniques have been studied in connection with the LCN solution of electromagnetic integral equations. Simulation results show the performance of the estimators and their capability to correctly locate high-error regions. A relatively simple adaptive

p-refinement algorithm was implemented to demonstrate the potential of the proposed error estimation schemes. The relative computational cost of the proposed error estimation schemes was also presented.

From the global error plots in Figures 4.5, 4.8, 4.10, 4.12, and 4.15, it appears that the over-determined estimator usually provides the most accurate estimate of the true global error, although for many of these examples the normal-based estimator and the MFIE-based estimator were essentially as accurate. For most of these examples the derivative-based estimator produced a global error curve with a different slope from that of the other estimators. (This issue will be discussed in Chapter 6.) From plots of the local error, none of the estimators closely tracks the actual reference error in the current, although all correctly identify the region of largest magnitude current density as that with the greatest error.

CHAPTER 5

AN IMPLICIT ERROR ESTIMATION TECHNIQUE AND ADAPTIVE REFINEMENT FOR THE LOCALLY-CORRECTED NYSTRÖM METHOD

In this chapter, an alternative adaptive *p*-refinement scheme for the locally-corrected Nyström solution of the electric field integral equation is demonstrated [32]. In contrast to the previous chapters, this approach uses an *implicit* error estimation scheme to determine what parts of the target model are refined. The error estimate is obtained from a set of higher-order solutions to smaller local problems, using a lower-order solution for the remainder of the geometry. The proposed scheme is demonstrated for a two-dimensional transverse-electric conducting target that has localized high-error regions. It is shown that higher error regions are correctly identified and refined by the proposed scheme.

5.1 Introduction

As discussed in previous chapters, high order solutions of integral equations can often be obtained more efficiently using the locally-corrected Nyström (LCN) method than with the method of moments (MoM), because the LCN approach avoids most of the expensive integrations that the MoM requires [5]. The LCN method also lends itself to an easy implementation of adaptive *p*-refinement techniques, where the order of the representation is improved in certain regions of the problem geometry [33].

Adaptive refinement algorithms need to identify the regions of the problem domain where numerical error is relatively high and this is done by the use of a suitable error estimation

technique. In this chapter, we demonstrate an implicit error estimator similar to that used with the MoM in [25]. The implicit estimator uses a higher-order solution to a sub-problem involving just a few cells on the surface of the target, in conjunction with a lower-order solution for the remainder of the geometry, to find an estimate for the error in the region of the few cells. This is in contrast with the explicit error estimators used in previous chapters, which solve for the current density on the whole domain and employ a secondary step of processing that information to obtain an estimate [7].

In this chapter, the adaptive *p*-refinement technique is applied to the electric field integral equation (EFIE) for the transverse electric (TE) polarization using the LCN method. We use curved cells defined by Lagrange polynomials to accurately model the scatterer geometry. The integral equation to be solved can be written as [5]:

$$E_t^{inc}(t) = j\frac{\eta}{k}\int_{\Gamma} J_t(t)D(t,t')\,dt', \tag{5.1}$$

where

$$\begin{aligned} D(t,t') = \{&k^2\cos[\Omega(t)-\Omega(t')] + \sin\Omega(t)\sin\Omega(t')\frac{\partial^2}{\partial x^2} \\ &- \sin[\Omega(t)+\Omega(t')]\frac{\partial^2}{\partial x\partial y} + \cos\Omega(t)\cos\Omega(t')\frac{\partial^2}{\partial y^2}\}\frac{1}{4j}H_0^{(2)}(kR). \end{aligned} \tag{5.2}$$

The kernel in (5.2) behaves as $O(R^{-2})$ for small arguments, indicating the hyper-singular nature of the integral operator. As long as the observer is sufficiently away from the source (0.2λ in our case), we can directly sample *D*; otherwise, a local-correction procedure based on matching near-field values produced by a set of known bases (Legendre polynomials in our case) is used to construct a bounded kernel which is then used to compute the corresponding impedance matrix entries. Details on this procedure have been documented previously in Chapters 2 and 4.

The LCN technique is used to solve for the current density J_t along the contour of the scatterer. Below, we describe the implicit error estimation scheme followed by the *p*-refinement method. Simulation results for several example scatterers are presented in Section 5.4.

5.2 Implicit error estimation technique

The structure under consideration is first discretized into N curved cells $\{c_i\}$, as previously described in Chapter 4. A "lower-order" solution J_q is computed using the LCN method with a uniform representation of order q (q-point quadrature) in each cell. Next, a window of 3 adjacent cells $\{c_{k-1}, c_k, c_{k+1}\}$ is taken, and a new current density J_{q+1} is computed on these 3 cells, using a representation order of q+1. The 3-cell problem is solved using the order-q results in the other N–3 cells as the sources of an additional incident field. Thus, the 3-cell problem only requires the solution of a 3q by 3q system of equations. The normalized change in the complex-valued current density at the midpoint (t = 0) of the center cell c_k is taken as a measure of the relative error in cell c_k. This error estimate is given by:

$$e_k = \frac{\left| J_q(c_k|_{t=0}) - J_{q+1}(c_k|_{t=0}) \right|}{\max(|J_q|)}. \tag{5.3}$$

If the value of the current density is not directly defined at the cell center (due to the location of quadrature rule nodes), an interpolation procedure [5] using Legendre polynomials is used to compute the current density there.

The window is shifted by 1 cell and the 3-cell procedure is repeated until an array of size N is formed containing the relative error estimates for each cell. These are local error values. The global error can be computed as the l_2-norm of the sequence of N local-error values from the array.

5.3 The *p*-refinement technique

Once the error has been estimated using the implicit technique, the *p*-refinement procedure is essentially the same as that discussed in Chapter 4. The typical LCN implementation involves an independent representation in each cell of the model, and thus, it lends itself to an easy implementation of *p*-refinement. In other words, the adaption involves changing the order (or the number of nodes) of the quadrature rule in each cell. The regions of the problem domain that have relatively high error are assigned a higher-order rule than the ones that have lower error. The technique for adaptive refinement that we have implemented requires the local-error values to be sorted in descending order. For illustration, we use an empirical scheme where the top 20% of the cells are assigned order q+2, the next 20% are assigned order q+1, and the remaining cells are left unchanged at order q. Once the order in each cell is determined, the problem is re-solved for the new values of current density. The process can be repeated until a sufficient global error level is achieved. This simple technique is used here for illustration; it is not necessarily an optimal one for efficient *p*-refinement.

5.4 Simulation results

Consider a 5λ circumference circular cylinder illuminated by two line sources placed at a radial distance of 0.1λ away from the surface of the cylinder (Figure 4.3 of Chapter 4). The region of the cylinder near the line sources ($\varphi = 180°$) is expected to have more error in current density than the regions far away. Figure 5.1 shows the error estimate obtained from the implicit error estimator described above, while transitioning from $q = 2$ to $q = 3$ for a 50-cell model of the cylinder contour. The error estimate (shown as the change in J) is highest at $\varphi = 180°$, as expected.

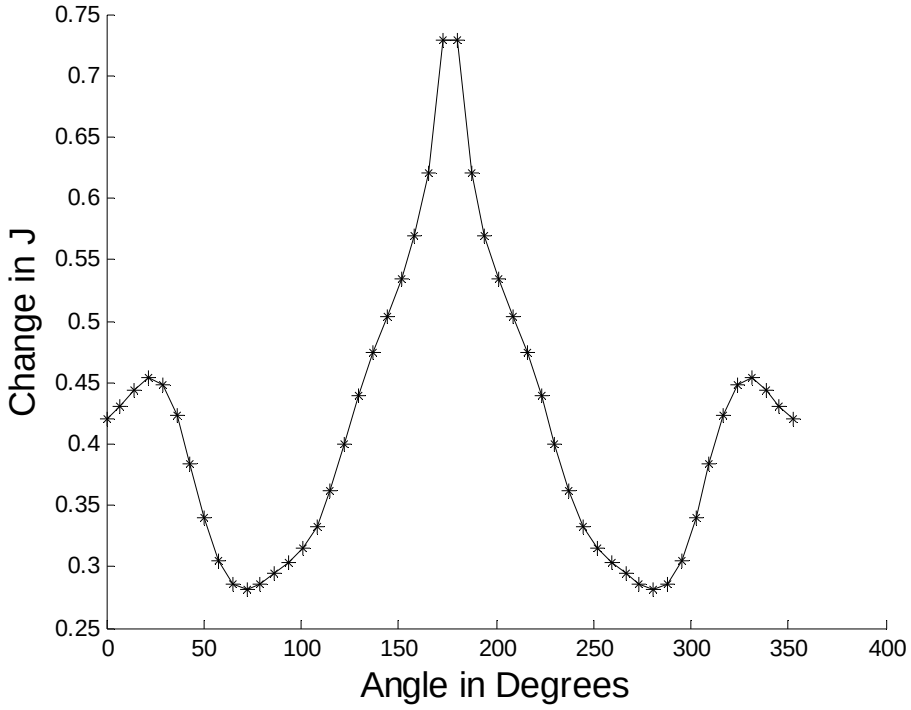

Fig. 5.1: Cell-by-cell distribution of the error, as obtained by the implicit error estimator.

Our refinement scheme assigns an order q+2 to the 20% of the cells with the largest error, assigns an order q+1 to the next 20%, and leaves the remaining cells unchanged at order q. Figure 5.2 shows the distribution of the cells with the new order resulting from the refinement procedure. Figure 5.3 shows the result of the p-refinement process, by plotting the actual normalized error in the current densities, computed before (with a uniform order of q=2) and after the adaptive refinement procedure is applied (with variable orders given in Figure 5.2). The matrix equation increased from order 100 to order 130 after the refinement step. These two results are compared to a reference solution obtained from a 400-cell model and a uniform order of q=4 to determine the actual error (a system of order 1600). The regions of the problem that were identified by the error estimator as having the largest error exhibit about an order of magnitude reduction in actual error after refinement.

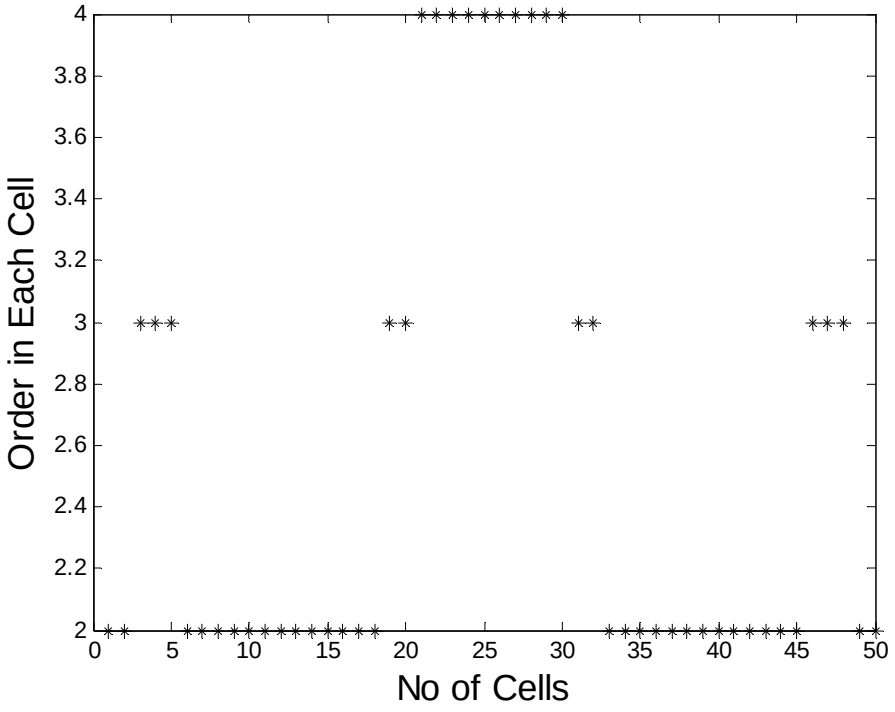

Fig. 5.2: Cell order determined from the error estimate.

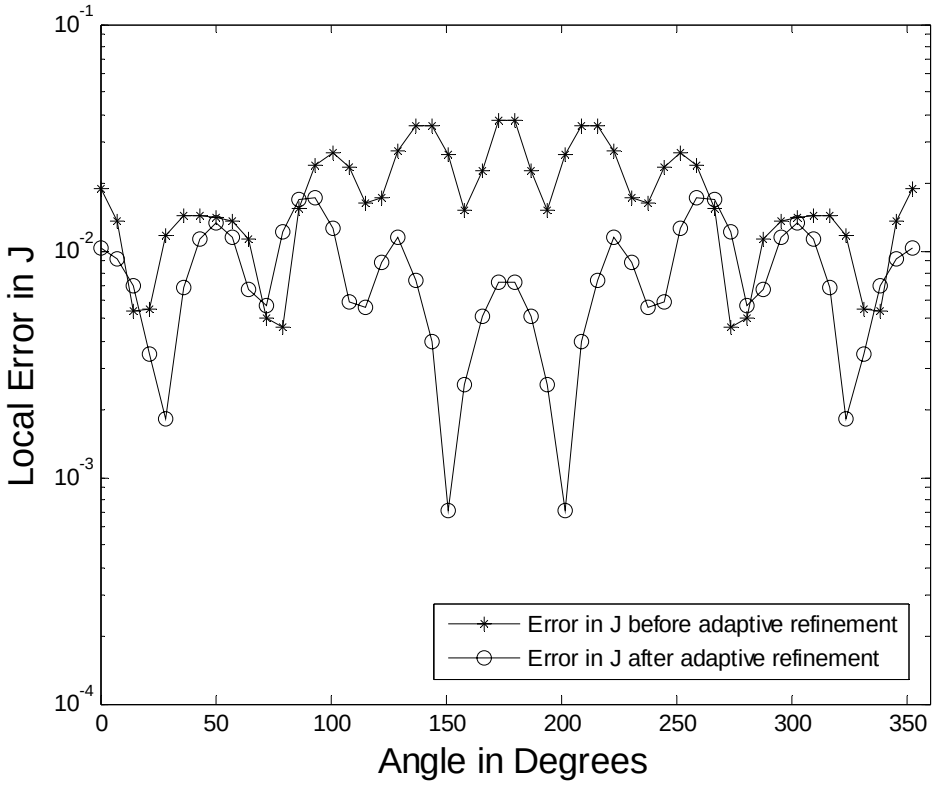

Fig. 5.3: Local error in current density before and after adaptive refinement.

For the preceding circular cylinder example, the combination of the implicit estimator and the simple *p*-refinement scheme results in a more uniform distribution of the peak local error than that produced by the initial numerical result. Since a uniform error level is generally preferred, one can conclude that the *p*-adaptive LCN procedure improves the efficiency of the solution process.

As a second example, we consider the smooth triangular cylinder problem (Figure 4.6 of Chapter 4) illuminated with a pair of line sources placed at a radial distance of 0.17 λ. The cylinder is modeled with 80 cells. Figure 5.4 shows the error distribution obtained from the implicit estimator for a transition from $q = 2$ to $q = 3$. Figure 5.5 shows the cell order obtained from the simple refinement algorithm described above (the 20% of the cells with the largest error elevated to q=4, while the next 20% are elevated to q=3). Figure 5.6 shows the actual error in the current density before and after the refinement step. The initial result was calculated for a uniform order of $q = 2$ and involved a matrix equation of order 160; the refined result employed the cell orders given in Figure 5.5 and a system of order 208. The reference solution used a 160-cell model and a uniform order of $q = 4$, for a system of order 640.

For the smooth triangular cylinder example, the error in J is reduced by an order of magnitude in the regions identified by the estimator as having the largest error. In fact, the final error distribution in Figure 5.6 is dominated by the parts of the structure where the current density was not refined. This example illustrates a drawback of the simple refinement scheme being used here for illustration; obviously it might be necessary to carry out several adaptive refinement steps before obtaining a sufficiently uniform error level. In addition, a more sophisticated process can be developed that adjusts the range of orders and the number of cells that are refined as a function of the dynamic range of the original error levels.

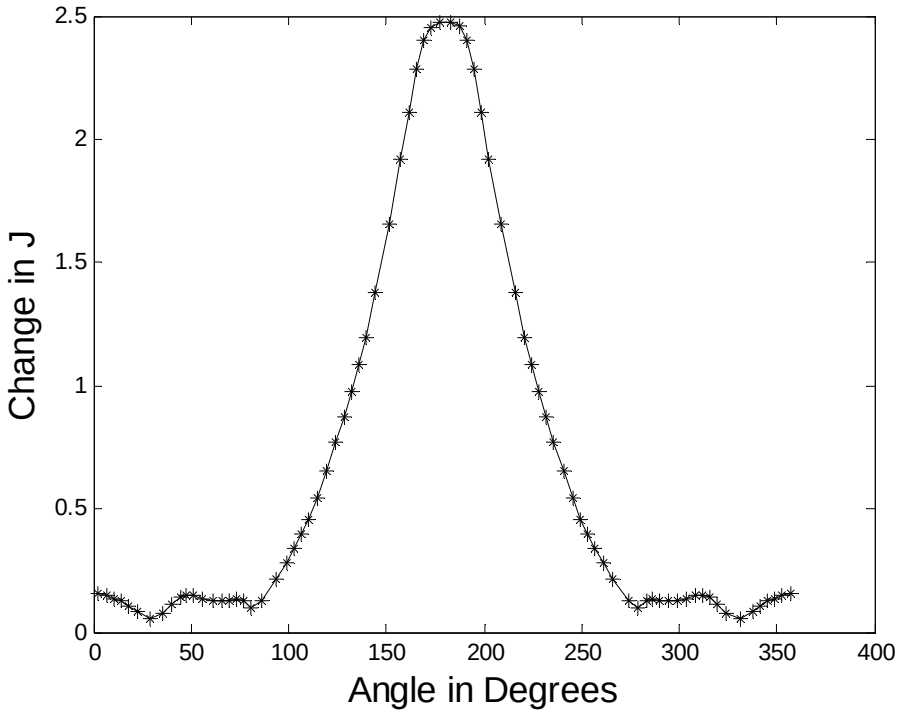

Fig. 5.4: Cell-by-cell distribution of the error produced by the implicit estimator.

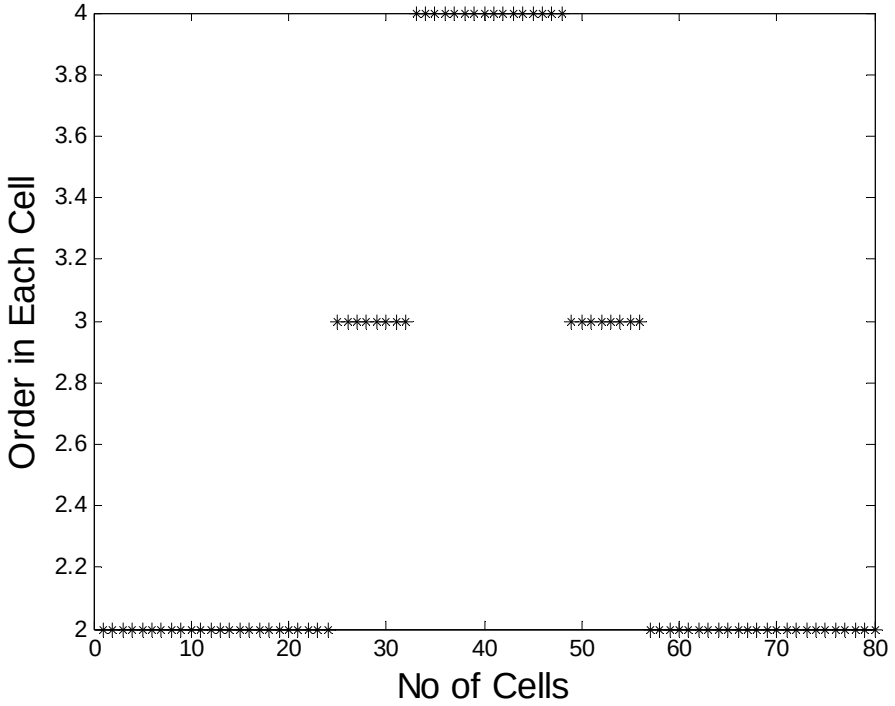

Fig. 5.5: Cell order determined from the error estimate.

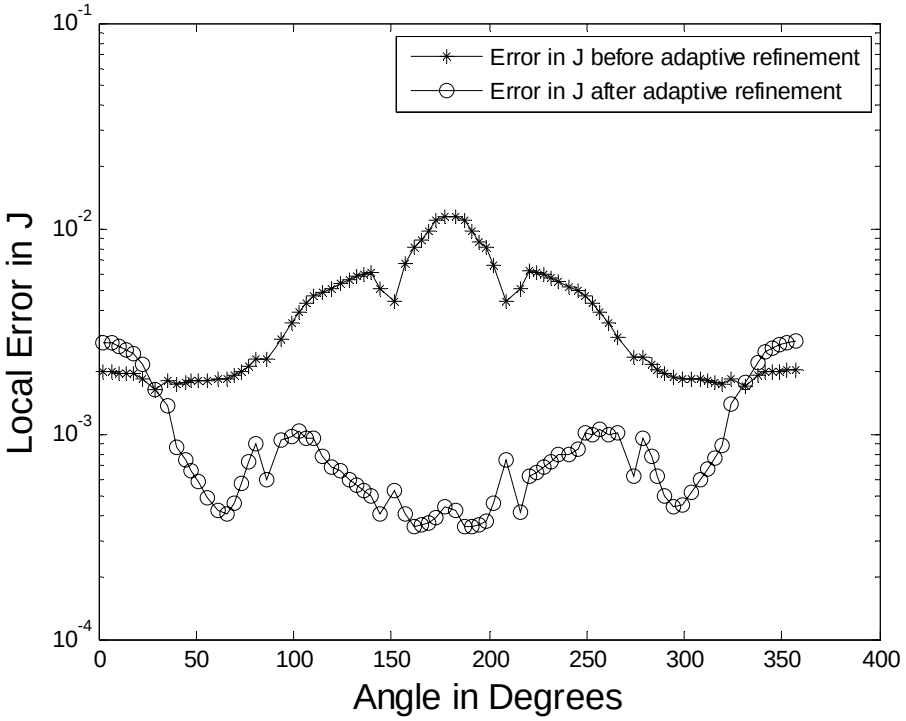

Fig. 5.6: Local error in current density before and after adaptive refinement.

The third example involves a smooth star shaped cylinder (Figure 4.13 of Chapter 4) illuminated with a pair of line sources placed at a radial distance of 0.27λ. A model of 80 cells is used. Figures 5.7 and 5.8 show the error distribution obtained from the implicit error estimator and the cell order obtained from the simple refinement scheme, respectively. As in the preceding examples, the estimator employed a transition from q = 2 to q = 3, and the simple refinement algorithm elevated the order of the 20% of the cells with the largest error to q=4, and the next 20% to q=3. The baseline result involved a matrix of order 160; the refinement one of order 208.

Figure 5.9 shows the actual error in the current density before and after refinement. The initial result was calculated for a uniform order of q = 2; the refined result employed the cell orders given in Figure 5.8. A reference solution based on a 160-cell model and a uniform order of q = 4 (matrix order 640) was used to determine the actual local error in current density.

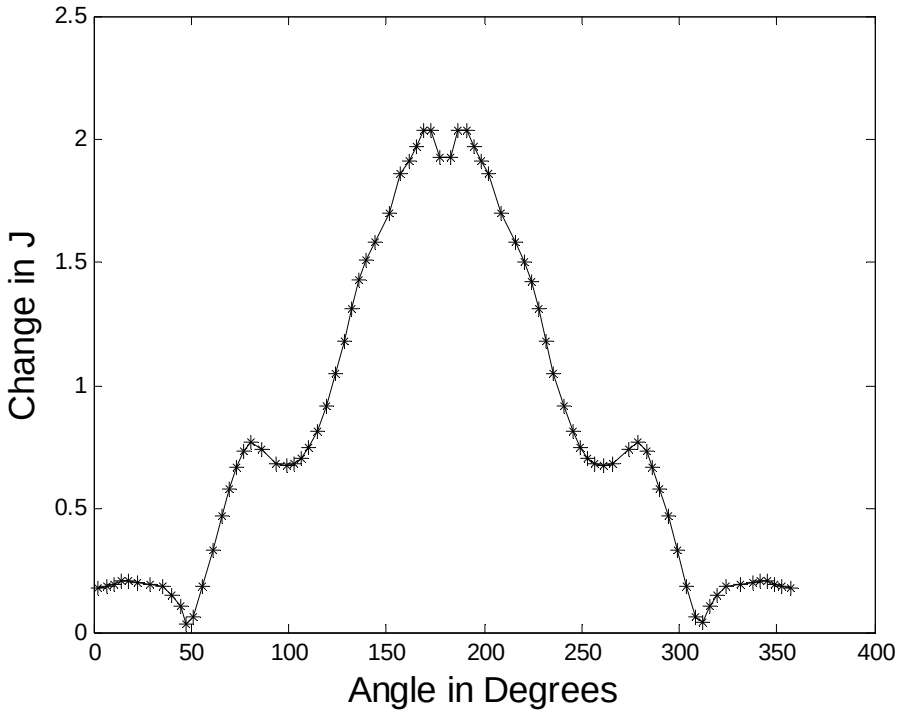

Fig. 5.7: Cell-by-cell distribution of the error produced by the implicit estimator.

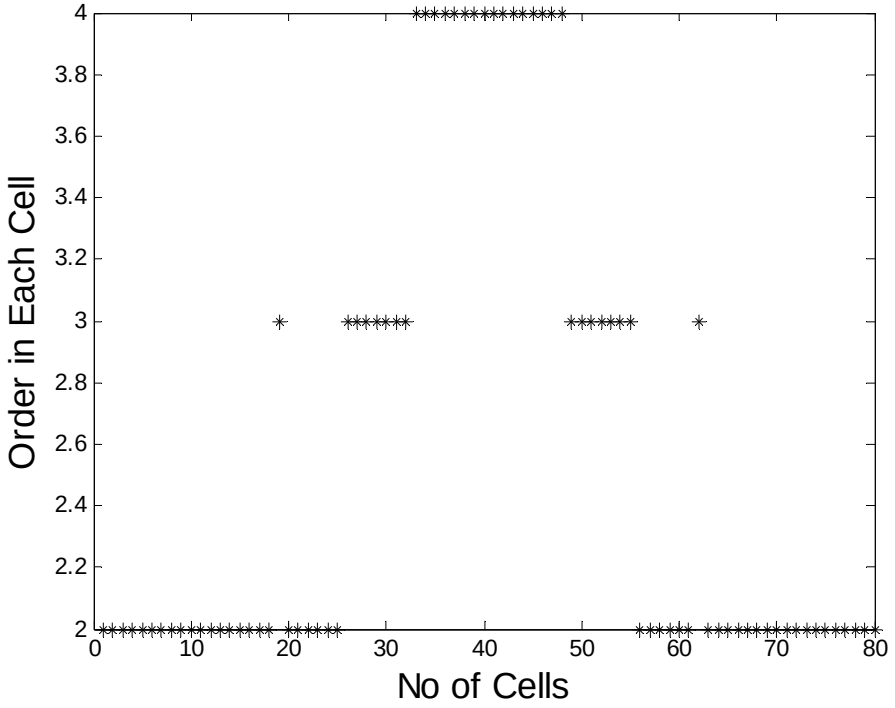

Fig. 5.8: New cell order obtained from the error estimate.

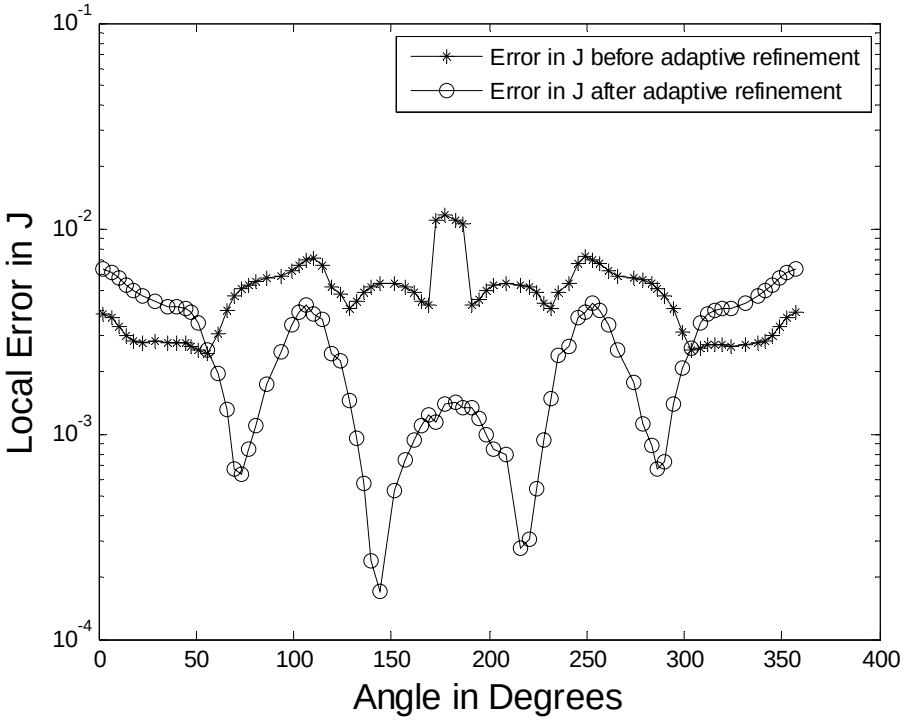

Fig. 5.9: Local error in current density before and after adaptive refinement.

The final example involves the key-sectional cylinder (Figure 3.2a from Chapter 3) illuminated with a pair of line sources located at a radial distance of 0.7λ. The structure is modeled with 75 cells and the baseline solution was calculated using a uniform representation of order q = 2. Figure 5.10 shows the error distribution obtained from the estimator when transitioning from q = 2 to q = 3. Figure 5.11 shows the distribution of cell orders obtained using the simple refinement algorithm employed in the preceding examples (cells with error levels in the top 20% are elevated to q=4, and the next 20% are elevated to q=3).

Figure 5.12 shows the actual error in the current density before and after refinement. The initial result was calculated from a matrix of order 150; the refined result employed a system of order 195. A reference solution based on a 150-cell model and a uniform order of q = 4 (a system of order 600) was used to determine the actual local error in current density.

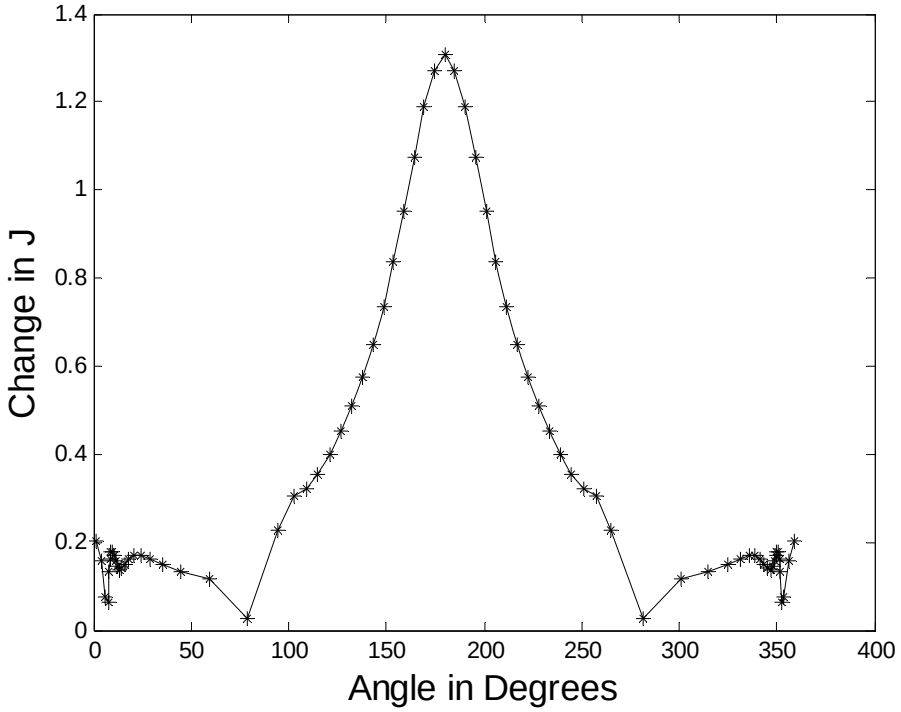

Fig. 5.10: Estimated error distribution for the key-sectional cylinder.

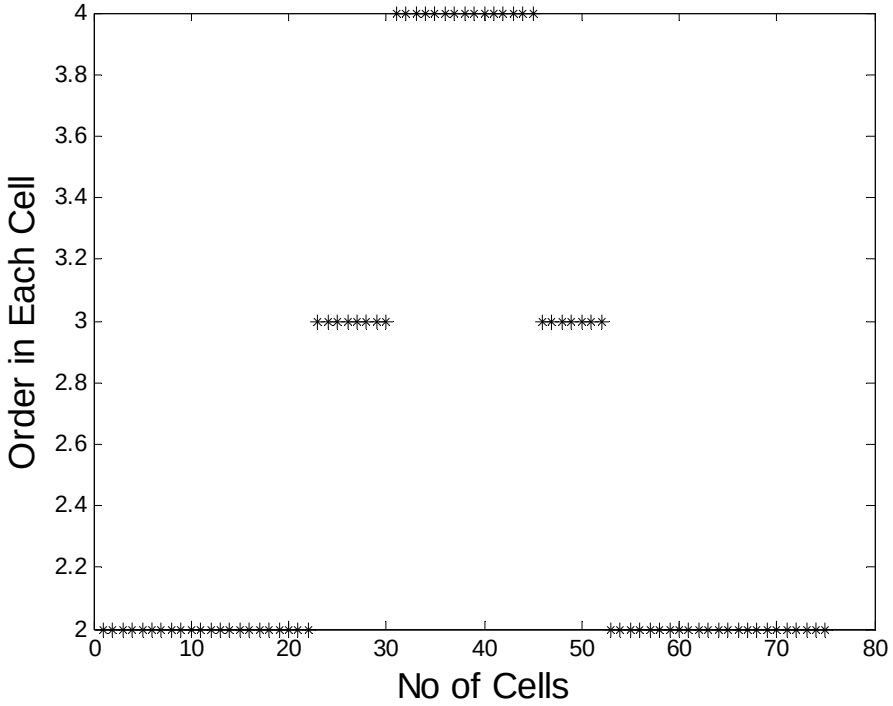

Fig. 5.11: New cell order obtained from the error estimate.

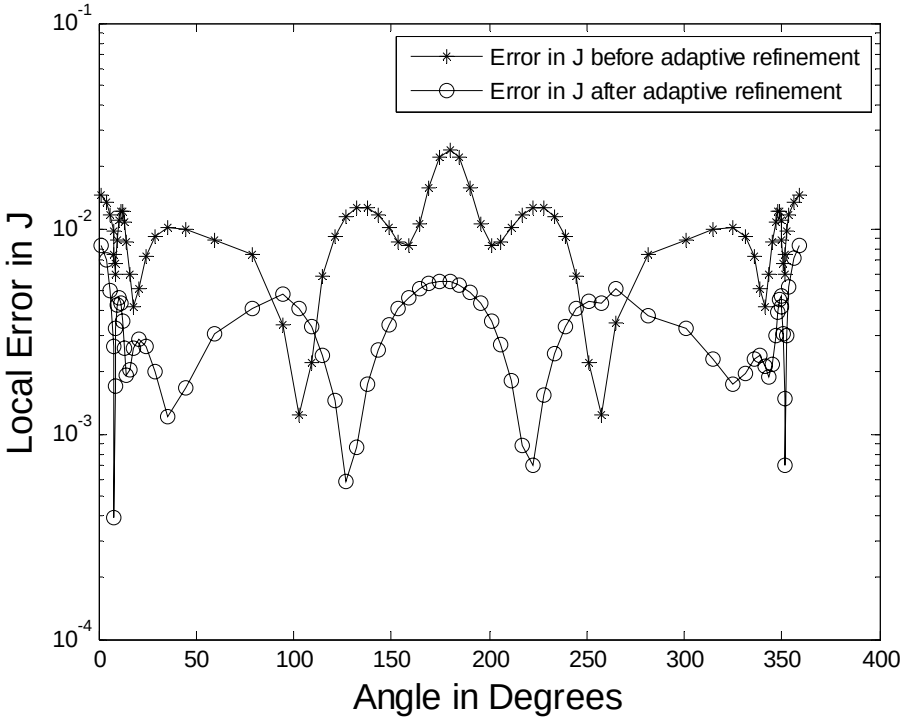

Fig. 5.12: Local error in current density before and after adaptive refinement.

For the key-sectional cylinder, it is noteworthy that the implicit error estimate in Figure 5.10 is very different in character from some of the explicit estimators used previously for this problem in Chapter 3. Several of the estimates in Figure 3.2b from Chapter 3 contain large spikes near the surface discontinuities in the key-sectional cylinder structure. However, the implicit estimator does not produce an error spike for this example. Many practical structures contain edges or other surface discontinuities that give rise to singularities in the current or charge density. These singularities may not be incorporated into the representations used for the current density, and consequently those error spikes will dominate the error estimates regardless of the extent of refinement. Additional research is needed to determine whether this behavior of the implicit estimator is consistent across a wide range of geometries, and if so whether it is an advantage or disadvantage compared to the explicit estimators.

5.5 Concluding remarks

In this chapter, an implicit error estimation scheme is tested in conjunction with the LCN method. Its utility is demonstrated for several examples using a simple *p*-refinement technique. For all the examples, the implicit estimator correctly identified regions where the current density exhibited the largest error.

As implemented here, the cost of the implicit estimator can be approximated as follows, assuming that the baseline calculation for N cells and uniform order q has already been carried out. Each 3-cell calculation requires a system of order $3(q+1)$; therefore N such system involve the computation of $9N(q^2+2q+1)$ matrix entries. The solution of the additional N systems, assuming a computational cost of $O(m^3/3)$ to solve an order-m system using LU factorization, is proportional to $9N(q^3+3q^2)$. These costs compare favorably with the explicit error estimators considered in previous chapters.

For the examples considered in this chapter, which were deliberately constructed to exhibit a large error in one region of the problem, the combination of the error estimation process and a single step of the simple *p*-refinement algorithm usually led to a fairly uniform error distribution being obtained from the LCN approach. This supports the two potential advantages of the *p*-refinement LCN procedure: first, it increases user confidence in the accuracy of the result, and second, it offers a more computationally efficient solution process than the current practice.

CHAPTER 6

IMPROVING ERROR ESTIMATION FOR INTEGRAL EQUATION FORMULATIONS

Chapters 3, 4, and 5 presented various error estimation techniques that can be used with the MoM and the LCN solutions of electromagnetic integral equations. The approach adopted in those chapters is primarily empirical. In this chapter, we explore some of the mathematical foundations for error analysis in order to provide a better framework for an understanding of error estimation.

In chapter 3, it was observed that the global residual error and global current error decrease at different rates as the cell sizes decrease. Thus we begin by reviewing the notion of interpolation error and the convergence rates associated with numerical solutions. We also identify the expected rates at which various quantities (current density, residuals) converge.

Finally, we consider the possibility of scaling the residual error estimators used in previous chapters to better approximate the actual current density error over a range of cell sizes. Although this approach is not entirely successful, there are indications that it can be used to improve the accuracy of the residual estimators.

6.1 Interpolation error

Suppose a given function f needs to be approximated using a set of polynomial functions $\{p_n\}$. The error in the approximation is known as the *interpolation error*. This error will be dependent upon the nature of f and on the order of the polynomials available in the set $\{p_n\}$.

Suppose f is a linear function $ax + b$ defined on some interval of size h, and the set $\{p_n\}$ consists of only a constant function, p_0. The constant will not be able to approximate the linear term ax. As the interval size h is reduced, the difference between the function $ax + b$ and the approximation p_0 will be proportional to ax, which in turn is bounded by ah. We say that the error is "order h" or $O(h)$ in that case.

Similarly, if f is a quadratic function $ax^2 + bx + c$ defined on an interval of size h, and the set $\{p_n\}$ consists of constant and linear polynomials, the interpolation error will be bounded by ah^2 as h decreases, or $O(h^2)$. In general, the interpolation error is dominated by the first "missing" polynomial degree greater than the highest order polynomial in the set $\{p_n\}$. Thus, when representing a function with polynomials of degree p, one expects an interpolation error proportional to $O(h^{p+1})$.

6.2 Error behavior of *J*, the current density

In the MoM solution to an integral equation, the error in the solution mainly arises from the inability of the bases to represent variations in the unknown, or equivalently the interpolation error [4]. If a set of polynomial bases functions with highest degree p is employed to represent an unknown, then that set can exactly represent the unknown only if the unknown is a linear combination of polynomials having degree less than or equal to p. Therefore, for other functions the interpolation error using such a set of bases behaves as $O(h^{p+1})$, where h is proportional to the largest cell size within the mesh.

In chapter 3, for example, several problems were solved using the MoM with piecewise linear bases (triangular functions) for which $p = 1$. The error in the current density, as the mesh was refined with successively smaller cells, was observed to behave as $O(h^2)$ as expected.

Similarly, the error in the LCN solution of the TE EFIE was observed to behave as $O(h^q)$ where q is the order of the quadrature rule in each cell. The quadrature order is related to the polynomial degree p by $q = p + 1$, making the error in the LCN solution $O(h^{p+1}) = O(h^q)$, also as expected. These observations support the idea that the primary source of error in numerical solutions of this type is the interpolation error.

6.3 Error behavior of the residual

As discussed in Chapter 2, the residual error for a general equation

$$L\{f\} = g, \tag{6.1}$$

is defined as

$$R = g - L\{f_a\}, \tag{6.2}$$

where f_a is an approximation to f. It is important to observe that the residual error is dependent upon the operator L. More specifically, it is dependent upon the number of derivatives and the integrations that appear in L. Observations suggest that each derivative in L has the effect of decreasing the error bound by one power, whereas each integration has the effect of increasing the error bound by one power. For example, for an $O(h^{p+1})$ error rate in f, a derivative in L would make the residual R decrease at a rate of $O(h^p)$ whereas an integration would make it roll off faster, at an $O(h^{p+2})$ rate.

We observed this behavior for the MoM and the LCN solutions in Chapters 3 and 4, respectively. For the MoM solution using piecewise linear bases, the current density error should behave as $O(h^2)$ as the cell sizes are reduced, as was observed. The residual error for the TE EFIE operator, on the other hand, was observed to behave as $O(h)$. The TE EFIE operator

contains two tangential derivatives and one integral, resulting in an overall behavior that acts as a single derivative. A similar difference between the slope of the residual error plots and the current error plots was observed for the LCN solution of the TE EFIE in Chapter 4.

Generalizing the above observation to other integral equations, we conclude that for the TM polarization, the EFIE operator behaves as a single integral, which should yield a residual error that behaves as $O(h^{p+2})$ as the cell sizes are reduced. For the MFIE, the residual error has same rate as the interpolation error, viz. $O(h^{p+1})$. These observations are in line with previously published work [22-23].

6.4 Error behavior of the derivative of *J*

In chapter 4, the normalized change in the derivative of *J*, computed at cell junctions, was used as an estimate of the numerical error. If the error in the solution behaves as $O(h^q)$, then the error based on derivative discontinuity of *J* should behave as $O(h^{q-1})$. However, the observed error slope associated with the derivative discontinuity estimate was $O(h^q)$, the same as the interpolation error in *J*. This discrepancy is apparently due to the way we computed the derivative discontinuity error estimator. The estimator was computed from the expression

$$LE_i^{Diff} = \frac{|J_t'(t_{bi}^+) - J_t'(t_{bi}^-)|}{\max(|J_t|)}, \tag{6.3}$$

where the cell boundary is denoted by the location $\{t_{bi}\}$. Unlike the other error estimators used in Chapter 4, this one is not a unitless measure. The result in (6.3) has units of h^{-1}. By redefining the error estimator to include a scale factor of h^{-1}, the expected convergence rate $O(h^{q-1})$ can be obtained.

6.5 Calibration of error estimators using scale factors

From the preceding discussion, it has become clear that the residual error and the solution error slopes are, in general, different from each other. To make the residual error tightly track the solution error, some sort of *calibration* of the error estimator is required so that it does not under-estimate or over-estimate the actual error in the solution. Over-estimating the error is not as harmful as under-estimating it. Therefore, to account for all different scenarios of slope mismatches between the residual and the actual error, we need to develop a generalized calibration procedure. This issue has apparently never been addressed in the literature and still remains an open challenge. Our contribution here is to bring it forward to the research community. In the following, we will explore some of the mathematical foundations for the calibration procedure and attempt to implement appropriate scale factors.

Consider again the general equation

$$L\{f\} = g\,. \tag{6.4}$$

Suppose f_a is an approximation to the exact solution f, obtained by a numerical solution procedure. The residual R associated with this approximate solution is

$$R = g - L\{f_a\}\,. \tag{6.5}$$

As mentioned above, R does not track the actual error in the solution $f - f_a$. Equation (6.5) can be manipulated to obtain actual error from R as follows

$$f - f_a = L^{-1}\{R\}\,. \tag{6.6}$$

The difficulty is finding the inverse operator L^{-1}. If we can compute L^{-1}, we can construct an error estimate that actually tracks the solution error. The norm of the global error in the solution is related to the residual by

$$\|f - f_a\| \le \|L^{-1}\| \bullet \|R\| \tag{6.7}$$

The norm of the inverse operator, $\|L^{-1}\|$, could be used as a scale factor to adjust the rate of decrease in the residual such that it better tracks the actual error in the solution.

The major difficulty in the above formulation is finding the exact inverse operator. When we discretize the given integral equation, its continuous operator is projected onto a matrix operator, Z_1, the impedance matrix. To compute the residual, we are not able to use the same impedance matrix as it would give a zero residual and hence no information about the error. Instead, we form a new impedance matrix, Z_2, and use that to calculate the residual. The discretization of the continuous TE EFIE operator results in the following matrix equation

$$Z_1 \bullet J = E^{inc}, \tag{6.8}$$

whose solution yields the current density

$$J = Z_1^{-1} \bullet E^{inc}. \tag{6.9}$$

This computed J is used to calculate the residual error according to

$$R = E^{inc} - Z_2 \bullet J. \tag{6.10}$$

Applying the inverse of the new impedance matrix to the residual gives an error in J, ε_J. Unfortunately, this is not the difference between the approximate solution and the exact solution,

as desired, but the difference between two approximate solutions. With the idea that this might be a useful quantity towards finding the actual error from the residual, we compute

$$\varepsilon_J = Z_2^{-1} \bullet R \,. \tag{6.11}$$

Using a suitable matrix norm, Equation (6.11) can be written as

$$\left\|\varepsilon_J\right\| = \left\|Z_2^{-1}R\right\| \le \left\|Z_2^{-1}\right\|\left\|R\right\|, \tag{6.12}$$

where the quantity $\left\|\overline{Z}_2^{-1}\right\|$ is a scale factor that might enable us to adjust the slope of the residual to match the solution error slope.

There are many different ways to compute the norm of a matrix [24]. Commonly used definitions are the 1-*norm* and the ∞-*norm* which are simply the maximum absolute column sum and the maximum absolute row sum of the matrix, respectively. For a matrix, Z_2, of size $Nq \times Nq$, the 1-norm is given by

$$\left\|Z_2\right\|_1 = \frac{1}{Nq}\max\{\sum_{i=1}^{Nq}\left|z_2(i,j)\right|\}, \qquad \forall\ j \in \{1,2,3,...,Nq\}\,, \tag{6.13}$$

and the ∞-norm is given by

$$\left\|Z_2\right\|_\infty = \frac{1}{Nq}\max\{\sum_{j=1}^{Nq}\left|z_2(i,j)\right|\}, \qquad \forall\ i \in \{1,2,3,...,Nq\}\,. \tag{6.14}$$

These norms are expensive to compute as they require computing all of the matrix entries. Another commonly used norm that does not require a complete matrix is called *Frobenius* or *Euclidean* norm of a matrix. The Frobenius norm of a matrix Z_2 of size $Nq \times Nq$ is defined as

$$\|Z_2\|_F = \sqrt{\frac{1}{(Nq)^2}\sum_{i=1}^{Nq}|z_2(i,i)|^2}\ . \tag{6.15}$$

Since the Frobenius norm is only a function of the diagonal elements, it can be computed quite easily since it would require calculating only the *self-interaction* terms of the impedance matrix. It is important to note that the 1/*Nq* scaling factor in the above norm definitions is consistent with the way we have been defining the norm of a vector in this work. For a vector $A = \{a_i\}$ of size l_A, the 2-norm is defined as

$$\|A\| = \sqrt{\frac{1}{l_A}\sum_{i=1}^{l_A} a_i^2}\ . \tag{6.16}$$

We will use the above three different definitions of a norm of matrix and (6.12) to further investigate the relationship between global error rates of the residual and the solution in the next section.

6.6 Simulation results

In this section, we investigate the utility of the scheme proposed in the previous section by applying it to problems studied in previous chapters. First, consider a circular cylinder of 5λ circumference illuminated with a pair of line sources placed at a radial distance of 0.1λ away from the surface of the cylinder (Figure 3.1(a) from Chapter 3). A 50-cell discretization with q = 4 (4 quadrature points per cell) is used to calculate the initial solution for the current density. The normal E-field residual defined as

$$R = \frac{\left|\hat{n}\bullet\bar{E}^{tot} - \frac{j\eta}{k}\frac{d\bar{J}}{dt}\right|}{\max(\left|\bar{E}^{inc}\right|)}, \tag{6.17}$$

where $\bar{E}^{tot} = \bar{E}^{inc} + \bar{E}^{s}$, was calculated at *each* of the quadrature points using the equations in Appendix A. The new impedance matrix, Z_2, associated with this residual is a square matrix and it may be inverted and applied to the residual to compute an estimate of the error in *J*. This estimate of the error is shown in Figure 6.1, where it is compared with a reference error computed according to

$$\frac{\left|\bar{J} - \bar{J}_{ref}\right|}{\max(\left|\bar{J}_{ref}\right|)}, \tag{6.18}$$

where *J* is the original result and $\bar{J}_{ref}$ is computed by the LCN procedure with $q = 4$ and a 400-cell model. As shown in Figure 6.1, these error estimates do not agree very well, except in the immediate vicinity of 180 degrees where the current density is a maximum.

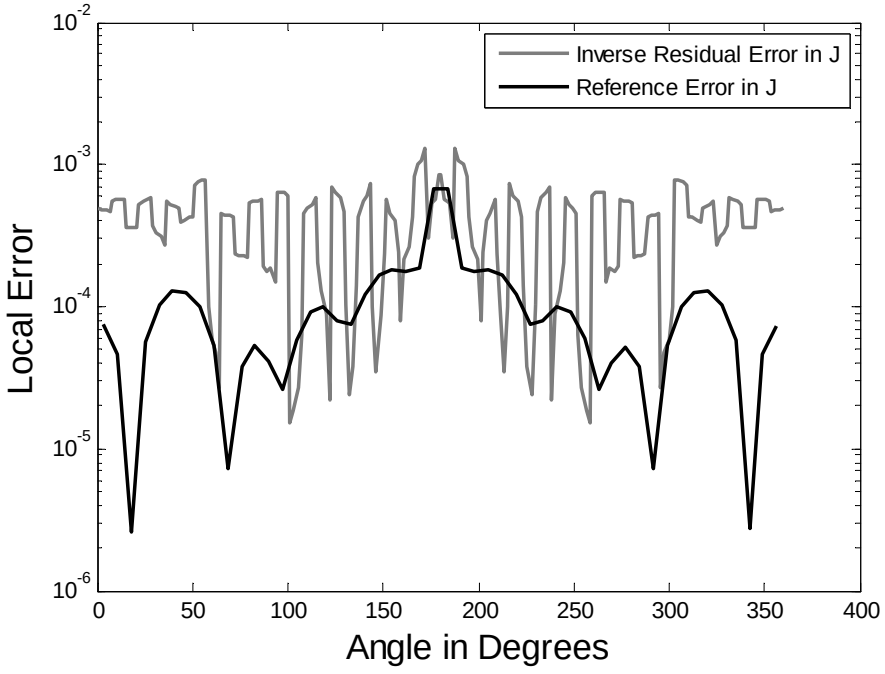

Fig. 6.1: Comparison of the inverse residual error and the reference error for a 5λ circumference circular cylinder illuminated with a pair of line sources.

To explore the possibility of converting the residual R into a more accurate estimate of the error in J, we multiply the normal E-field residual calculated using (6.17) with the inverse of the new impedance matrix, Z_2, to obtain ε_J according to (6.11). The 2-norm of ε_J is compared with the 2-norm of the reference error (Equation 6.18) for a varying mesh density. The result is shown in Figure 6.2. The 2-norm plot of the inverse residual error shown in Figure 6.2 is actually a plot of $\left\|Z_2^{-1}R\right\|$, which is rather expensive to compute. As an alternative, we can also compute $\left\|Z_2^{-1}\right\|\|R\|$ using any of the matrix norm definitions in (6.13)-(6.15) to scale the residual error using the norm of the inverse impedance matrix. Figures 6.3-6.5 show the results for this approach, respectively, for the Frobenius, 1-, and ∞- norms of Z_2^{-1}.

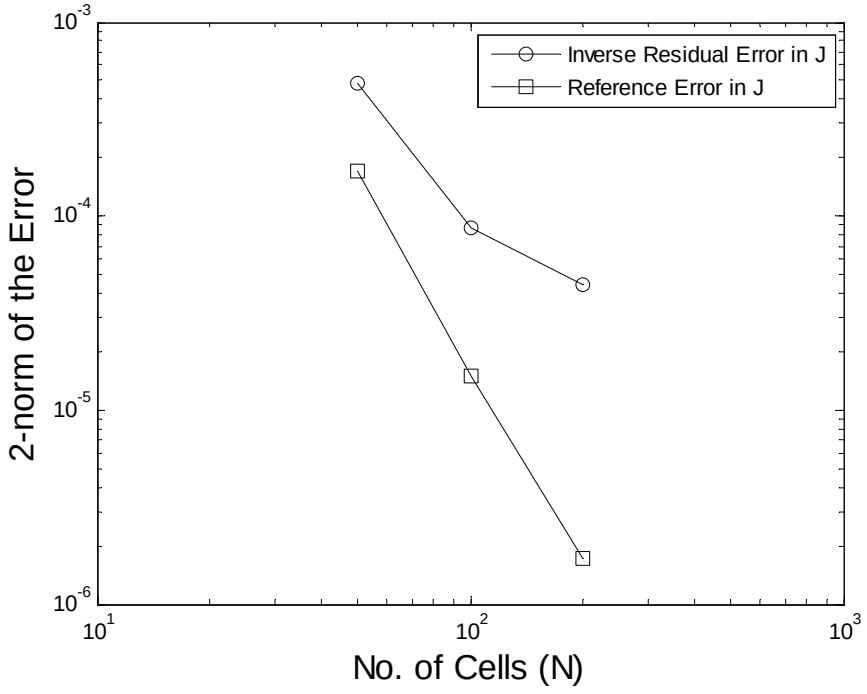

Fig. 6.2: A comparison of the 2-norm of the inverse residual, $\left\|Z_2^{-1}R\right\|$, and the 2-norm of the reference error.

The first observation about these results is that the plots obtained using different matrix norms are very similar, which suggests that the final result is independent of the norm definition used for Z_2^{-1}. The second observation is that the Schwarz inequality given by

$$\left\| Z_2^{-1} R \right\| \le \left\| Z_2^{-1} \right\| \left\| R \right\|, \tag{6.19}$$

is satisfied as is clear by comparison of Figure 6.2 and Figures 6.3-6.5 indicating the appropriateness of norm definitions. The third and more critical observation is that this approach fails to correct the slope mismatch error. The slope of the global error estimate remains different from that of the actual current density error, especially for higher mesh densities.

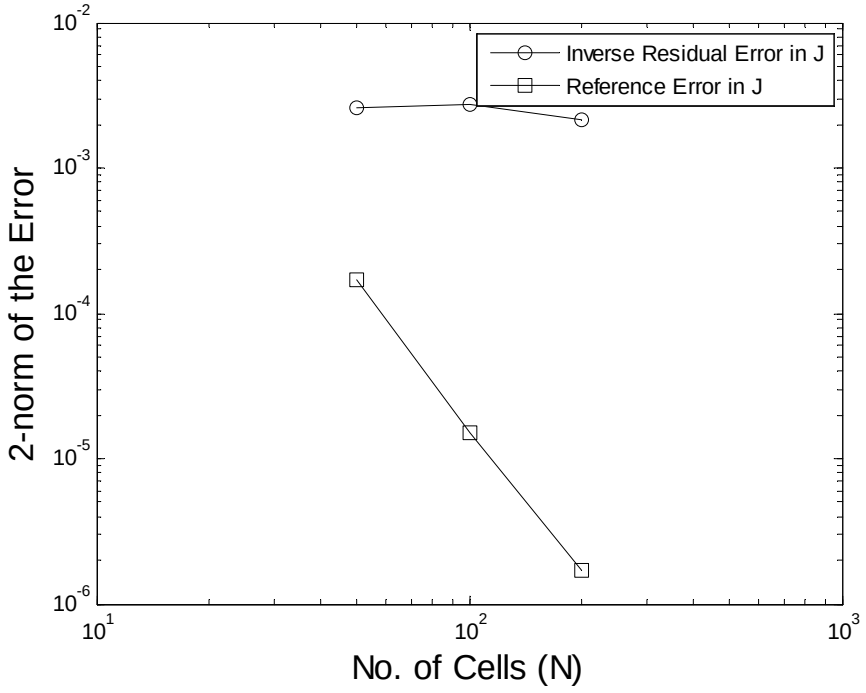

Fig. 6.3: A comparison of the 2-norm of normal E-field residual multiplied with Frobenius norm of Z_2^{-1} ($\left\| Z_2^{-1} \right\| \left\| R \right\|$) and the 2-norm of the reference error.

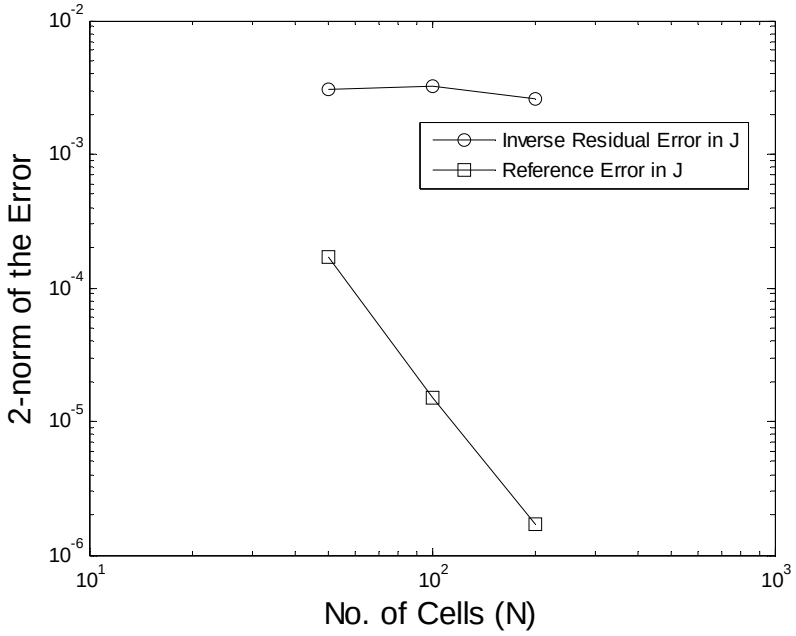

Fig. 6.4: A comparison of the 2-norm of normal E-field residual multiplied with 1-norm of Z_2^{-1} ($\left\|Z_2^{-1}\right\|\|R\|$) and the 2-norm of the reference error.

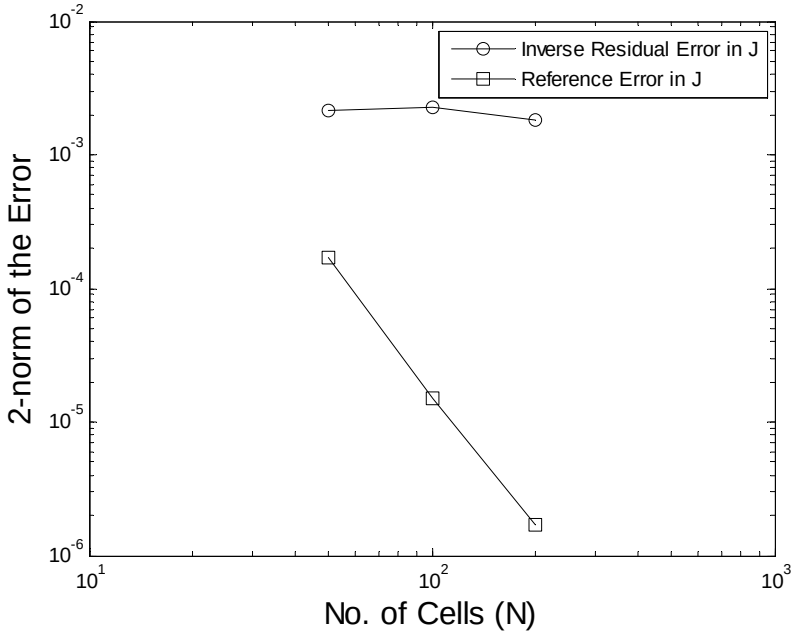

Fig. 6.5: A comparison of the 2-norm of normal E-field residual multiplied with ∞-norm of Z_2^{-1} ($\left\|Z_2^{-1}\right\|\|R\|$) and the 2-norm of the reference error.

We note that the matrix Z_2 is fundamentally no more accurate than the matrix Z_1 used to obtain the initial solution J, and the process of adjusting the error estimate proposed above is somewhat equivalent to computing two estimates (one using Z_1 to approximate L and the other using Z_2 to approximate L) and comparing them to obtain the error estimate. It is apparent that the same Z_2 that was used to construct R cannot be inverted and applied to the same R to correct for the slope problem in it. A more accurate reference solution is required. A Z_2 matrix obtained using a higher density model or a higher-order representation than that used for Z_1 should lead to a more accurate result for J, but the increased computational workload makes such an approach impractical. If a higher-order solution is computed, Equation (6.18) may be used directly to estimate the error in J.

As a different approach, we repeated the procedure using the tangential E-field residual estimator discussed in Chapter 4. In this implementation, instead of computing the residual at each of the quadrature points to form a square matrix Z_2, as we did above, we computed the residual at the center of each cell making the resulting matrix Z_2 rectangular with dimensions N by Nq. In this situation, the Moore-Penrose inverse, also called the pseudoinverse, was used to calculate the inverse of Z_2 to operate on the residual.

Figure 6.6 shows a comparison of the inverse residual error (Equation 6.12) obtained with a 50-cell model and $q = 4$ and the reference error (Equation 6.18) computed using a 400-cell model and $q = 4$. These plots show reasonable agreement in the vicinity of 180 degrees, where the current density has the largest magnitude, but deviate at other angles. Figure 6.7 shows the global error behavior for several different models, obtained by taking the 2-norm of (6.12) and (6.18). In this case, the slopes of the error curves are slightly different, but the overall error levels are similar.

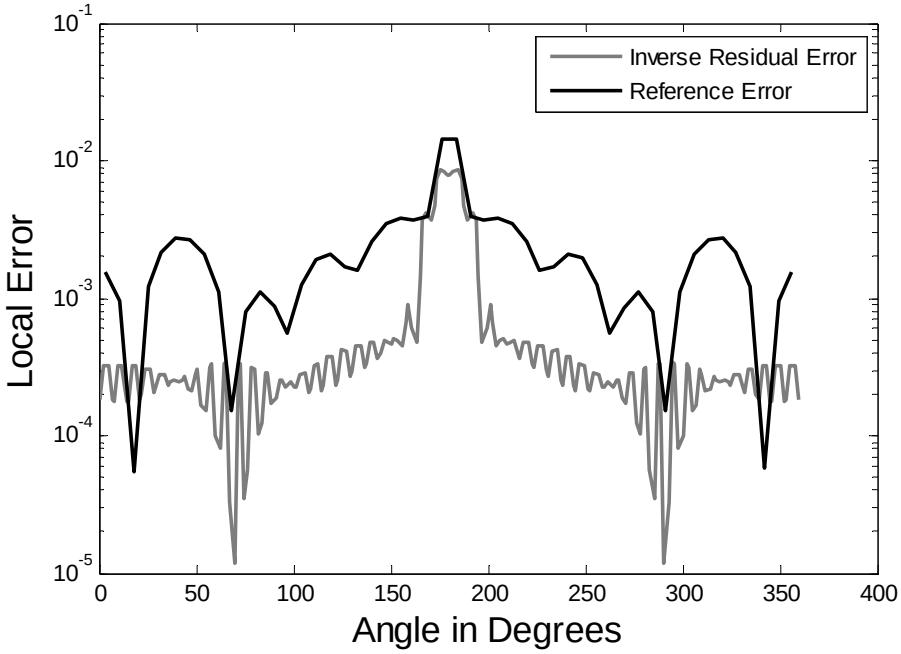

Fig. 6.6: Comparison of the inverse residual error and the reference error for a 5λ circumference circular cylinder illuminated with a pair of line sources.

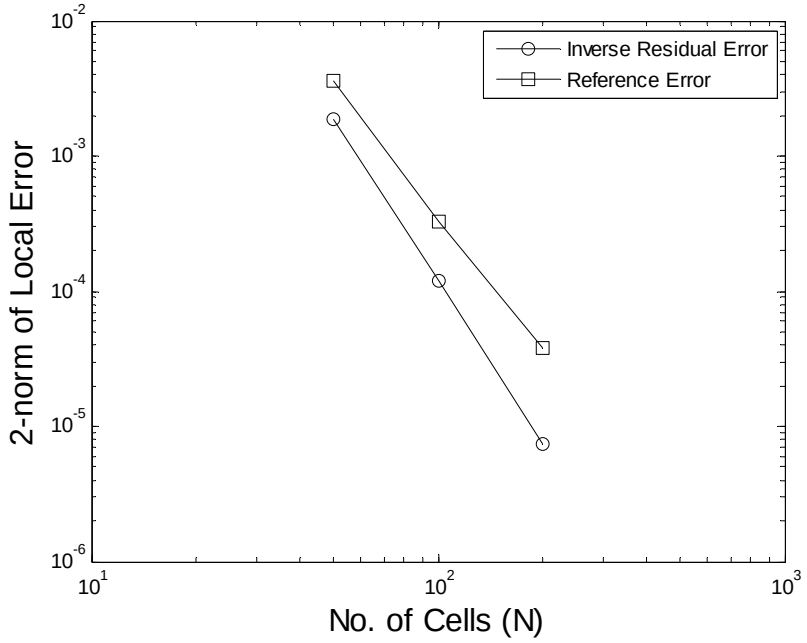

Fig. 6.7: Global error slopes of the inverse residual and the reference errors.

6.7 Concluding remarks

This chapter investigated the relationship between the numerical error in the solution and the residual. Solution error is dominated by the interpolation error, which is in turn related to the degree of the highest basis available in the set.

Convergence rates of the residuals for various electromagnetic integral equation operators were discussed and related to the solution error. As the models used for MoM or LCN analysis are refined, the residual errors and current errors usually decrease at different rates. Several approaches were considered to obtain scale factors that would correct for the slope mismatches. Although these implementations did not give completely satisfactory performance, they appear to improve the error estimates obtained by the residual calculations. Further research will be required to find a more effective way of scaling the residual error estimates.

CHAPTER 7

CONCLUDING REMARKS AND THE FUTURE WORK

This dissertation has focused on error estimation and adaptive refinement techniques for integral equation formulations of electromagnetic scattering. Various ways of estimating the error in the numerical solution of these integral equations using the MoM and the LCN methods have been studied. Sample problems involving smooth conducting targets illuminated by near-zone line sources were used to test the error estimators. These targets each exhibit a local region with relatively large error levels, and thus are suitable for assessing error estimator performance. The accuracy and computational cost of the estimators have been compared. Several simple adaptive refinement procedures have also been implemented for illustration.

The MoM implementation used in Chapter 3 was limited to flat-cell modeling and low-order (linear) bases, as is common practice in the computational electromagnetics discipline. That implementation is suitable for *h*-refinement, but not for *p*-refinement. Although the MoM approach can be implemented with curved cells and higher order bases, it is less computationally efficient than the LCN approach in that situation. Thus the LCN method was selected as the primary approach for studying the error estimators in subsequent chapters and for implementing simple *p*-refinement techniques.

The primary conclusion of this work is that the residual-based error estimators perform reasonably well for identifying the region of a problem with the largest error, but are less reliable for predicting the global error level associated with a particular computation. The most accurate estimator, and unfortunately the most costly estimator to implement, used an over-determined system. The current discontinuity error estimator (Chapter 4) usually worked as well as the

residual estimators for identifying regions with high error levels, and was far less costly to implement.

Since targets with corners introduce singularities into the currents, which tend to dominate the error predictions unless proper corner singularities are introduced into the representation of the currents, we only included one example target with exterior corners (Chapter 3). However, we observed that the implicit estimator discussed in Chapter 6 seems to be less likely to produce an error spike at corners of a conducting target, and thus may be preferred for use with structures with corners when the associated singular currents are not being rigorously modeled. Additional study of the implicit estimator for problems with corners is warranted.

Although the discussion and the examples were limited to two-dimensional problems involving smooth, conducting targets, the error estimators considered in this work should be easy to extend to three-dimensional problems, and to integral equation formulations for non-conducting structures. These topics are left to future work.

The adaptive refinement techniques used for illustration are very simple, and could be improved in sophistication. For instance, instead of automatically assigning a fixed percentage of the cells to one order, they could be modified to adapt the assignment algorithm to the dynamic range of the estimated error in a specific problem. This topic will also be left to future work.

APPENDIX A

COMPUTATION OF THE NORMAL COMPONENT OF THE SCATTERED E-FIELD

After the current density has been obtained by a numerical solution of the EFIE, the normal component of the scattered E-field can be obtained from the following equation:

$$E_n^s = -jk\eta \int_\alpha^\beta \hat{n}(t) \bullet \hat{t}(t') J_t(t') \frac{1}{4j} H_0^{(2)}(kR) dt' + \frac{\eta}{jk} \frac{\partial}{\partial n} \int_\alpha^\beta \frac{dJ_t}{dt'} \frac{1}{4j} H_0^{(2)}(kR) dt' . \tag{A1}$$

This equation can be rewritten in the form

$$E_n^s(t) = j \frac{\eta}{k} \int_\alpha^\beta J_t(t) D_n(t,t') dt' , \tag{A2}$$

where $D_n(t,t')$ is given by

$$D_n(t,t') = \{k^2 \cos[\Omega_n(t) - \Omega(t')] + \sin\Omega_n(t) \sin\Omega(t') \frac{\partial^2}{\partial x^2} - \sin[\Omega_n(t) + \Omega(t')] \frac{\partial^2}{\partial x \partial y} + \cos\Omega_n(t) \cos\Omega(t') \frac{\partial^2}{\partial y^2} \} \frac{1}{4j} H_0^{(2)}(kR) . \tag{A3}$$

In (A3), Ω is the angle between the outward normal vector and the scatterer surface, and Ω_n is defined as

$$\Omega_n(t) = \Omega(t) - \frac{\pi}{2} . \tag{A4}$$

The calculation of E_n^s is straightforward when the observer and source cells are different. For self-cell entries, additional care is required since $D_n(t,t')$ becomes infinite. In that case, the second integral can be written to take δ-functions at the cell ends explicitly into account:

$$\frac{\eta}{jk}\frac{\partial}{\partial n}\int_{\alpha}^{\beta}\frac{dJ_t}{dt'}\frac{1}{4j}H_0^{(2)}(kR)dt' = \frac{\eta}{jk}\frac{\partial}{\partial n}\int_{\alpha}^{\beta}\frac{dJ_t}{dt'}\frac{1}{4j}H_0^{(2)}(kR)dt' + \frac{\eta}{jk}\frac{\partial}{\partial n} \left\{\frac{1}{4j}H_0^{(2)}(kR)\Big|_{t,\alpha} J_t(\alpha) - \frac{1}{4j}H_0^{(2)}(kR)\Big|_{t,\beta} J_t(\beta)\right\}. \tag{A5}$$

To compute the first term on the right-hand side of (A5), we extract its principal value contribution at the center of the cell, yielding

$$\frac{\eta}{jk}\frac{\partial}{\partial n}\int_{\alpha}^{\beta}\frac{dJ_t}{dt'}\frac{1}{4j}H_0^{(2)}(kR)dt' = \frac{\eta}{jk}\left\{-\frac{1}{2}\frac{dJ_t}{dt'}\Big|_{obs.}\right\} + \frac{\eta}{jk}\int_{\alpha}^{\beta}\frac{dJ_t}{dt'}\frac{\partial}{\partial n}\left[\frac{1}{4j}H_0^{(2)}(kR)\right]dt'. \tag{A6}$$

The first term on the right-hand side of (A6) is the principal value contribution, which is similar to that obtained for the self-term calculations associated with the Magnetic Field Integral Equation [Chapter 2 of 4].

By combining (A6) with the previous expressions, we obtain the normal component of the electric field at the center of the source cell as:

$$\begin{aligned} E_n^s = &-jk\eta\int_{\alpha}^{\beta}\hat{n}(t)\bullet\hat{t}(t')J_t(t')\frac{1}{4j}H_0^{(2)}(kR)dt' \\ &+\frac{\eta}{jk}\left\{J_t(\alpha)\frac{\partial}{\partial n}\left[\frac{1}{4j}H_0^{(2)}(kR)\right]_{t,\alpha} - J_t(\beta)\frac{\partial}{\partial n}\left[\frac{1}{4j}H_0^{(2)}(kR)\right]_{t,\beta}\right\} \\ &-\frac{1}{2}\frac{\eta}{jk}\frac{dJ_t}{dt'}\Big|_{obs.} + \frac{\eta}{jk}\int_{\alpha}^{\beta}\frac{dJ_t}{dt'}\cdot\frac{\partial}{\partial n}\left[\frac{1}{4j}H_0^{(2)}(kR)\right]dt'. \end{aligned} \tag{A7}$$

This expression can be used to compute the normal component of the electric field E_n^s for use with the error estimators of Chapter 4.

References

[1] R. F. Harrington, *Field Computation by Moment Methods*. New York: IEEE Press, 1993. (Reprint of the original 1968 edition.)

[2] N. Morita, N. Kumagai, and J. R. Mautz, *Integral Equation Methods for Electromagnetics*. Boston: Artech House, 1990. (Translation of the original 1987 edition.)

[3] J. J. H. Wang, *Generalized Moment Methods in Electromagnetics – Formulation and Solution of Integral Equations*. New York: Wiley, 1991.

[4] A. F. Peterson, S. L. Ray, and R. Mittra, *Computational Methods for Electromagnetics*. New York: IEEE Press, 1998.

[5] A. F. Peterson and M. M. Bibby, *An Introduction to the Locally-corrected Nyström method*, San Rafael: Morgan & Claypool Synthesis Lectures, 2010.

[6] M. M. Botha, *Efficient finite element electromagnetic analysis of antennas and microwave devices: the FE-BI-FMM formulation and a posteriori error estimation for p adaptive analysis*. PhD Dissertation: University of Stellenbosch, South Africa, 2002.

[7] M. Ainsworth and J. T. Oden, *A posteriori Error Estimation in Finite Element Analysis*. New York: Wiley, 2000.

[8] F. J. C. Meyer and D. B. Davidson, "A posteriori error estimates for two-dimensional electromagnetic field computations: Boundary elements and finite elements," *ACES Journal*, vol. 11, pp. 40-54, July 1996.

[9] K. C. Chellamuthu, N. Ida, and Q. K. Zhang, "Adaptive finite element mesh refinement and '*a posteriori*' error estimation procedures for electromagnetic field computation," *ACES Journal*, vol. 12, pp. 61-68, March 1997.

[10] M. M. Botha and D. B. Davidson, "An explicit a posteriori error indicator for electromagnetic, finite element-boundary integral analysis," *IEEE Trans. Antennas Propagat*., vol. 53, pp. 3717-3725, November 2005.

[11] M. M. Botha and D. B. Davidson, "The implicit element residual method for a posteriori error estimation in FE-BI analysis," *IEEE Trans. Antennas Propagat*., vol. 54, pp. 255-258, January 2006.

[12] M. M. Botha and D. B. Davidson, "Investigation of an explicit, residual-based, a posteriori error indicator for the adaptive finite element analysis of waveguide structures," *ACES Journal*, vol. 21, no.1, pp. 63-71, March 2006.

[13] E. Kita and N. Kamiya, "Error estimation and adaptive mesh refinement in boundary element method, an overview," *Engineering Analysis with Boundary Elements*, vol 25, pp. 479-495, 2001.

[14] K. F. Warnick and W. C. Chew, "Error analysis of the moment method," *IEEE Antennas Propagat. Mag.*, vol. 46, pp. 38-53, December 2004.

[15] K. F. Warnick, *Numerical Analysis for Electromagnetic Integral Equations.* Boston: Artech House, 2008.

[16] G. C. Hsiao and R. E. Kleinman, "Error control in numerical solution of boundary integral equations," *ACES Journal*, vol. 11, pp. 32-36, 1996.

[17] G. C. Hsiao and R. E. Kleinman, "Mathematical foundations for error estimation in numerical solutions of integral equations in electromagnetics," *IEEE Trans. Antennas Propagat*., vol. 45, pp. 316-328, March 1997.

[18] A. P. C. Fourie, D. C. Nitch, and A. R. Clark, "Predicting MoM error currents by inverse application of residual E-fields," *ACES Journal*, vol. 14, pp. 72-75, November 1999.

[19] P. J. Davies, D. B. Duncan, and S. A. Funken, "Accurate and efficient algorithms for frequency domain scattering from a thin wire," *J. Computational Physics*, vol. 168, pp. 155-183, 2001.

[20] F. G. Bogdanov and R. G. Jobava, "Estimating accuracy of MoM solutions on arbitrarily triangulated 3-D geometries based on examination of boundary conditions performance and accurate derivation of scattered fields," *JEWA*, vol. 18, no. 7, pp. 879-897, 2004.

[21] A. F. Peterson and M. M. Bibby, "High-order numerical solutions of the MFIE for the linear dipole," *IEEE Trans. Antennas Propagat*., vol. 52, pp. 2684-2691, October 2004.

[22] M. M. Bibby and A. F. Peterson, "On the use of over-determined systems in the adaptive numerical solution of integral equations," *IEEE Trans. Antennas Propagat.,* vol. 53, pp. 2267-2273, July 2005.

[23] M. M. Bibby, A. F. Peterson, and C. M. Coldwell, "High order representations for singular currents at corners," *IEEE Trans. Antennas Propagat*., vol. 56, pp. 2277-2287, August 2008.

[24] G. H. Golub and C. F. Van Loan, *Matrix Computations*. Baltimore: Johns Hopkins University Press, 1989.

[25] X. Wang, M. M. Botha, and J.-M. Jin, "An error estimator for the moment method

in electromagnetic scattering," *Microwave and Optical Technology Letters*, vol. 44, pp. 320-326, February 2005.

[26] K. R. Davey and D. Zheng, "Error tracking in boundary element formulations," *IEEE Trans. Magnetics*,. Vol. 32, pp. 259-264, January 1996.

[27] J. Wang and J. P. Webb, "Hierarchal vector boundary elements and adaption for 3-D electromagnetic scattering," *IEEE Trans. Antennas Propagat*., vol. 45, pp. 1869-1879, December 1997.

[28] K. J. Bunch and R. W. Grow, "The boundary residual method for three-dimensional homogeneous field problems with boundaries of arbitrary geometries," *International Journal of Infrared and Millimeter Waves*, vol. 10, pp. 1007-1032, 1989.

[29] U. Saeed and A. F. Peterson, "A comparison of several local error estimators for integral equation formulations," presented in *URSI*, Ottawa, Canada, 2007.

[30] S. D. Gedney, "On deriving a locally-corrected Nyström scheme from a quadrature sampled moment method," *IEEE Trans. Antennas Propagat.*, vol. 51, pp. 2402–2412, September 2003.

[31] R. F. Harrington, *Time Harmonic Electromagnetic Fields*. New York: IEEE Press, 2001.

[32] U. Saeed and A. F. Peterson, "Adaptive refinement for the locally-corrected Nyström method based on an implicit error estimation scheme," *Proc. ACES 2011 Conference*, Williamsburg, VA, 2011.

[33] A. F. Peterson, "Accuracy of currents produced by the locally-corrected Nyström method and the method of moments when used with higher-order representations," *Applied Computational Electromagnetics Society (ACES) Journal*, vol. 17, pp. 74-83, March 2002.